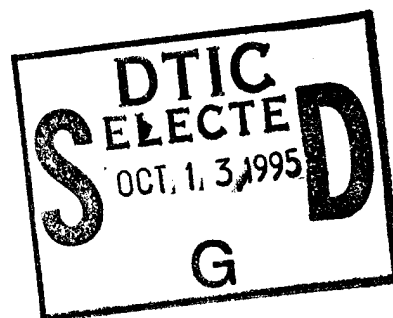RL-TR-95-149
Final Technical Report
August 1995

DIELECTRIC DISK RADIATING ELEMENTS

University of Mississippi

G.P. Junker, A.A. Kishk, A.W. Glisson, and D. Kajfez

DTIC
SELECTED
OCT. 1, 3, 1995
G

APPROVED FOR PUBLIC RELEASE; DISTRIBUTION UNLIMITED.

19951011 112

Rome Laboratory
Air Force Materiel Command
Griffiss Air Force Base, New York

DTIC QUALITY INSPECTED 5

This report has been reviewed by the Rome Laboratory Public Affairs Office (PA) and is releasable to the National Technical Information Service (NTIS). At NTIS it will be releasable to the general public, including foreign nations.

RL-TR-95-149 has been reviewed and is approved for publication.

APPROVED: *Bris Tomasic*

BORIS TOMASIC
Project Engineer

FOR THE COMMANDER: *Robert V. McGahan*

ROBERT V. McGAHAN
Acting Director
Electromagnetics & Reliability Directorate

REPORT DOCUMENTATION PAGE

Form Approved
OMB No. 0704-0188

1. AGENCY USE ONLY (Leave Blank)	2. REPORT DATE August 1995	3. REPORT TYPE AND DATES COVERED Final Apr 91 - Sep 94

4. TITLE AND SUBTITLE

DIELECTRIC DISK RADIATING ELEMENTS

5. FUNDING NUMBERS
C - F19628-91-K-0010
PE - 61102F
PR - 2305
TA - J3
WU - 49

6. AUTHOR(S)

G.P. Junker, A.A. Kishk, A.W. Glisson, and D. Kajfez

7. PERFORMING ORGANIZATION NAME(S) AND ADDRESS(ES)

University of Mississippi
Department of Electrical Engineering
University MS 38677

8. PERFORMING ORGANIZATION REPORT NUMBER

N/A

9. SPONSORING/MONITORING AGENCY NAME(S) AND ADDRESS(ES)

Rome Laboratory (ERAA)
31 Grenier St
Hanscom AFB MA 01731-3010

10. SPONSORING/MONITORING AGENCY REPORT NUMBER

RL-TR-95-149

11. SUPPLEMENTARY NOTES

Rome Laboratory Project Engineer: Boris Tomasic/ERAA/(617) 478-2055

12a. DISTRIBUTION/AVAILABILITY STATEMENT

Approved for public release; distribution unlimited.

12b. DISTRIBUTION CODE

13. ABSTRACT (Maximum 200 words)

A new class of antennas, consisting of dielectric resonant cylinders located on a conducting plane, is investigated numerically and experimentally. The numerical formulation is applied to the problem of a dielectric body of revolution in the presence of an electrically thin wire, or in the presence of a slot aperture. The formulation enables one to compute the input impedance of practical dielectric-cylinder antennas, which are fed either by a probe at the end of a coaxial cable, or by a slot in the ground plane of a microstrip transmission line. Such computations were heretofore unavailable in the published literature. Experiments were performed to verify the impedance behavior as a function of frequency. The agreement with the numerical results is excellent for the wire-fed antennas but, for the slot-fed antennas, the measured values are strongly influenced by the details of the feeding arrangement. The slot-fed dielectric antennas will require further investigation before the influence of the aperture details is fully understood, and a satisfactory agreement between the theory and experiment is obtained.

14. SUBJECT TERMS

Dielectric disk, Radiating array elements, Microwaves, Dielectric resonator

15. NUMBER OF PAGES
118

16. PRICE CODE

17. SECURITY CLASSIFICATION OF REPORT	18. SECURITY CLASSIFICATION OF THIS PAGE	19. SECURITY CLASSIFICATION OF ABSTRACT	20. LIMITATION OF ABSTRACT
UNCLASSIFIED	UNCLASSIFIED	UNCLASSIFIED	UL

ACKNOWLEDGEMENT

Accesion For		
NTIS CRA&I		☒
DTIC TAB		☐
Unannounced		☐
Justification		
By		
Distribution /		
Availability Codes		
Dist	Avail and / or Special	
A-1		

TABLE OF CONTENTS

CHAPTER 1

Introduction

Classical antenna structures are designed using electrically conducting elements such as wires, reflectors, microstrip patches, etc., as the basic radiators. The dielectric parts of traditional antennas serve mainly as supporting and insulating elements in the antenna system. There have been occasional uses of dielectrics for radiating structures, such as in polyrod antennas, lens antennas, or in applications such as covering the metal walls for achieving the proper polarization properties, e.g., in low-sidelobe horn antennas. However, the majority of antennas in present use are predominantly made of metal parts.

The research project described in this report investigates a new class of antennas, which will have a minimum of metal parts, and consist mainly of ceramic dielectric materials mounted over a metal ground plane. Possible advantages of these radiating elements are wider bandwidth and higher power handling capabilities, as compared with microstrip antennas of similar size. Furthermore, dielectric radiators offer the freedom to choose a resonant mode that produces broadside radiation (e.g., HEM_{11}), or another mode which produces endfire radiation (e.g., TE_{01}).

About ten years ago, experimental studies were conducted to determine the radiation characteristics of cylindrical [1] and hemispherical [2] dielectric resonator antennas (DRAs) residing on a conducting ground plane. Simultaneously, numerical and experimental studies of dielectric resonators sitiuated in free space have established the resonant frequencies of the several lowest source-free modes, their near field distributions and their radiation Q factors [40, 43].

In [1, 2] the DRAs were excited by a coaxial probe extending into the dielectric material through the bottom of the ground plane. One of the conclusions drawn from the experimental studies was that in order to obtain desirable broadside radiation characteristics, the feed probe must be positioned away from the resonator's axis of symmetry and near the "outer wall" of the dielectric resonator.

Later, new applications for dielectric resonator antennas (DRA) were developed after having demonstrated that the radiation characteristics of the antennas measured in [1] could be numerically computed by modeling the dielectric resonator (DR) as a body of revolution (BOR),

1

and simulating the off axis coaxial probe feed as an infinitesimal dipole radiator [3], [4]. It should be clearly understood that the coaxial feed probe was only simulated in this work. The physical presence of the feed probe was not accounted for since no boundary condition was enforced on the feed probe itself; and as such, the antenna input impedance could not be obtained. When the feed probe's axis of symmetry is coincident with the axis of symmetry of the BOR [5], a pure BOR model can be used to compute the input impedance of a DRA since it allows for enforcement of the electromagnetic boundary conditions on the feed probe. Without knowledge of an antenna's input impedance, it is not possible for an engineer to efficiently design any system whose constituent components include dielectric resonator antennas.

Until now, the only precision models the engineer had at his disposal were techniques such as those described in [42, 43], which are summarized in a recent monograph [6], from which the modal electromagnetic field distribution of a dielectric resonator in infinite homogeneous free space undisturbed by any feeding structure may be determined, or techniques such as [3, 4], where the feed probe is merely simulated. From studies of the field distribution, the engineer may then determine a possible location for the feed structure. However, there is still no information concerning the interaction of the feed structure with the dielectric resonator.

Previous investigations of method-of-moments (MoM) analysis of structures consisting of combined BORs and wires have been restricted to perfect electric conductors (PEC) only. In [7], a technique used for the computation of input impedance of monopole antennas in the presence of conducting BORs was introduced. Far field patterns were computed for rotationally symmetric conducting bodies with attached wires considered as both radiating [8] and as scattering [9] problems. The problem of computation of the input impedance of wire antennas attached on-axis to a BOR was solved in [10]. Radiation patterns from reflector antennas with struts [11] were computed from currents obtained after applying the techniques introduced in [8] and [9]. The reflector surfaces were modelled as BORs and the struts as wire structures. The BOR/wire concepts have been applied to arbitrary surfaces in combination with conducting and dielectric BORs [12-14].

This report builds upon this foundation by extending the existing BOR/wire technique to include dielectric bodies coupled to electrically thin wires [15, 17] and slot apertures [16]. Chapter 2 formulates a system of integro-differential equation for solving the electromagnetic boundary value problem generated by thin wires coupled to a dielectric BOR. This formulation is general in that the wires may be interior or exterior to the BOR. A Galerkin moment method

2

procedure is applied to solve this system of equations. Chapter 3 presents results of experimental and theoretical studies of cylindrical dielectric resonator antennas excited by a coaxial probe. Chapter 4 extends the theoretical development presented in Chapter 2 by formulating and solving the boundary value problem of a thin slot aperture coupled to a dielectric BOR. Also, the chapter contains results of the experimental investigation of the input impedance of various slot-excited dielectric radiators. Appendix A introduces an extended delta gap source model, which is used as a forcing function for the electric field integral equation of thin wire theory. This extended delta source model eliminates some of the problems associated with the existing delta gap source model. Additional details of the numerical formulation used in this work are provided in Appendices B, C, and D.

In the course of this investigation, the faculty and students at University of Mississipi have authored and co-authored the following papers that are directly related to this project:

1. G. P. Junker, A. A. Kishk, and A. W. Glisson, "MoM solution of wire radiators coupled to dielectric bodies of revolution," *1993 IEEE Antennas and Propagation Society International Symposium Digest*, pp. 40-43, Ann Arbor, MI, July 1993.

2. A. A. Kishk, A. W. Glisson, and D. Kajfez, "Computed resonant frequency and far fields of isolated dielectric disks," *1993 International IEEE Antennas and Propagation Society International Symposium Digest*, pp. 408-411, Ann Arbor, MI, July 1993.

3. A. A. Kishk, M. R. Zunoubi, and D. Kajfez, "A numerical study of dielectric disk antenna above grounded dielectric substrate," *IEEE Transactions on Antennas and Propagation*, vol. 41, pp. 813-821, June 1993.

4. A. A. Kishk, A. Ittipiboon, Y. M. M. Antar, and M. Cuhaci, "Dielectric resonator antennas fed by a slot in the ground plane of a microstrip line," *Proceedings of the Eighth International Conference on Antennas and Propagation*, Part 1, pp. 540-543, Heriot-Watt University, UK, April 1993.

5. A. A. Kishk, A. Ittipiboon, Y. M. M. Antar, and M. Cuhaci, "Slot Excitation of the Dielectric Disk radiator," submitted to the *IEEE Trans. on Antennas and Propagation*, under review.

6. G. P. Junker, A. A. Kishk, A. W. Glisson, and D. Kajfez, "Effect of an air gap on a cylindrical dielectric resonator antenna operating in the TM_{01} mode," *Electronics Letters*, vol. 30, No. 2, pp. 97-98, 1994.

7. G. P. Junker, A. A. Kishk, A. W. Glisson, and D. Kajfez, "Effect of an air gap around the coaxial probe exciting a cylindrical dielectric resonator antenna," *Electronics Letters*, vol. 30, No. 3, pp. 177-178, 1994.

8.   G. P. Junker, A. A. Kishk, and A. W. Glisson, "Input impedance of an aperture coupled dielectric resonator antenna," *1994 IEEE Antennas and Propag. Society International Symposium Digest*, vol. 2, pp. 748-751, Seattle, June 1994.

9.   J. Chen, A. A. Kishk, and A. W. Glisson, "Electromagnetic scattering from a conducting object of arbitrary shape embedded in a mutlilayer medium," *1994 IEEE Antennas and Propag. Society International Symposium Digest*, vol. 2, pp. 1346-1349, Seattle, June 1994.

10.   G. P. Junker, A. A. Kishk, A. W. Glisson, "Input impedance of dielectric resonator antennas excited by a coaxial probe," *IEEE Trans. Antennas Propag.*, vol. 42, pp. 960-966, July 1994.

11.   G. P. Junker, A. A. Kishk, A. W. Glisson, D. Kajfez, "Effect of fabrication imperfections for ground-plane-backed dielectric resonator antennas with excitation," *ANTEM Proceedings*, pp. 445-447, Ottawa, Canada, August 1994.

12.   G. P. Junker, A. A. Kishk, A. W. Glisson, D. Kajfez, "Effect of fabrication imperfections for ground-plane-backed dielectric resonators with coaxial excitation," submitted to *IEEE Antennas Propag. Magazine*.

13.   G. P. Junker, A. A. Kishk, A. W. Glisson, "Input impedance of aperture coupled dielectric resonator antennas," submitted to *IEEE Trans. Antennas Propag.*

Each paper contains an acknowledgement of the AFOSR support. The photocopies of the above papers that have appeared in print are enclosed with this report.

CHAPTER 2

Thin Wires Coupled to Dielectric Bodies of Revolution

2.1 Formulation of the Boundary Value Problem

In this section, wires, or conducting strips, which may be modelled as wires, are considered. In the case of the wire, thin shall mean that the wire radius, as a function of operating frequency, is small enough in terms of wavelengths in the medium in which it resides so that the only component of current induced on the wire is that which is axially directed and circumferentially invariant. This definition is the same as that given by the well developed thin wire theory [18]. For a finite length strip to be considered thin, it's equivalent electrical radius [19] must be such that the definition of thin as imposed by thin wire theory is valid. The geometry of Fig. 2a is typical of the electromagnetic boundary value problem of a structure consisting of thin wires and a dielectric body of revolution (DBOR). The DBOR is represented as the cross section of a surface of revolution, S_{de}. The surface S_{de} has been created by the rotation of a simple curve or a generating arc about the Z-axis in a cylindrical coordinate system (the generating arc may be thought of as the intersection of a surface of revolution and a plane defined by a constant angle ϕ in a cylindrical coordinate system). In general, the wire or thin conductor may be any structure which satisfies the given definition of "thin" and whose geometry can be represented as a simple curve. The DBOR is composed of a homogeneous material with constituent parameters ϵ_d and μ_d, where ϵ_d and μ_d are the permittivity and permeability of the material, respectively. The region exterior to the DBOR is composed of a homogeneous medium of constituent parameters ϵ_e and μ_e. The wires are represented by S_{wd} and S_{we} where the subscripts "wd" and "we" refer to wire elements interior and exterior to the DBOR, respectively. The electric and magnetic field vectors are represented by the symbols $\underline{E}$ and $\underline{H}$, respectively. Superscripts "dt" and "et" refer to the total field interior and exterior to the DBOR, respectively.
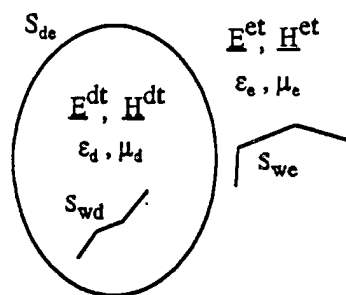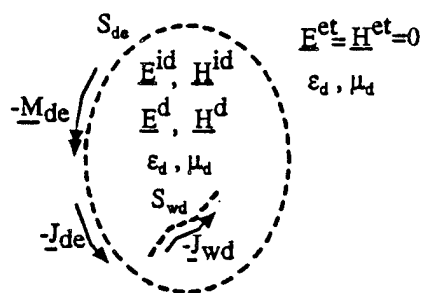
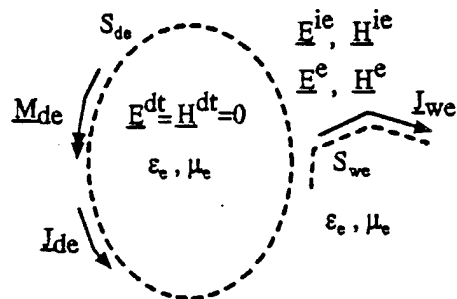Fig. 2.1a The original problem.

Fig. 2.1b The interior problem.

Fig. 2.1c. The exterior problem.

6

The field vectors $\underline{E}$ and $\underline{H}$ with superscripts "d" and "e" refer to the fields which arise from the equivalent currents which reside on the surfaces in the interior and exterior problems, respectively. The superscript "i" refers to the known field, that is, the source field which excites the wire radiator. The equivalent electric and magnetic surface currents which arise from application of the field equivalence principle are represented by the symbols $\underline{J}$ and $\underline{M}$, respectively.

In accordance with the field equivalence principle [20], the original problem of Fig. 2a can be divided into two problems: one for the interior region, and the other for the exterior region. The two equivalent problems are illustrated in Figs. 2b and 2c. By enforcing the boundary conditions that the tangential component of the electric field must vanish at the conductor surface, and that the tangential components of both the electric and magnetic fields must be continuous across the dielectric surface, a system of integro-differential equations is obtained from which the unknowns $\underline{J}_{wd}$, $\underline{J}_{we}$, $\underline{M}_{de}$, and $\underline{J}_{de}$ can be determined. This system of equations can be written in operator form as the following:

$$\underline{E}^d_{tan}(\underline{J}_{de}+\underline{J}_{wd},\underline{M}_{de}) = \underline{E}^{id}_{tan} \quad \text{on } S_{wd} \tag{2.1}$$

$$\underline{E}^e_{tan}(\underline{J}_{de}+\underline{J}_{we},\underline{M}_{de}) = -\underline{E}^{ie}_{tan} \quad \text{on } S_{we} \tag{2.2}$$

$$\underline{E}^e_{tan}(\underline{J}_{de}+\underline{J}_{we},\underline{M}_{de}) + \underline{E}^d_{tan}(\underline{J}_{de}+\underline{J}_{wd},\underline{M}_{de}) = \underline{E}^{id}_{tan} - \underline{E}^{ie}_{tan} \quad \text{on } S_{de} \tag{2.3}$$

$$\underline{H}^e_{tan}(\underline{J}_{de}+\underline{J}_{we},\underline{M}_{de}) + \underline{H}^d_{tan}(\underline{J}_{de}+\underline{J}_{wd},\underline{M}_{de}) = \underline{H}^{id}_{tan} - \underline{H}^{ie}_{tan} \quad \text{on } S_{de} \tag{2.4}$$

The above system of equations consists of the electric field integral equation (EFIE) on the conductor surface, and both the EFIE and the magnetic field integral equation (MFIE) on the DBOR surface. This formulation is refered to as the E-PMCHW formulation [21]. For future reference, the left hand side of the above system of equations shall be denoted as $\underline{L}(f)$ where $\underline{L}$

represents $\underline{E}$ and $\underline{H}$ and $\underline{f}$ represents the unknown currents $\underline{J}$ and $\underline{M}$. The right hand side of the same system of equations shall be denoted as g.

2.2 The Potential Integrals

The integro-differential operators $\underline{E}(\underline{J},\underline{M})$ and $\underline{H}(\underline{J},\underline{M})$ of Eqs. (2.1) to (2.4) are defined in terms of magnetic and electric vector and scalar potential functions represented by $\underline{A}$, $\underline{F}$, Φ, and Ψ, respectively,

$$\underline{E}^q(\underline{J},\underline{M}) = -j\omega\underline{A}^q - \nabla\Phi^q - \frac{1}{\epsilon_q}\nabla\times\underline{F}^q \qquad (2.5)$$

$$\underline{H}^q(\underline{J},\underline{M}) = -j\omega\underline{F}^q - \nabla\Psi^q + \frac{1}{\mu_q}\nabla\times\underline{A}^q \qquad (2.6)$$

where the potential functions are defined as

$$\underline{A}^q(\underline{r}) = \mu_q \int_S \int G^q(\underline{r},\underline{r}')\underline{J}(\underline{r}')ds' \qquad (2.7)$$

$$\underline{F}^q(\underline{r}) = \epsilon_q \int_S \int G^q(\underline{r},\underline{r}')\underline{M}(\underline{r}')ds' \qquad (2.8)$$

$$\Phi^q(\underline{r}) = \frac{1}{\epsilon_q} \int_S \int G^q(\underline{r},\underline{r}')\rho_e(\underline{r}')ds' \qquad (2.9)$$

$$\Psi^q(\underline{r}) = \frac{1}{\mu_q} \int_S \int G^q(\underline{r},\underline{r}')\rho_m(\underline{r}')ds' \qquad (2.10)$$

and S is a surface that includes the dielectric resonator surface and the wire radiator surfaces that contribute to the field in region q. The surface charge sources ρ_e and ρ_m are related to the current sources through the equations of continuity

$$\nabla'\bullet\underline{J}(\underline{r}') = -j\omega\rho_e(\underline{r}') \qquad (2.11)$$

8

$$\nabla' \bullet \underline{M}(\underline{f}) = -j\omega\rho_m(\underline{f}) \tag{2.12}$$

The function G^q is the scalar free space Green's function and is a function of $\underline{r}$ and $\underline{f}$, the field and source coordinates, respectively.

2.3 Moment Method Solution

The surface integral equations (2.1)-(2.4) are solved by the MoM [18]. The described problem can be solved in an efficient manner by a judicious choice of basis and testing functions. First, consider the DBOR. Due to the axial symmetry, two components of electric and magnetic current can be identified: one directed along the generating arc, and the other in the circumferential direction. The surface $S_{d\bullet}$ is divided into annular rings and upon these rings the surface currents are expanded as a series of overlapping functions of the following form:

$$\underline{K} = \sum_{m=-N_\bullet}^{N_\bullet} \sum_{N=1}^{N_t} (K_{mN}^t \underline{K}_{mN}^t + K_{mN}^\phi \underline{K}_{mN}^\phi) \quad \text{on} \quad S_{d\bullet} \tag{2.13}$$

where K_{mN}^t and K_{mN}^ϕ are the current expansion coefficients and the basis functions are defined by

$$\underline{K}_{mN}^p = u_p \frac{T_N(t)}{\rho(t)} e^{jm\phi} \tag{2.14}$$

with $\underline{K} = \underline{J}_{d\bullet}$ or $\underline{M}_{d\bullet}$, $p = t$ or ϕ, and where u is a unit vector. The radial distance from the axis of the resonator to the surface $S_{d\bullet}$ is $\rho(t)$. In part, $\underline{K}$ is composed of the product of two functions, $T_N(t)e^{jm\phi}$, with different spatial variation. $T_N(t)$ is a piecewise linear function (commonly called the triangle function) that models the variation along the generating arc, and $e^{jm\phi}$, an entire domain harmonic function used to model the circumferential variation, is the mth Fourier modal expansion term. The triangle function is defined in Appendix B. According to thin wire theory,

9

the only component of current on a wire is that which is axially directed and circumferentially invariant. Hence the current on the wire is expanded in a series of functions as

$$I = \sum_p d_p T_p(w) u_p \quad p=1,2, ..., p_w \quad \text{on} \quad S_{wq} \tag{2.15}$$

where d_p is the current expansion coefficient associated with each triangle basis function $T_p(w)$, and p_w is the total number of basis functions on the wire. It is now convenient to refer to the individual terms of the series of basis functions representing the unknowns $\underline{J}$ and $\underline{M}$ as $\underline{f}_n$ and the unknown current coefficients as c_n. The unknown current coefficients c_n can be determined via the method of moments by forming the inner product via the Galerkin technique after defining a set of testing functions $\underline{w}_n = \underline{f}_n^*$, where * is the complex conjugate. This results in the following system of equations

$$\sum_{n=1}^{N} c_n < \underline{w}_m, \underline{L}(\underline{f}_n) > = < \underline{w}_m, g > \quad m=1,2,..,N . \tag{2.16}$$

An advantage of the Galerkin procedure is the resulting symmetry in the inner products when the coordinates of the testing and basis functions are interchanged. The above system of equations may be expressed in matrix form as

10

$$
\begin{bmatrix}
[BB]_{-n} & \cdot & \cdots & \cdot & \cdots & \cdot & \cdot & [BW]_{-n} \\
\cdot & [BB]_{-n+1} & \cdots & \cdot & \cdots & \cdot & 0 & [BW]_{-n+1} \\
\cdot & \cdot & \cdots & \cdots & \cdots & \cdots & \cdots & \cdots \\
\cdot & \cdot & \cdots & [BB]_0 & \cdots & \cdot & \cdot & [BW]_0 \\
\cdot & 0 & \cdots & \cdot & \cdots & \cdots & \cdot & \cdots \\
\cdot & \cdot & \cdots & \cdot & \cdots & [BB]_{n-1} & \cdot & [BW]_{n-1} \\
\cdot & \cdot & \cdots & \cdots & \cdot & \cdot & [BB]_n & [BW]_n \\
[WB]_{-n} & [WB]_{-n+1} & \cdots & [WB]_0 & \cdots & [WB]_{n-1} & [WB]_n & [WW]
\end{bmatrix} \cdot
$$

$$
\begin{bmatrix}
|JM>_{-n} \\
|JM>_{-n+1} \\
\cdots \\
|JM>_0 \\
\cdots \\
|JM>_{n-1} \\
|JM>_n \\
|J_w>
\end{bmatrix}
=
\begin{bmatrix}
0 \\
0 \\
\cdots \\
0 \\
\cdots \\
0 \\
0 \\
|V_w>
\end{bmatrix}
\tag{2.17}
$$

The vectors $|JM>_n$ represent the electric and magnetic current coefficients for the nth Fourier mode of the basis functions which reside on S_{de} and are given by

$$
\begin{bmatrix}
|J_{de}> \\
|M_{de}>
\end{bmatrix}_n
\tag{2.20}
$$

The vector $|J_w>$ represents the current expansion coefficients for the currents that reside on the surface S_{wq}, $q=d$ or e, and is given by

$$
\begin{bmatrix}
|J_{wd}> \\
|J_{we}>
\end{bmatrix}
\tag{2.19}
$$

11

The matrix $[BB]_n$ is further partitioned as

$$
\begin{bmatrix}
([Z_{de,de}^{\circ}]+\eta_r[Z_{de,de}^{d}]) & ([Y_{de,de}^{\circ}]+[Y_{de,de}^{d}]) \\
([Y_{de,de}^{\circ}]+[Y_{de,de}^{d}]) & (-[Z_{de,de}^{\circ}]-\dfrac{1}{\eta_r}[Z_{de,de}^{d}])
\end{bmatrix}_n
\qquad (2.20)
$$

where $\eta_r^2 = \mu_q/\epsilon_q$, and a typical $[Z]$ or $[Y]$ matrix is of the form

$$
\begin{bmatrix}
[B_{tt}] & [B_{t\phi}] \\
[B_{\phi t}] & [B_{\phi\phi}]
\end{bmatrix}_n
=
\begin{bmatrix}
[B_{tt}] & -[B_{t\phi}] \\
-[B_{\phi t}] & [B_{\phi\phi}]
\end{bmatrix}_{-n}
\qquad (2.21)
$$

where $[B] = [Z]$ or $[Y]$, a square matrix of order N_t for each Fourier mode n. The integral expressions for the matrices $[BB]_n$ can be found in [22]. The matrix $[BW]_n$ is given by

$$
\begin{bmatrix}
\eta_r[Z_{de,wd}^{d}] & [Z_{de,we}^{\circ}] \\
[Y_{de,wd}^{d}] & [Y_{de,we}^{\circ}]
\end{bmatrix}_n
\qquad (2.22)
$$

and the matrix $[WB]_n$ is given by

$$
\begin{bmatrix}
\eta_r[Z_{wd,de}^{d}] & [Y_{wd,de}^{d}] \\
[Z_{we,de}^{\circ}] & [Y_{we,de}^{\circ}]
\end{bmatrix}_n
\qquad (2.23)
$$

The matrices $[BW]_n$ and $[WB]_n$ can be further partitioned as

12

$$[BW]_a = \begin{bmatrix} \eta_r[Z^d_{t,w}] & [Z^e_{t,w}] \\ \eta_r[Z^d_{\phi,w}] & [Z^e_{\phi,w}] \\ [Y^d_{t,w}] & [Y^e_{t,w}] \\ [Y^d_{\phi,w}] & [Y^e_{\phi,w}] \end{bmatrix}_a \quad \text{and} \quad [WB]_a = \begin{bmatrix} \eta_r[Z^d_{w,t}] & \eta_r[Z^d_{w,\phi}] & [Y^d_{w,t}] & [Y^d_{w,\phi}] \\ [Z^e_{w,t}] & [Z^e_{w,\phi}] & [Y^e_{w,t}] & [Y^e_{w,\phi}] \end{bmatrix}_a \quad (2.24)$$

The matrix $[BW]_a$ is of order $(4N_t \times p_w)$ and $[WB]_a$ is of order $(p_w \times 4N_t)$. An increase in computational efficiency can be obtained by using the relationship, $[WB]_a = \pm[BW]_{-a}^T$, where the $+$ and $-$ signs are used for the $[Z]$ and $[Y]$ matrices, respectively. The integral expressions for the matrix elements $[BW]_a$ are given in Appendix B. In all of the above matrices, $[Z_{\alpha,\beta}]$ represents the inner product $<\underline{w},\underline{E}(\underline{J})>$ or $<\underline{w},\underline{H}(\underline{M})>$, whereas $[Y_{\alpha,\beta}]$ represents the inner product $<\underline{w},\underline{E}(\underline{M})>$ or $<\underline{w},-\underline{H}(\underline{J})>$. Furthermore, the first subscript, α, identifies the component of the testing function, whereas the second, β, identifies the component of the basis function.

Finally, the matrix $[WW]$ is given by

$$\begin{bmatrix} [Z^d_{wd,wd}] & [0] \\ [0] & [Z^e_{we,we}] \end{bmatrix} \quad (2.25)$$

which also serves to illustrate the region isolation of the interior and exterior problems.

Since the final goal is the computation of input impedance, the following steps, which are in essence a "mode by mode" elimination procedure, can be performed to obtain the solution for the current coefficients, J_{wq}, from which the input impedance can be calculated.

13

$$|JM>_n = -[BB]_n^{-1} \bullet [BW]_{-n} \bullet |J_w>, \quad n=-N,\ldots,N \qquad (2.26)$$

These results can be substituted into the last equation system (last row) of (2.19) to obtain

$$\left[[WB]_{-n} \cdot [BB]_{-n}^{-1} \cdot [BW]_{-n} + \ldots + [WB]_0 \cdot [BB]_0^{-1} \cdot [BW]_0 + \ldots \right.$$
$$\left. + [WB]_n \cdot [BB]_n^{-1} \cdot [BW]_n - [WW] \right] |J_w> = -|V_w> . \qquad (2.27)$$

The wire current is easily obtained by inverting the bracketed term and multiplying the result by $|V_w>$. Even if quantities other than the impedance of the antenna are desired this can be an efficient approach. If storage is at a premium, the submatrices can be recomputed as necessary to determine other quantities, such as the currents on S_{da}. Alternatively, the matrix products indicated in the right side of (2.26) can be stored. Storage of these products will generally require less space than even the non-zero submatrices shown in (2.17).

CHAPTER 3

Theoretical and Experimental Results for DRAs with Coaxial Feed Probe Excitaion

3.1 Computer Code Verification

A general FORTRAN computer program was written to solve the boundary value problem formulated in Chapter 2. The geometry of Fig. 3.1a is that of a dielectric resonator antenna (DRA) excited by a coaxial probe extending through the bottom of a conducting ground plane. It is drawn as a rectangular cylinder for simplicity. To analyze such an antenna, it is necessary to invoke image theory to remove the ground plane. Removal of the ground plane results in the equivalent imaged problem of a DBOR excited by a dipole as illustrated in Fig. 3.1b.

As a preliminary check to establish the validity of the computer code, the input impedance of the hemispherical dielectric resonator antenna (HDRA) of Ref. [2] was computed as a function of frequency. These computed impedances are plotted together with computed impedances obtained from the dyadic Green's function analysis [23] and with the measured input impedance. As can be seen from Fig. 3.2, the results obtained from the two different analytic techniques are in very good agreement. Note that the resonant curves of the theoretical input impedances are shifted to a lower frequency than that of the measured impedance and that the reactance of the theoretical impedances are less capacitive than the measured reactance. It is believed that these discrepancies are due to an effect which is very similar to that of a very thin air gap between a dielectric resonator and the conducting surfaces on which it resides [24-26].

In order to verify a theoretical model experimentally, it is necessary to have a test device which represents the ideal situation as closely as possible. Therefore, to ensure that there would be no air gaps between the dielectric material and the conducting surfaces, a CDRA was constructed out of a section of PVC tube packed with "Hi K Powder" manufactured by Emerson & Cuming, Inc. as shown in Fig. 3.3. The 2.6cm PVC tube with an inner radius a=2.75cm and

a wall thickness of 2.5mm was fastened directly to a ground plane with silicone rubber adhesive. To accommodate both thin ($a_w = 0.381$mm) and comparatively thick ($a_w = 1.295$mm) feed probes, both SMA and N type connectors were used. Measurements were made using an HP-8510B network analyzer. Since the permittivity of the PVC container is low, and the antenna is a resonant structure, the container was neglected in the numerical model. To excite the HEM_{11} mode, the feed probe was positioned at $\rho_f = 1.4$cm. The source free resonant frequency of the CDR was computed to be 1.377 GHz by using the technique described in [27]. Fig. 3.4 plots both experimental and computed input impedances as a function of frequency. As can be seen, the experimental and theoretical results are in better agreement than the case of the HDRA. One observes slight variations in resonant frequency and impedance levels when computed impedances are compared to those obtained by measurements. The greatest variations in impedance levels occur for the thicker feed probe.

An experiment was conducted to further investigate these discrepancies in input impedance levels. To ascertain whether or not the wire end caps had any effect upon the input impedance, both hollow and solid coaxial feed probes were used with the CDRA of Fig. 3.3. The feed probes were made from K&S Engineering's #163 3/32" (0.238125cm) diameter rod and #118 3/32" diameter tube. The 1.9cm feed probe was positioned at $\rho_f = 1.28$cm. As can be seen from Fig. 3.5, the end cap effect is negligible. The slight difference in measured impedance levels can be attributed to experimental error. However, when the 20x20cm ground plane was extended by approximately a quarter free space wavelength at the center frequency, without disturbing the test antenna, the measured impedance level approached that of the computed impedance as can be seen in Fig. 3.6. This is not surprising for a feed probe in this position since it also excites a zero order mode component [27]. Therefore, these results suggest that finite ground plane effects as well as thin wire theory inadequacies have introduced errors. Other experimental and computed

16

results can be found in Appendix A.

3.2 Air Gap Study

3.2.1 The effect of an air gap between the bottom of a CDR and the ground plane

When a dielectric resonator (DR) resides directly on a conducting ground plane and is fed by a coaxial probe through the bottom of the ground plane, the excited DR modes useful for antenna purposes tend to be those with a strong electric field component normal to the ground plane. Failure to insure complete electrical contact between the bottom of the DR and the ground plane can result in very thin air gaps at the dielectric and conductor interface. If the DR is composed of a material of high dielectric constant, and an air gap is introduced between the DR and the ground plane, the electric field component normal to the ground plane will be much stronger in the air gap than it is just inside the DR. Because of this, the resonant frequency and input impedance of the antenna can be significantly influenced. A theoretical investigation into the effect of an air gap between two unexcited dielectric resonators isolated in free space has been reported in [24]. This study did not consider the effect of conductors embedded in the dielectric upon resonant frequency, nor did it consider the effect upon input impedance of an actual radiating structure. The intent of this section is to present the results of an experimental and numerical investigation which illustrates the effect of an air gap on the input impedance and resonant frequency of a DR antenna which is excited by a coaxial probe [25-26].

Fig. 3.7 illustrates the antenna under test. The antenna is in essence that of Fig. 3.3, except that an annular styrofoam spacer is used to simulate an air gap between the bottom of the CDR and the ground plane. The dimensions of the annular styrofoam spacer (air gap) are denoted as the following: height, h_g=0.152mm; inner radius, r_g=2.92mm; outer radius, 30mm. The spacer thickness varies from 0.0008 to .001 free space wavelengths over the frequency range of operation. The feed probe, which is soldered to an SMA connector, is of length l_w and radius

a_w. Silicone rubber adhesive was used to fasten the PVC container directly to the ground plane for the "no air gap" test case. For the air gap test case, the styrofoam spacer was glued to the bottom of the container and then to the ground plane. A small amount of adhesive was used around the SMA connector on the ground plane to insure that the powder would not get under the spacer. To excite the TM_{01} mode, the PVC container was positioned so that the container and the feed probe were concentric.

Again, since the permittivity of the PVC container is low, and the antenna is a resonant structure, the container has been neglected in the numerical model. After invoking image theory and removing the ground plane, the original antenna was analyzed as a body of revolution (BOR) composed of a dipole antenna surrounded by a dielectric cylinder isolated in free space using the numerical code described in [28].

Fig. 3.8 is a plot of input impedance as a function of frequency for the test antenna of dimensions r_a=2.75cm, r_b=3.0cm, h=2.6cm, a_w=0.381mm and l_w=1.369cm. As can be seen from the figure, the comparison between measured and computed input impedances for h_g=0.0 is very good. For this case, the frequencies at which the peak values of input resistance occurs are at 1.852GHz and 1.864GHz for the measured and computed curves, respectively. For the numerical model, it was necessary to increase h_g=0.152mm by 0.051mm in order to obtain results which compared as favorably as in the h_g=0.0mm case. This additional spacing, which could not be measured for the actual antenna, could easily have been introduced during the antenna fabrication. As can be seen from Fig. 3.8, the introduction of an air gap causes a change in both resonant frequency and impedance levels. The resonant frequency shifts to 1.936GHz and 1.924GHz for the measured and computed cases, respectively.

In order to demonstrate how pronounced the effect of an air gap upon the input impedance and resonant frequency of this class of antennas of different permittivity operating at higher

18

frequencies can be, the following numerical study was conducted. The dimensions of the DR antenna as shown in Fig. 3.7, with $\epsilon_r = 4.0$, were selected so that the TM_{01} mode was excited near 4.25Ghz for the case $h_s = 0.0$. The dimensions of this antenna are as follows: $r_a = 1.9174$cm, $h = 3.852$cm, $a_w = 0.433$mm, and $l_w = 1.15$cm. The input impedance of this antenna is plotted as a function of frequency together with input impedance of the same antenna with air gaps, $h_s = 0.01$mm and $h_s = 0.05$mm, when $r_s \rightarrow a_w$ as a function of frequency, and plotted in Fig. 3.9. The antenna was then scaled so that it would operate at the same frequency for three other dielectric constants. The input impedance for these antennas was computed for the same two gap spacings as was the $\epsilon_r = 4.0$ antenna. The dimensions of the scaled antennas with $\epsilon_r = 8.9$, 16.0, and 22.0 are given in the figure captions of their impedance plots, Figs. 3.10 through 3.12, respectively. There are three interesting observations which can be made concerning these series of figures. The first is that the air gap causes the antenna resonant frequency to shift upward. The amount of shift being proportional to the resonator's dielectric constant. The second is that the air gap causes a broadening of the resonant curves which is an indication of a lowering of the antenna Q factor. The third is that intentional introduction of low permittivity material between the bottom of the DR and the ground plane should result in a more effective radiator with improved bandwidth. From what was originally considered to be a fabrication imperfection, one has uncovered possible ways to improve antenna performance. It should be pointed out that this study was conducted only on the TM_{01} DR antenna mode, however, similar behavior may be expected for other DR antenna modes which have a strong component of electric field normal to a conducting surface.

3.2.2 The effect of an air gap surrounding the coaxial feed probe of a DR antenna

When a dielectric resonator (DR) antenna is fed by a coaxial probe, the electromagnetic field boundary conditions demand that the electric field lines terminate normally to the surface of the

19

feed probe. Since the normal component of the electric field is discontinuous across a surface separating two media of different permittivities, the introduction of a thin air gap between the feed probe and a high permittivity DR may have a significant effect upon the input impedance and resonant frequency of the antenna. The intent of this section is to present the results of an experimental investigation which demonstrates the effect of an air gap surrounding the feed probe of a dielectric resonator antenna. Fig. 3.13 illustrates the antenna under test. In this study, the air gap between the dielectric material and the feed probe is simulated by inserting the feed probe (a_w=0.381mm) into a teflon tube (ϵ_r=2.1) with an inner radius of 0.3968mm and wall thickness t=0.3968mm, as illustrated in section cut A-A of Fig. 3.13. Since electrical lengths are inversely proportional to the square root of ϵ_r, the use of a teflon tube to simulate an air tube is reasonable.

Using the technique presented in [27], the source free resonant frequencies for the TM_{01} and HEM_{11} modes for the CDR under consideration (without the presence of the feed probe) were found to be 2.029GHz and 1.377Ghz, respectively. To excite the TM_{01} mode, a feed probe of length l_w=1.5cm positioned at ρ_f=0.0cm was used. Fig. 3.14 plots the input impedances vs. frequency for TM_{01} mode. As can be seen, the resonant frequency shifts from 1.68GHz to 1.92Ghz and the magnitude of the resonant impedance is reduced upon introduction of the air gap. Inserted in Fig. 3.14 is a plot of the return loss as a function of normalized frequency. The return loss is given to show that the frequency obtained from the return loss minimum is not an indication of the resonant frequency of the antenna. The frequency at which the return loss is minimum for both antennas is near the predicted resonant frequency for the source free CDR. Note that unlike the antenna without the air gap, the resonant frequency of the antenna with the air gap is near the frequency at which the return loss is a minimum. The 10dB bandwidth of both antennas is about the same; however, the antenna with the gap is a better 50Ω match. The

20

10dB bandwidth of the no gap antenna appears to be wider only because of the influence of the next higher zero order mode. Also obvious from inspection of Fig. 3.14 is that introduction of the air gap shifts the next higher zero order mode up in frequency.

To excite the HEM_{11} mode, a feed probe of length $l_w = 2.18$cm positioned at $\rho_f = 1.4$cm was used. The measured input impedances are presented in Fig. 3.15. The effect of the air gap upon this antenna is similar to that of the antenna operating in the TM_{01} mode. Upon introduction of the gap, the resonant frequency shifts from 1.278GHz to 1.326GHz and the magnitude of the resonant impedance is reduced. For this mode, introduction of the air gap slightly decreases the 10dB bandwidth, but does not improve the 50Ω match. The frequency at which the return loss is minimum is near that of the predicted source free resonant frequency of the CDR. Though not as obvious, the antenna with the air gap increases the resonant frequency of the next higher order mode. This effect can be seen by observing that R_{in} begins to increase near 1.425GHz for the no gap antenna while it continues to decrease for the antenna with the air gap.

3.3 Parametric Study of Dielectric Resonator Antennas Excited by a Coaxial Probe

In order to demonstrate how the computer code written to solve the system of equations developed in Chapter 2 can be used to investigate the theoretical performance of a CDRA operating in the HEM_{11} mode, parametric studies based upon the computation of input impedance of the antenna as shown in Fig. 3.1a were performed. The CDRA under consideration has a radius of 1.283 cm and a height of 2.566 cm. The diameter of the coaxial feed probe is 0.0236 cm. The source free resonant frequency of the cylindrical dielectric resonator (CDR) of material parameters $\epsilon_r = 8.9$ and $\mu_r = 1.0$ was determined to be 2.72 GHz by using the technique described in [27]. Therefore, the parametric study was conducted over the frequency range of 2.0 to 3.2 GHz. It should be pointed out that this computed resonant frequency did not include the effect of the feed structure. Henceforth, the resonant mode of the source free (no feed probe) CDR

shall be prefixed with "pure", and that of the perturbed CDRA without any additional description.

The HEM_{11} mode consists primarily of the ± 1 Fourier modes of the basis and testing functions used in the Galerkin procedure. When the HEM_{11} mode is strongly coupled to the feed structure, the computed impedance matrix elements in the coupling blocks [BW] and [WB] of equation (2.17) for $n = \pm 1$ will be significantly larger in magnitude than those of any other Fourier mode index n. This means that $|JM>_{\pm 1}$ of equation (2.26) has the most influence on the bracketed term of equation (2.27) and that close to the resonant frequency of the HEM_{11} mode, the ± 1 Fourier modes are sufficient for convergence. Hence, one would expect that this strong ± 1 mode coupling would manifest itself as a sharp resonant response observable in the impedance versus frequency plots. Although the ± 1 modes are dominant, the modes $n = -4$ to $+4$ were used in all of the computations.

Fig. 3.16 plots the computed input impedance as a function of frequency for various feed positions ρ_f. Fig. 3.17 is a plot of the peak value of input resistance (R_{in}) as a function of feed position. Also included in Fig. 3.17 is the frequency at which this peak value occurs. From the study of Figs. 3.16 and 3.17, the HEM_{11} mode is observed to be dominant for feed positions of $0.4 < \rho_f < 1.2$ cm as evident from the steep resonant curves of R_{in} versus frequency of Fig. 3.16 and the operating frequency indicated in Fig. 3.17. The strong resonant behavior is also reflected in Fig. 3.16 by the steep slope of the reactance versus frequency curves. Evident from Fig. 3.17 is that the peak value of R_{in} begins to drop for $\rho_f > 1.1$ cm and falls dramatically when the feed probe is just outside the resonator. When the probe is outside the resonator, its length is only $.14\lambda$. Being so short, it is not an efficient radiator and as such is highly capacitive and weakly

22

coupled to the resonator. Note that the input reactance is more capacitive for the case of $\rho_f = 1.566$cm than it is for the case of $\rho_f = 1.326$cm. This trend for increasing capacitance will continue as the feed probe moves further away from the CDR until the system becomes completely decoupled. The strongly coupled DBOR modes contribute inductive reactance to the input impedance. Hence, for this structure, X_{in} does not cross the zero axis when the probe is outside the CDR. Fig. 3.17 indicates that the peak value of resistance occurs at a frequency of 2.77 GHz for all three feed locations $\rho_f > 1.283$ cm (outside the resonator). This is an indication that the pure HEM_{11} mode is not greatly disturbed by the presence of the short monopole. Thus, placing the probe outside the resonator also can be used to measure the resonant frequency of the DR for some modes to verify computed resonant frequencies. For feed positions $\rho_f < 0.75$ cm, Fourier modes other than the ± 1 are coupled to the coaxial probe as evidenced by the broadening of the frequency response curves for R_{in}. Hence the purity of the HEM_{11} mode will be affected by the feed locations since other radiating modes are being excited.

Another interesting study which produced useful information is that of fixing the feed position at $\rho_f = 0.962$cm, and varying the length of the feed l_w. The input impedance is plotted in Fig. 3.18. The peak value of R_{in} versus l_w is plotted in Fig. 3.19 together with the frequency at which this peak value occurs. From Fig. 3.19, one sees that the HEM_{11} mode is strongly excited for $1.25 < l_w < 1.75$ cm. This observation is made based upon the steep slope of R_{in} and X_{in} as a function of frequency and the high peak values of R_{in}. Also evident is that the resonant frequency, i.e., that frequency at which R_{in} achieves a maximum, drops for increasing probe length. Fig. 3.19 is interesting in that for $l_w < 1.1$ cm, the peak value of R_{in} occurs at frequencies from 2.7

23

to 2.77 GHz. This range of frequencies is close to the resonant frequency of the pure HEM_{11} mode. One also observes that upon increasing l_w, the frequency at which R_{in} achieves a maximum drops. This is as expected since it is well known from perturbational theory [20] that when a conductor is introduced into a cavity where the $\underline{E}$ field is strong, the cavity's unperturbed resonant frequency drops. Fig. 3.20 plots the input impedance as a function of normalized frequency to better illustrate the resonant response when the permittivity of the CDRA is varied. From this figure it can be seen that for the higher permittivity materials, the resonant response becomes sharper. This is as expected since increasing the permittivity for a fixed dimension resonator results in a higher Q-factor. Also evident from the previous data is that a small resonator made of high permittivity material should give the same performance as that of a much larger resonator made of a lower permittivity material. Fig. 3.21 shows the effect of the DR a/h ratio on the input impedance. This figure shows that the DR parameters, a, l, and h, can also be used to control the resonant frequency and the input impedances.
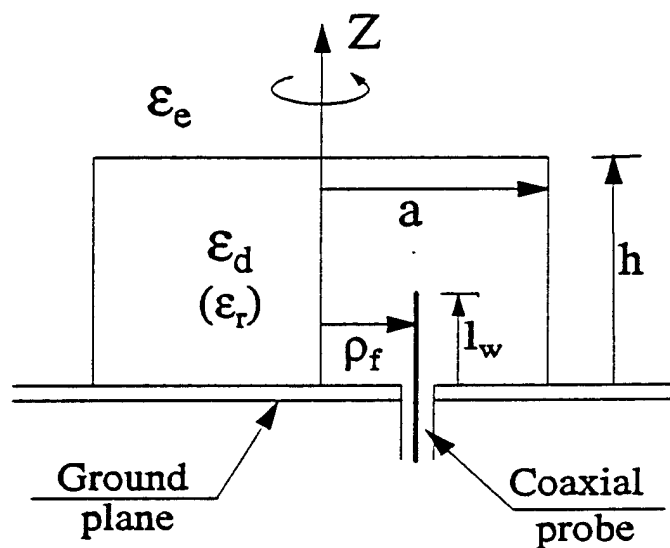
Fig. 3.1a. Geometry of the CDRA.
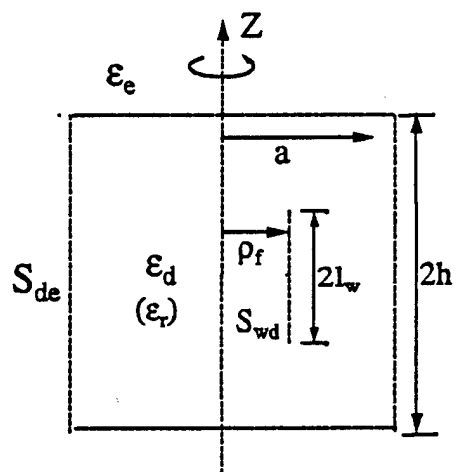
Fig. 3.1b. The equivalent imaged problem.

25
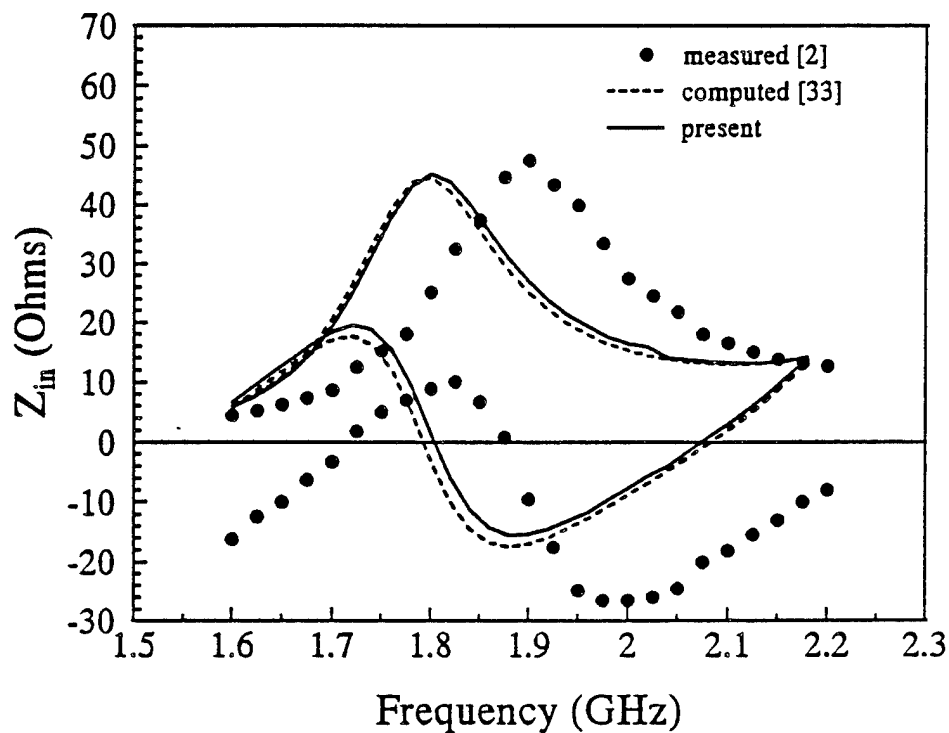
Fig. 3.2 Input impedance vs. frequency for the coaxial probe fed hemispherical dielectric resonator antenna. $\epsilon_r = 8.9$, tan $\delta = 0.0038$, a=2.54, $\rho_f = 1.74$cm, $a_w = 0.075$cm, $L_w = 1.52$cm.
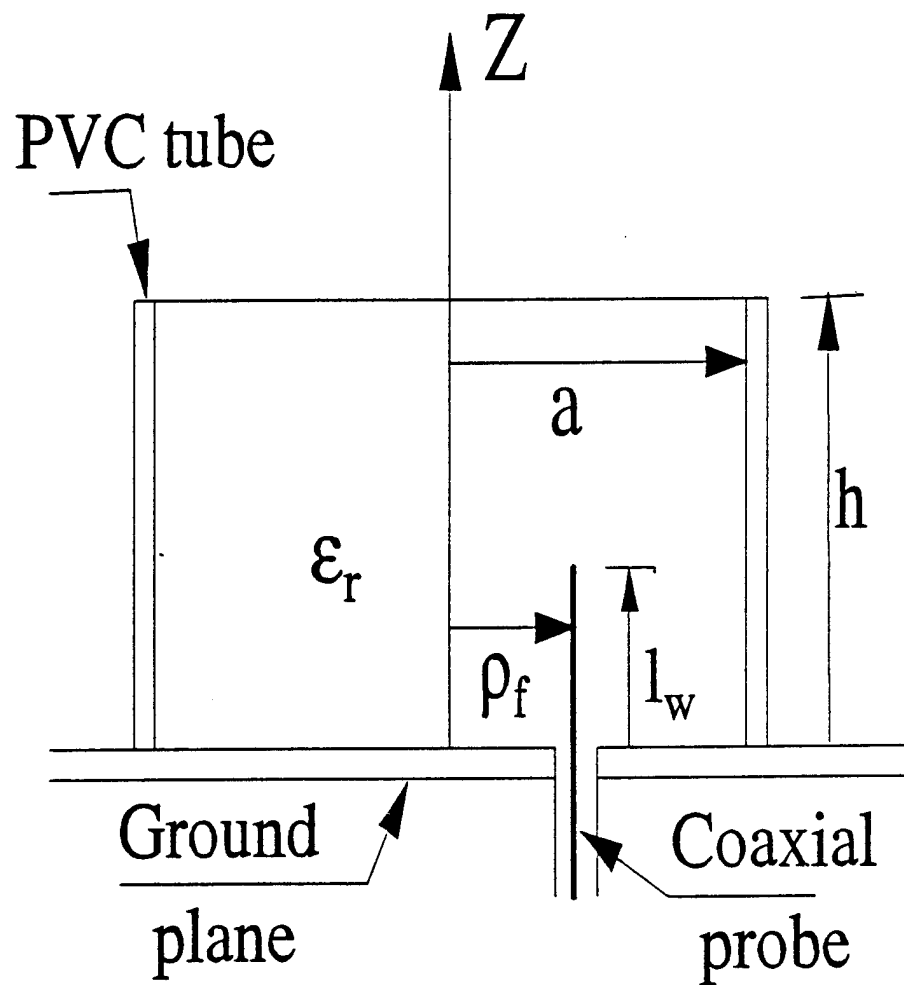
Fig. 3.3. Geometry of the powdered CDR antenna.
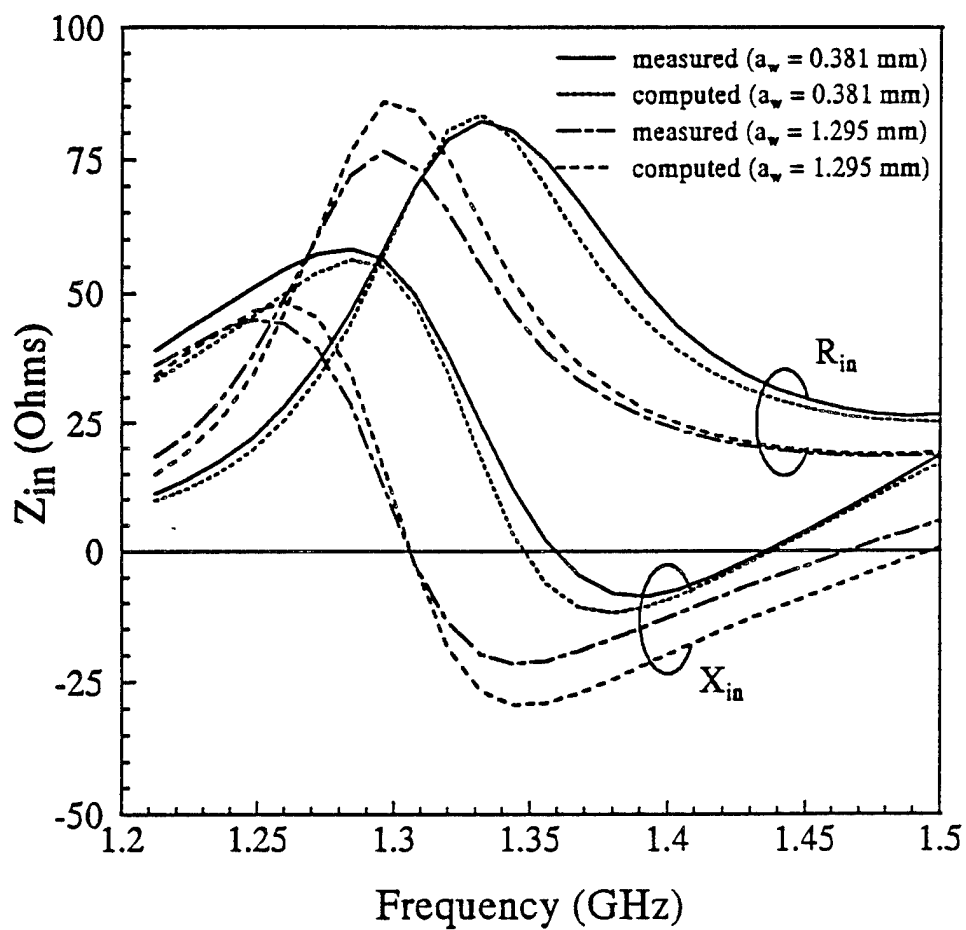
Fig. 3.4 Input impedance vs. frequency for the powdered CDRA. $\epsilon_r = 12.0$, a=2.75cm, h=2.6cm, $\rho_f = 1.4$cm, $l_w = 2.0$cm.

28
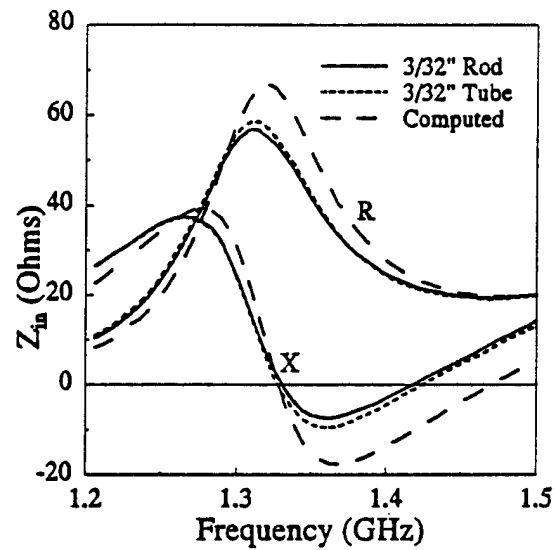
Fig. 3.5. Input impedance vs. Frequency for CDRA with different feed probes with ρ_f=1.28cm, $2a_w$=3/32", l_w=1.9cm, a=2.75cm, t=0.0, and h=2.6cm.
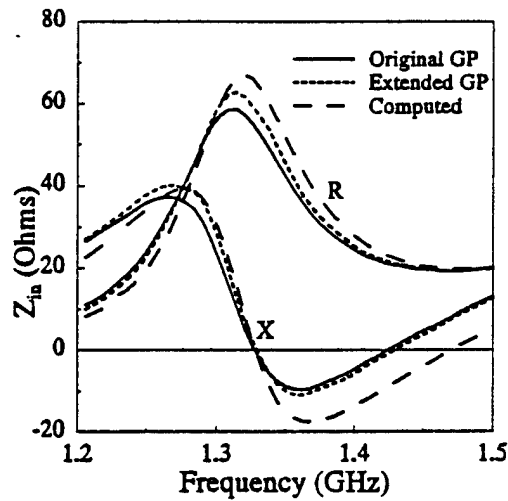
Fig. 3.6. Input impedance vs. Frequency for CDRA fed by tube probe using different ground planes with ρ_f=1.28cm, $2a_w$=3/32", l_w=1.9cm, a=2.75cm, t=0.0, and h=2.6cm.

29
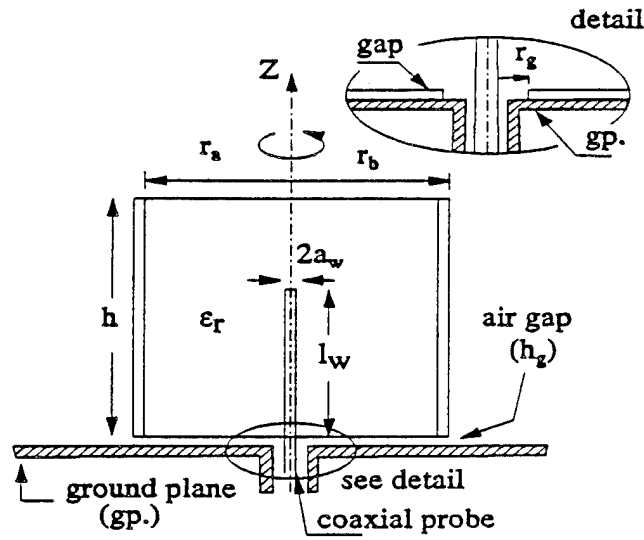
Fig. 3.7. Geometry of the antenna with air gap between the bottom of the DR and the ground plane.
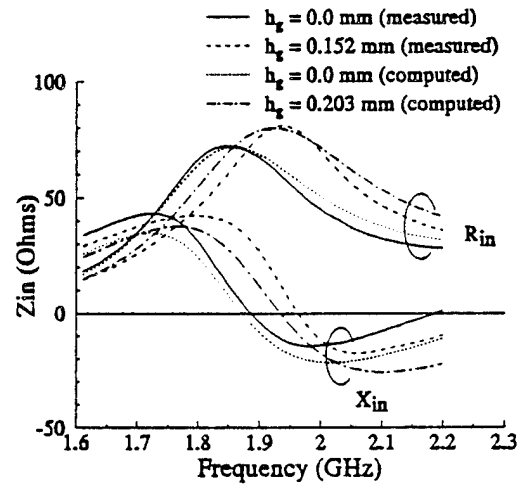
Fig. 3.8. Input impedance vs. frequency for the test antenna of Fig. 3.7. r_a=2.75cm, r_b=3.0cm, h=2.6cm, a_w=0.381mm, l_w=1.369cm, ϵ_r=12.0

30
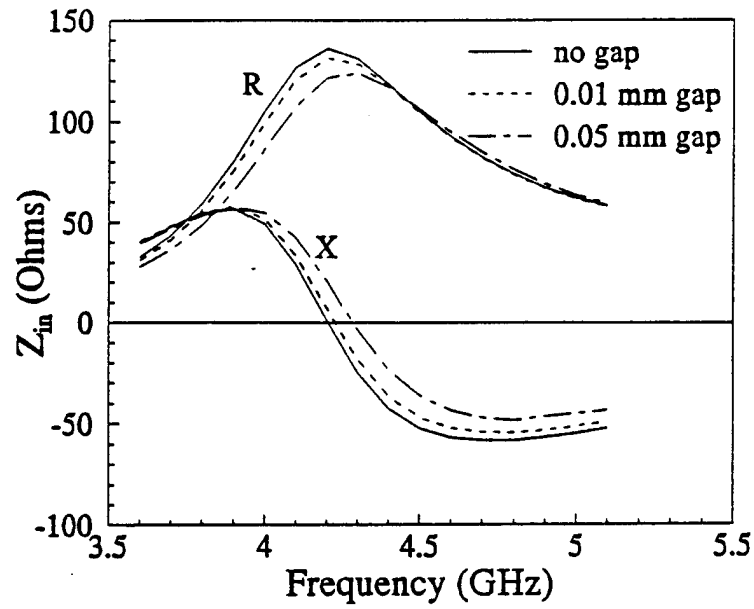
Fig. 3.9. Z_{in} vs. freq. $\epsilon_r = 4.0$, $r_a = 1.9174$cm, $h = 3.852$cm, $a_w = 0.433$mm, $l_w = 1.15$cm.
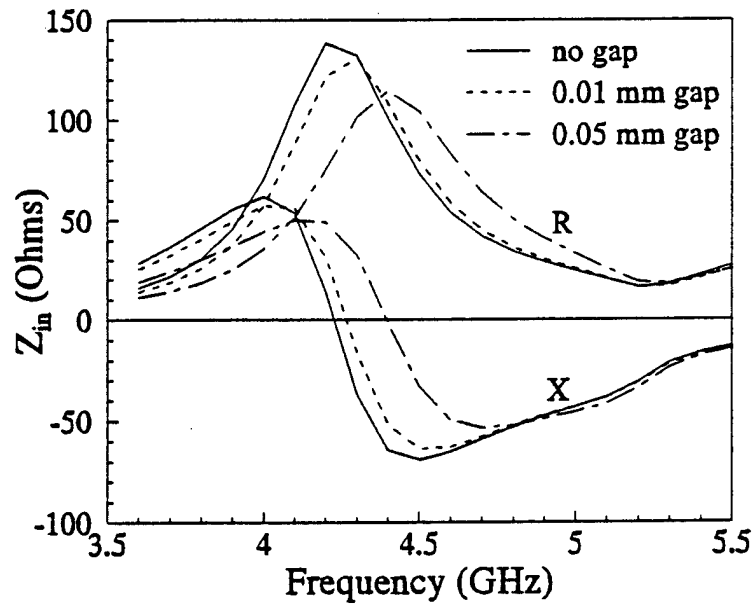
Fig. 3.10. Z_{in} vs. freq. $\epsilon_r = 8.9$, $r_a = 1.285$, $h = 2.582$cm $a_w = 0.29$mm, $l_w = 7.72$mm.
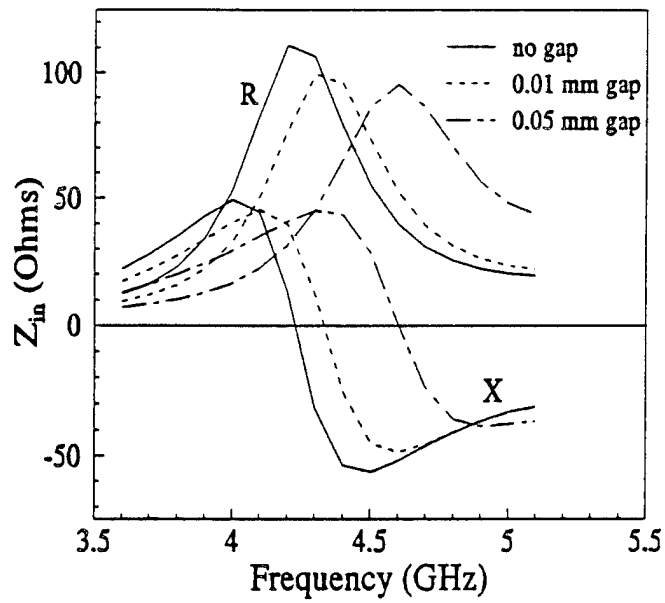
Fig. 3.11. Z_{in} vs. freq. $\epsilon=16.0$, $r_a=9.587$mm, $h=1.926$cm, $a_w=0.2165$mm, $l_w=5.75$mm.
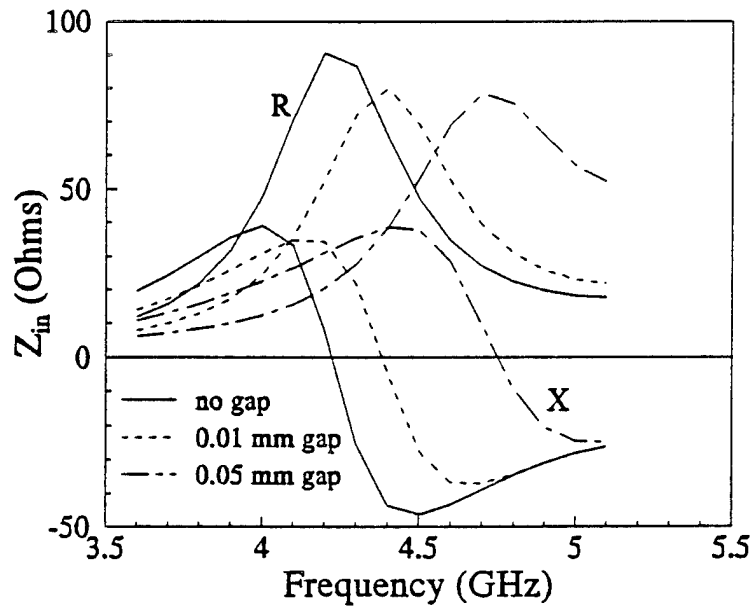
Fig. 3.12. Z_{in} vs. freq. $\epsilon=22.0$, $r_a=8.17$mm, $h=1.642$cm, $a_w=0.185$mm, $l_w=4.91$mm.

32
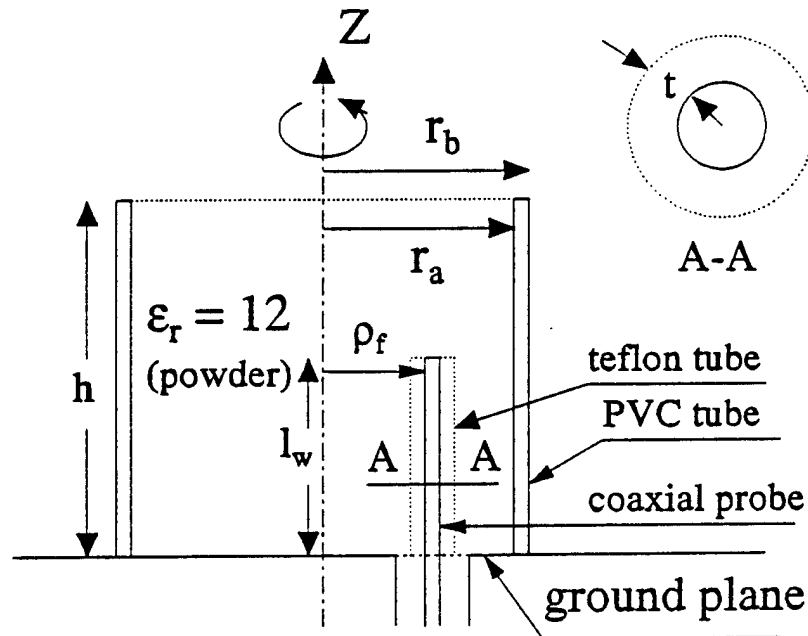
Fig. 3.13. Geometry of the antenna with air gap around the coaxial probe.
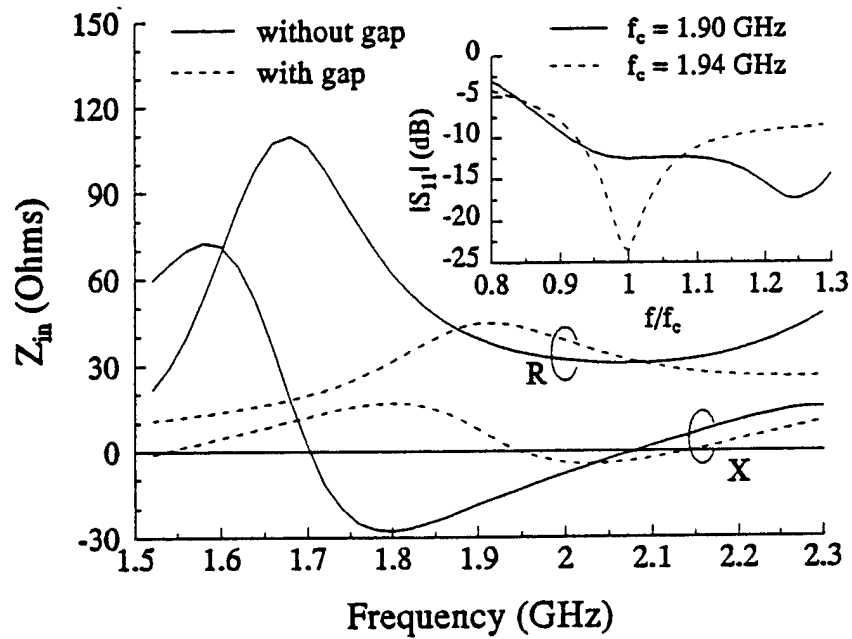
Fig. 3.14. Input impedance vs. frequency for the test antenna of Fig. 3.13.
r_a=2.75cm, r_b=3.0cm, h=2.6cm, ρ_f=0.0cm, a_w=0.381mm, t=0.3968mm,
l_w=1.5cm.

33
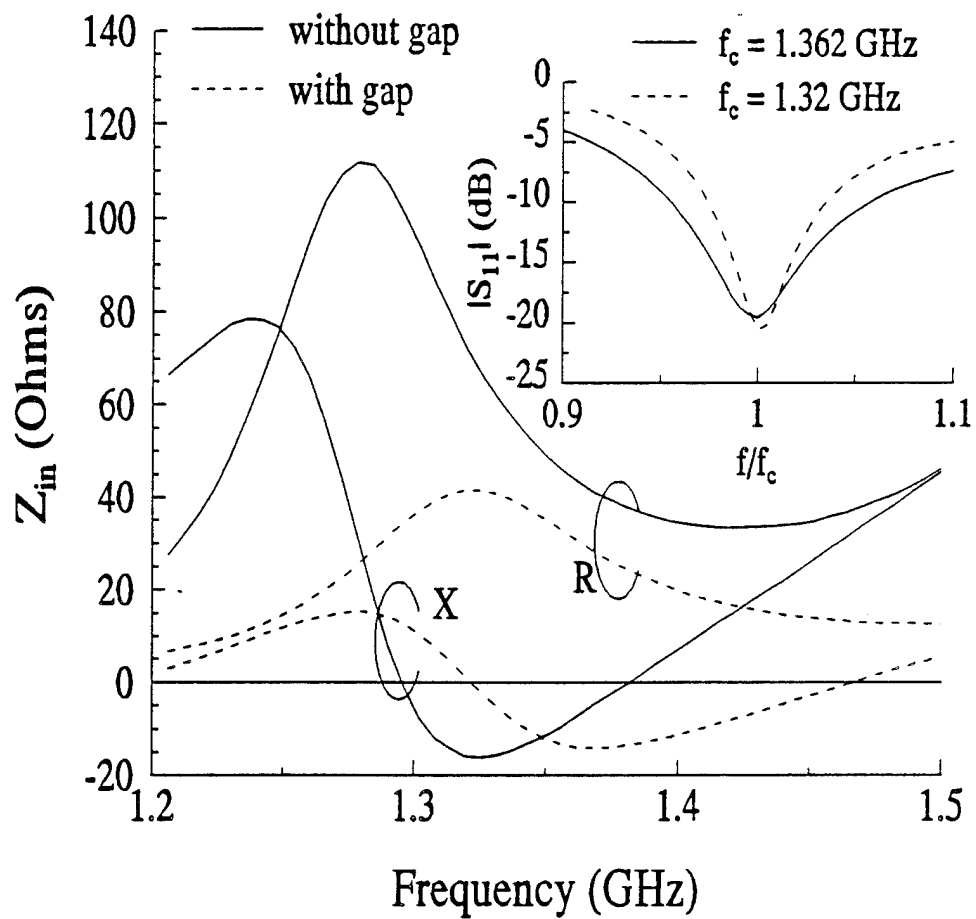
Fig. 3.15 Input impedance vs. frequency for the test antenna of Fig. 3.13.
r_a=2.75cm, r_b=3.0cm, h=2.6cm, ρ_f=1.4cm, a_w=0.381mm, t=0.3968mm,
l_w=2.18cm.

34
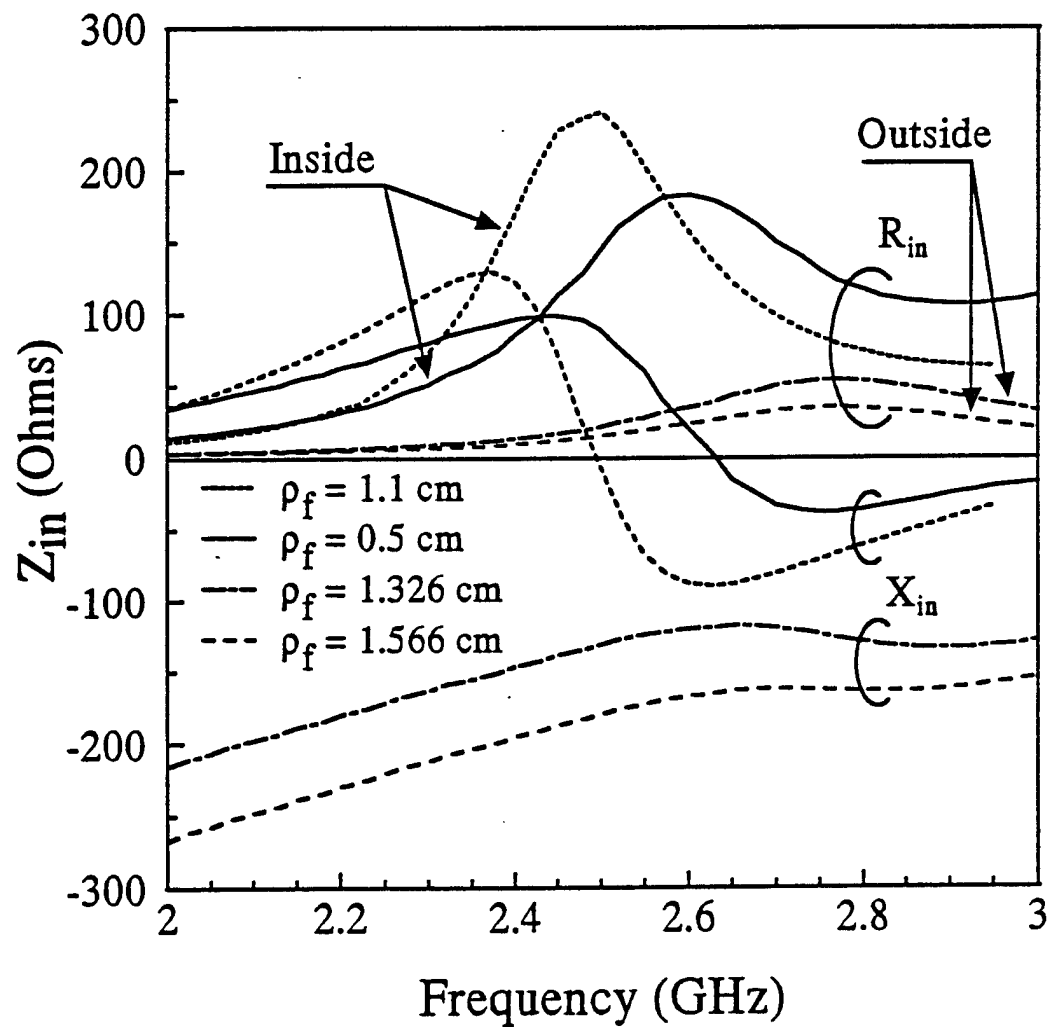
Fig. 3.16 Effect of coaxial probe feed position on the antenna input impedance. $\epsilon_r = 8.9$, $h = 2.566$cm, $a = 1.283$cm, $a_w = 0.0118$cm, $l_w = 1.5$cm.

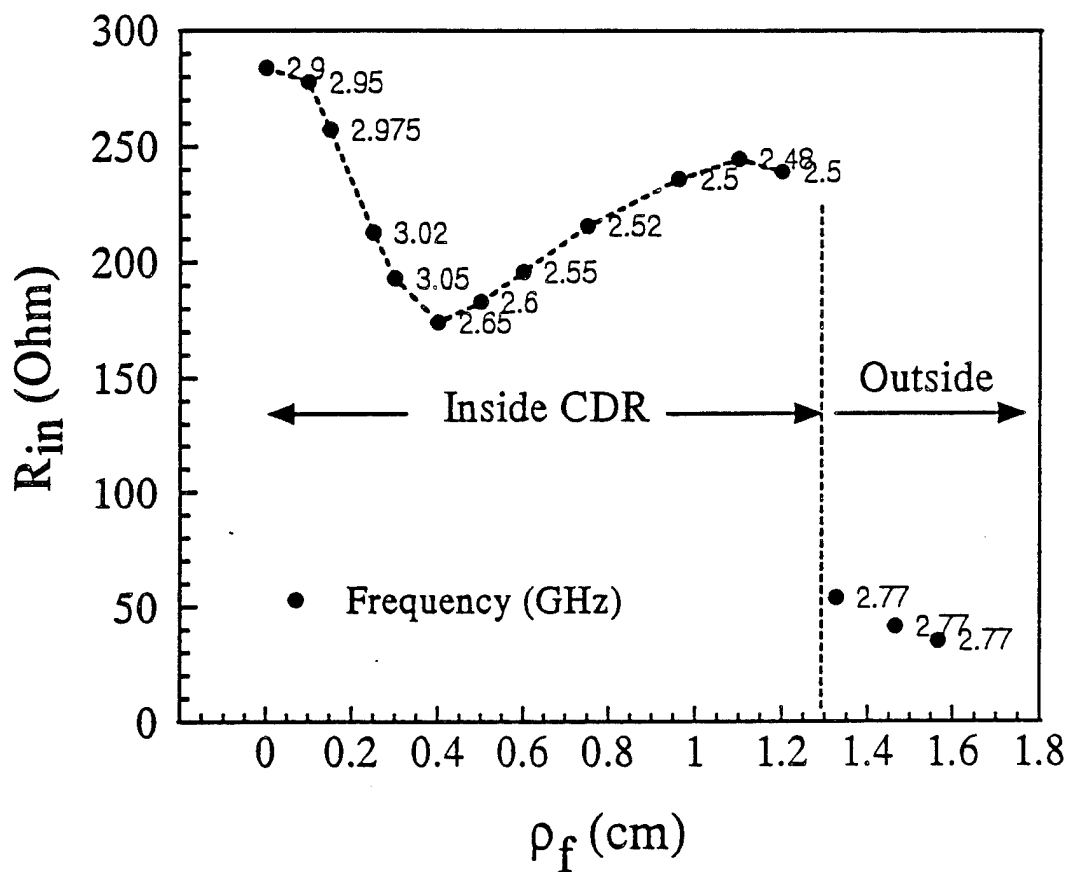Fig. 3.17 Effect of coaxial feed probe position on the peak value of the antenna input resistance. $\epsilon_r = 8.9$, h=2.566cm, a=1.283cm, $a_w = 0.0118$cm, $l_w = 1.5$cm.
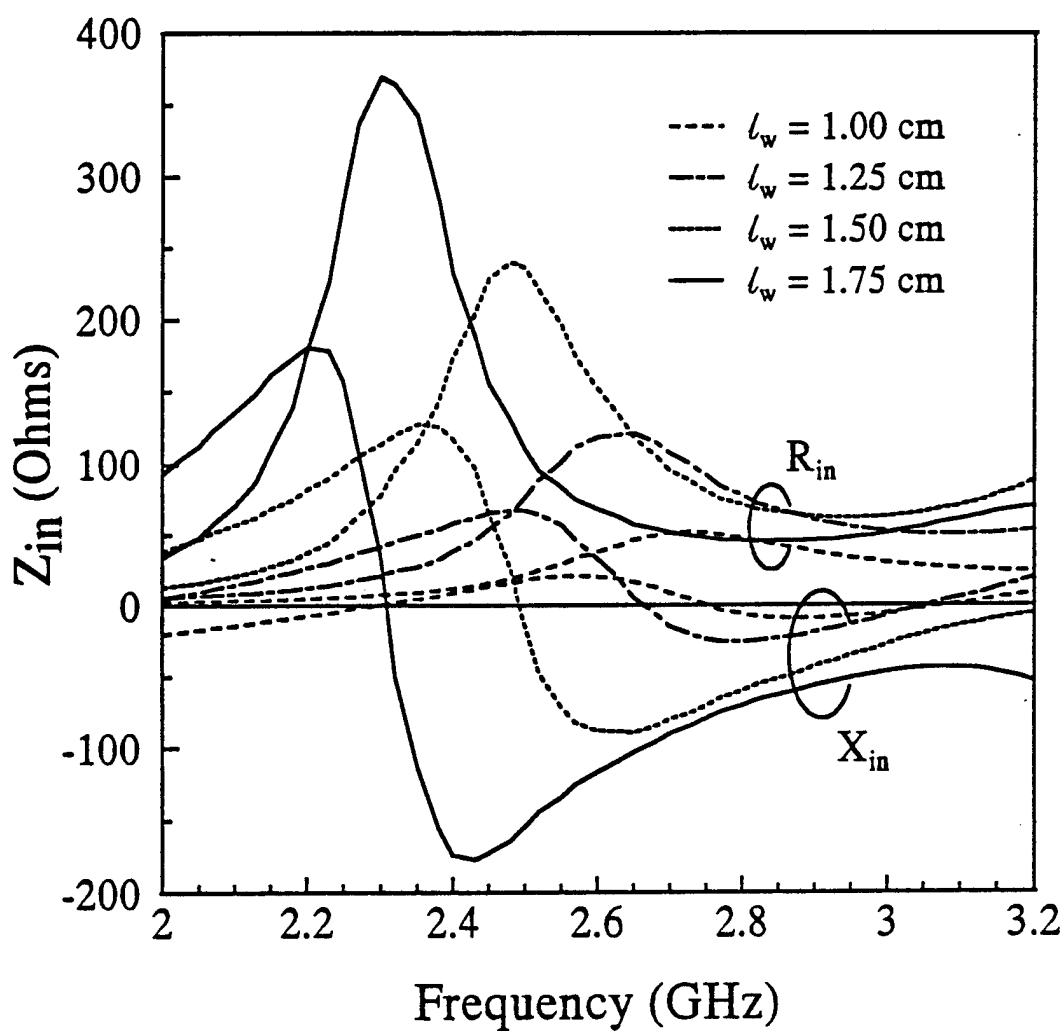
Fig. 3.18 Effect of coaxial probe length on the antenna input impedance. $\epsilon_r = 8.9$, h=2.566cm, a=1.283cm, a_w=0.0118cm, ρ_f=0.962cm.
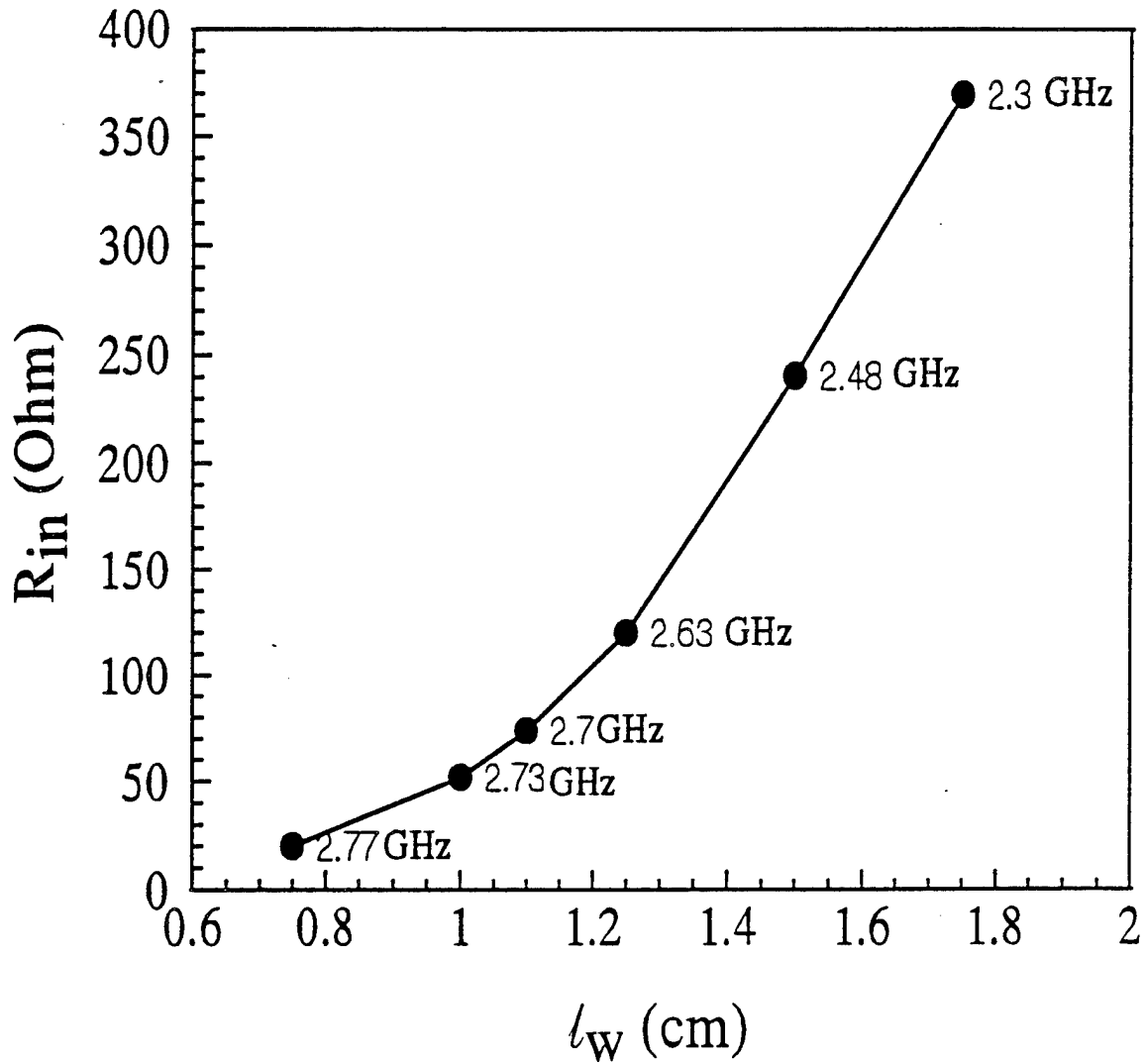
Fig. 3.19 Effect of coaxial feed probe length on the peak value of the antenna input resistance. $\epsilon_r = 8.9$, h=2.566cm, a=1.283cm, a_w=0.0118cm, ρ_f=0.962cm.
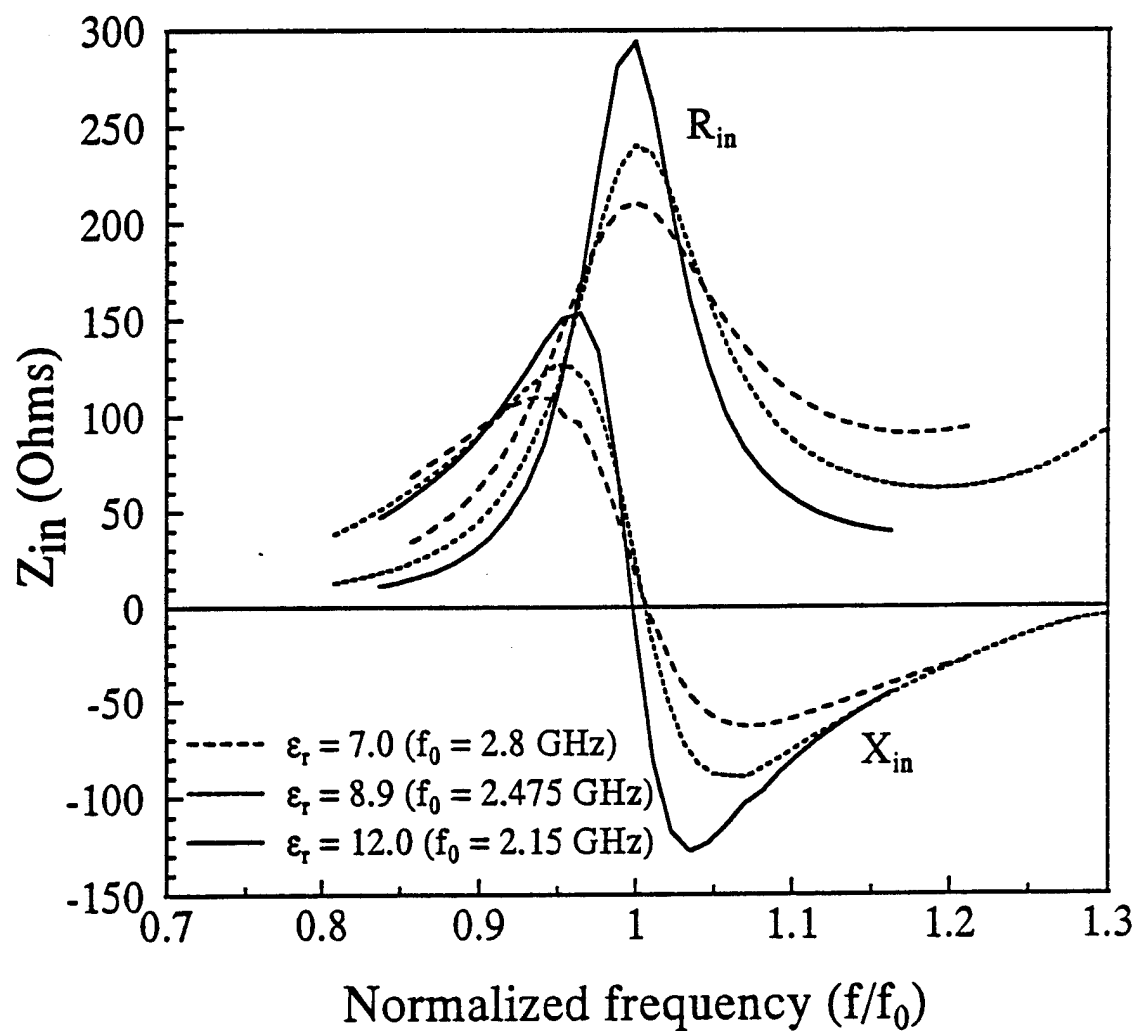
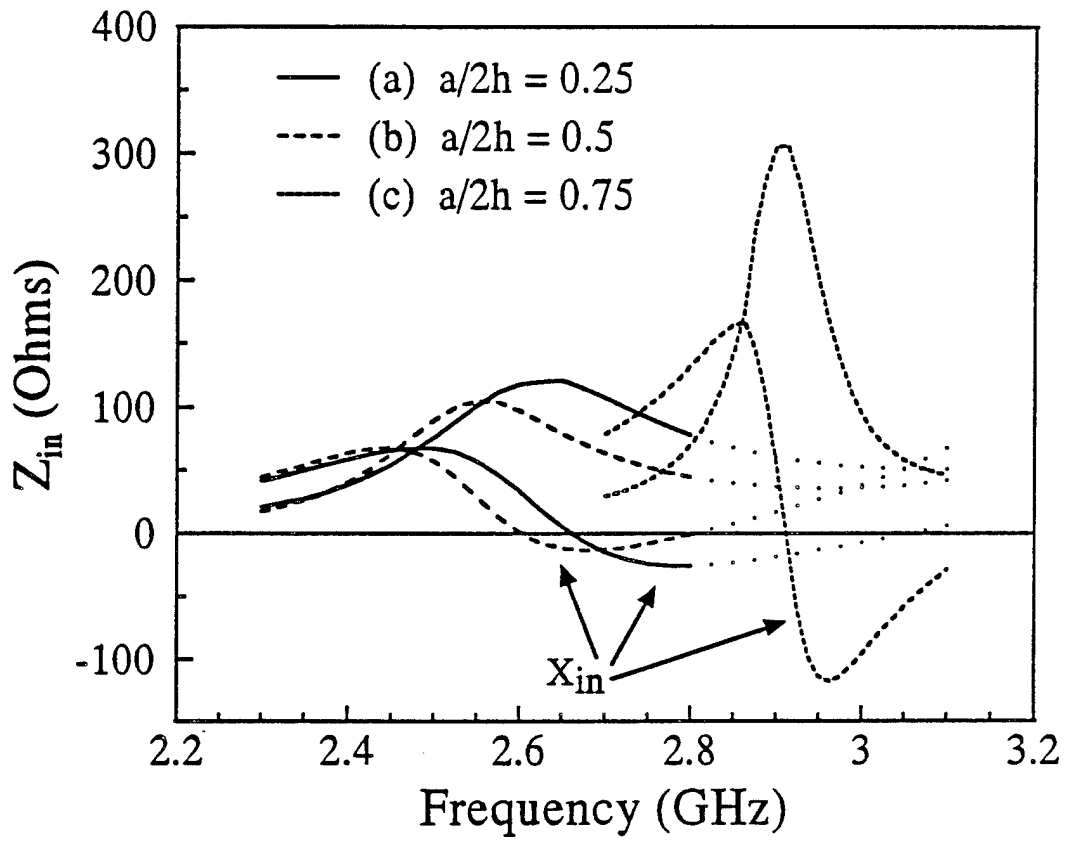Fig. 3.20 Effect of permittivity on antenna input impedance. h=2.566cm, a=1.283cm, a_w=0.0118cm, ρ_f=0.962cm,L_w=1.5cm, modes -3 to +3.

Fig. 3.21 Effect of various a/h ratios on antenna resonant impedance. $\epsilon_r = 8.9$; a) a/2h = 0.25: h = 1.588cm, a = 1.283cm, l_w = 1.25cm, ρ_f = 0.962cm, a_w = 0.0118cm; b) a/2h = 0.5: h = 1.6cm, a = 1.6cm, l_w = 1.25cm, ρ_f = 1.2cm, a_w = 0.0118cm; c) a/2h = 0.75: h = 1.5cm, a = 2.25cm, l_w = 1.25cm, ρ_f = 1.69cm, a_w = 0.0118cm.

CHAPTER 4

Thin Slot Apertures Coupled to Dielectric Bodies of Revolutions

As discussed in Chapter 1, the driving force behind this work is to build a numerical electromagnetics code which can be used to design small efficient dielectric resonator antennas. Chapter 2 formulated a system of equations for the boundary value problem of thin wire radiators coupled to DBORs and solved them via the MoM. Chapter 3 was devoted to the study of coaxial probe fed dielectric resonator antennas by implementing the formulation developed in Chapter 2. In most applications, coaxial probe feeds are normally used to couple with the electric field lines. Closed loop feed probes may be used to couple with the magnetic field lines of a DR mode. These closed loop probes create fabrication problems, especially when they are located within the DR. It has been established experimentally that a narrow slot can excite a DR in such a way as to cause it to operate efficiently [29,30]. Hence, a narrow slot aperture in a ground plane should be a cost effective alternative to closed loop wire feed probes for magnetic field line coupling. To couple with the desired resonator mode, and to achieve proper matching with the source, the slot aperture must be properly adjusted. Therefore, an efficient numerical design tool is needed to reduce the cost associated with a typical experimental antenna design cycle. Recently, a theoretical analysis was performed for the special case of a slot-coupled to a hemispherical dielectric resonator antenna [31-33]. This technique is restricted to hemispherical structures since it is based on the dyadic Green's function for a dielectric sphere.

In this chapter, the formulation presented in Chapter 2 for the coupling of a thin wire to a DBOR is modified to include the case of coupling of a thin slot aperture in a conducting ground plane to a DBOR. From a theoretical point of view, this is an attractive configuration since electromagnetic coupling through an aperture results in a division of the original problem into two half space problems upon application of image theory. Since the sources and matter in each

41

half space interact only with the slot, practical feed mechanisms may be accurately modelled in the half space below the ground plane without introducing additional complications to the DBOR/slot problem.

4.1 Formulation of the Boundary Value Problem

Consider a DBOR positioned directly over a slot in a conducting ground plane as illustrated in Fig. 4.1a. The slot is denoted by S_s. $\underline{E}^s$ is the unknown electric field in the thin slot. Fig. 4.1b illustrates the equivalent problem valid in the half space $z < 0$. This problem has been obtained in the following way [34]. After shorting the slot, the conducting ground plane was made continuous, and the electric field, $\underline{E}^s$, was restored to its original value at $z = 0^-$ by placing an equivalent surface magnetic current, $\underline{M}_s^- = u_z \times \underline{E}^s$, where u_z is a z-directed unit vector, just below the surface, S_s, (as suggested by the "-" superscript) in the short-circuited ground plane. Upon application of image theory, the ground plane is removed and replaced by an equivalent surface magnetic current $2\underline{M}_s^-$ on S_s.

The equivalent problem valid for the half space $z > 0$ is obtained in a similar manner. Again, after having shorted the slot in the ground plane, the electric field, $\underline{E}^s$, was restored to its original value by placing an equivalent surface magnetic current, $\underline{M}_s^+ = -u_z \times \underline{E}^s$, just above the surface, S_s, (as suggested by the "+" superscript) on the short-circuited ground plane. Image theory then yields the equivalent problem valid in the half space $z > 0$ as illustrated in Fig. 4.1c. This equivalent problem is further divided into an interior and exterior problem as a direct consequence of the equivalence principle. The interior problem may be obtained from Fig. 1b by substituting $\underline{J}_{wd}$ with $2\underline{M}_s$ and S_{wd} with S_s. The exterior problem may be obtained from Fig. 1c by eliminating $\underline{J}_{ws}$ and S_{ws}. Note that continuity of the electric field through the slot has been automatically satisfied by the fact that $\underline{M}_s^+ = -\underline{M}_s^-$ on opposite sides of the slot.

After enforcing continuity of the tangential component of both the electric and magnetic fields

42

on the surface of DBOR, and continuity of the magnetic field through the slot, the following system of integro-differential equations, from which the unknowns $\underline{J}_{de}$, $\underline{M}_{de}$, and $\underline{M}_s$ can be determined. These equations may be written in operator form as follows.

$$\underline{H}^d_{tan}(\underline{J}_{de}, \underline{M}_{de} - 2\underline{M}_s^-) - \underline{H}^e_{tan}(2\underline{M}_s^-) = \underline{H}^{i-}_{tan} \quad \text{on} \quad S_s \tag{4.1}$$

$$\underline{E}^d_{tan}(\underline{J}_{de}, \underline{M}_{de} - 2\underline{M}_s^-) + \underline{E}^e_{tan}(\underline{J}_{de}, \underline{M}_{de}) = \underline{0} \quad \text{on} \quad S_{de} \tag{4.2}$$

$$\underline{H}^d_{tan}(\underline{J}_{de}, \underline{M}_{de} - 2\underline{M}_s^-) + \underline{H}^e_{tan}(\underline{J}_{de}, \underline{M}_{de}) = \underline{0} \quad \text{on} \quad S_{de} \tag{4.3}$$

The above system of equations consists of the MFIE enforced on the slot, and the PMCHW formulation the surface of the DBOR [21]. Note that since the slot aperture is illuminated by an impressed source in the half space $z < 0$, the right hand side of equations (4.2) and (4.3) has been set equal to 0. $\underline{H}^i$ is the magnetic field due to the impressed sources and their images in the region $z < 0$.

4.2 Solution Techniques

The system of surface integral equations (4.1-4.3) are solved using the same Galerkin MoM procedure as described in Chapter 2. The basis functions used on the BOR were discussed in Chapter 2. Since the slot aperture is very narrow, the only component of current on S_s is that which is axially directed. Therefore, $\underline{M}_s$ is expanded as the following series functions.

$$\underline{M} = \sum_p d_p \frac{\Lambda_p(s)}{w} u_p \quad p=1,2, ..., p_s \quad \text{on} \quad S_s \tag{4.4}$$

where d_p is the current expansion coefficient associated with each rooftop basis function $\Lambda_p(w)$ [35], p_s is the total number of basis functions, and w is the width of the slot.

After applying the Galerkin MoM procedure to the system of equations (4.1-4.3), they may be expressed in matrix form as

43

$$
\begin{bmatrix}
[BB]_{-n} & . & \cdots & . & \cdots & . & . & [BS_s]_{-n} \\
. & [BB]_{-n+1} & \cdots & . & \cdots & . & 0 & [BS_s]_{-n+1} \\
. & . & \cdots & \cdots & \cdots & \cdots & \cdots & \cdots \\
. & . & \cdots & [BB]_0 & \cdots & . & . & [BS_s]_0 \\
. & 0 & \cdots & . & \cdots & \cdots & . & \cdots \\
. & . & \cdots & . & \cdots & [BB]_{n-1} & . & [BS_s]_{n-1} \\
. & . & \cdots & \cdots & . & . & [BB]_n & [BS_s]_n \\
[S_sB]_{-n} & [S_sB]_{-n+1} & \cdots & [S_sB]_0 & \cdots & [S_sB]_{n-1} & [S_sB]_n & [S_sS_s]
\end{bmatrix}
\cdot
$$

$$
\begin{bmatrix}
|JM>_{-n} \\
|JM>_{-n+1} \\
\cdots \\
|JM>_0 \\
\cdots \\
|JM>_{n-1} \\
|JM>_n \\
|M_s>
\end{bmatrix}
=
\begin{bmatrix}
0 \\
0 \\
\cdots \\
0 \\
\cdots \\
0 \\
0 \\
|I_s>
\end{bmatrix}
\qquad (4.5)
$$

The vectors $|JM>_n$ represent the electric and magnetic current coefficients for the nth Fourier mode of the basis functions which reside on S_{da} and are given by

$$
\begin{bmatrix}
|M_{da}> \\
|J_{da}>
\end{bmatrix}_n
\qquad (4.6)
$$

The vector $|M_s>$ represents the current expansion coefficients for the magnetic currents which reside on the surface S_s. $|I_s>$ represents the known (incident magnetic field) slot aperture excitation current in the half space $z < 0$.

44

The matrix $[BB]_n$ is further partitioned as

$$
\begin{bmatrix}
([Z^e_{de,de}] + \dfrac{1}{\eta_r}[Z^d_{de,de}]) & ([Y^e_{de,de}] + [Y^d_{de,de}]) \\[3mm]
([Y^e_{de,de}] + [Y^d_{de,de}]) & (-[Z^e_{de,de}] - \eta_r[Z^d_{de,de}])
\end{bmatrix}_n
\tag{4.7}
$$

where $\eta_r^2 = \mu_q/\epsilon_q$, (q=d or e) and a typical [Z] or [Y] matrix is of the form

$$
\begin{bmatrix}
[B_{zz}] & [B_{z\phi}] \\[2mm]
[B_{\phi z}] & [B_{\phi\phi}]
\end{bmatrix}_n
=
\begin{bmatrix}
[B_{zz}] & -[B_{z\phi}] \\[2mm]
-[B_{\phi z}] & [B_{\phi\phi}]
\end{bmatrix}_{-n}
\tag{4.8}
$$

where [B] = [Z] or [Y], a square matrix of order N_t for each Fourier mode n. These matrix elements may be obtained by applying duality to the corresponding integral representations given in [22]. The matrix $[BS_s]_n$ is given by

$$
\begin{bmatrix}
\dfrac{1}{\eta_r}[Z^d_{de,s}] \\[3mm]
[Y^d_{de,s}]
\end{bmatrix}_n
\tag{4.9}
$$

and the matrix $[S_sB]_n$ is given by

$$
\begin{bmatrix}
\dfrac{1}{\eta_r}[Z^d_{s,de}] & [Y^d_{s,de}]
\end{bmatrix}_n
\tag{4.10}
$$

The matrices $[BS_s]_n$ and $[S_sB]_n$ can be further partitioned as

45

$$[BS_s]_n = \begin{bmatrix} \frac{1}{\eta_r}[Z^d_{t,s}] \\[6pt] \frac{1}{\eta_r}[Z^d_{\phi,s}] \\[6pt] [Y^d_{t,s}] \\[6pt] [Y^d_{\phi,s}] \end{bmatrix}_n \quad \text{and} \quad [S_sB]_n = \begin{bmatrix} \frac{1}{\eta_r}[Z^d_{s,t}] & \frac{1}{\eta_r}[Z^d_{s,\phi}] & [Y^d_{s,t}] & [Y^d_{s,\phi}] \end{bmatrix}_n \qquad (4.11)$$

The matrix $[BS_s]_n$ is of order $(4N_t \times p_s)$ and $[S_sB]_n$ is of order $(p_s \times 4N_t)$. Integral expressions for the matrix elements of the coupling block $[BS_s]_n$ are given in Appendix B. The matrix $[S_s,S_s]$ is a Z matrix for $<w,\underline{H}(2\underline{M}_s)>$. The integral expression for this matrix may be found in [34].

Given that the slot is excited by a delta current source, and that the final goal is the computation of the slot input impedance, the following steps, as performed in Chapter 2, can be performed to obtain the solution for the magnetic current coefficients, $\underline{M}_s$.

$$|JM>_n = -[BB]_n^{-1} \bullet [BS_s]_{-n} \bullet |M_s>, \quad n = -N,...,N \qquad (4.12)$$

These results can be substituted into the last equation system (last row) of (4.5) to obtain the following matrix equation.

$$\begin{aligned} \Big[[S_sB]_{-n} \{BB]_{-n}^{-1} \{BS_s]_{-n} + ... + [S_sB]_0 \{BB]_0^{-1} \{BS_s]_0 + ... \\ + [S_sB]_n \{BB]_n^{-1} \{BS_s]_n - [S_s S_s] \Big] \bullet \\ |M_s> = -|I_s> \end{aligned} \qquad (4.13)$$

The current coefficients, $\underline{M}_s$, may now be easily obtained by inverting the bracketed term (an admittance matrix) and multiplying the result by $|I_s>$.

4.3 The Slot-Coupled Microstrip Line Feed

As mentioned in the beginning of this Chapter, since the sources and matter in each half space

46

interact only with the slot, practical feed mechanisms may be modelled in the half space below the ground plane without introducing additional complications to the DBOR/slot problem. One such feed mechanism is the slot coupled microstrip line.

Fig. 4.2a illustrates the geometry of the DBOR/slot boundary value problem in which the DBOR resides directly over a slot in a conducting ground plane, at $z=0$, which is separated from a microstrip transmission line by a substrate of thickness d. Since the geometry of Fig. 4.2a in the half space $z>0$ is identical to that of Fig. 4.1a, the equivalent problem for the geometry of Fig. 4.2a valid for $z>0$ is identical to that in Fig. 4.1c. Because of this, the problem description shall not be repeated for this case.

The half space $z<0$ consists of a thin dielectric substrate and an infinitesimally thin conducting transmission line at $z=-d$. The micro-strip line, as illustrated in Fig. 4.2b, is assumed to be both x-directed and infinitely long, and propagating a quasi-transverse electromagnetic (TEM) mode. The slot aperture has been replaced by the y-directed surface equivalent magnetic current, $\underline{M}_s$, as illustrated in Fig. 4.2b. For the sake of clarity, the aperture surface, S_s has not been shown in this figure. The transmission line is analyzed using the same method as that documented in [36]. This method is a combination of reciprocity, and moment method analyses, using the exact Green's functions for the planar structure. This method treats the slot aperture as a transmission line discontinuity. It is an efficient and accurate method for computing the input impedance of a thin slot aperture in the conducting ground plane of a planar structure whose substrate thickness is such that only the TM_0 mode surface wave propagates. Only the results of the analysis shall be given in this work since the details can be found in [36].

The magnetic current coefficients, d_p, can be found from the following matrix equation,

47

$$|M> = \{[Y^{z<0}] + \frac{1}{\eta_0}[Y^{z>0}] + \frac{1}{2}|\Delta v> <\Delta v|\}^{-1} \; |\Delta v> \qquad (4.14)$$

$[Y^{z>0}]$ is the $p_s \times p_s$ matrix given by the bracketed term in equation (4.13), and $<\Delta v|$ is the transpose of $|\Delta v>$. Using the results listed in Appendix D, the elements of $[Y^{z<0}]$, a $p_s \times p_s$ admittance matrix defined for the thin slot aperture, may be expressed in spectral form as

$$Y_{mn}^{z<0} = \frac{1}{4\pi^2} \int\limits_{-\infty}^{+\infty}\!\!\!\int F_u^2(k_x)\tilde{G}_{yy}^{HM}(k_x,k_y)F_p^2(k_y)$$
$$\bullet \cos[k_y(y_m-y_n)]dk_x dk_y. \qquad (4.15)$$

where $F_{u,p}$ is the Fourier transform of the basis and testing functions. Again using the results listed in Appendix D, the voltage discontinuity vector, $|\Delta v>$, may be written in spectral form as

$$\Delta v_m = \frac{1}{2\pi Z_c^{1/2}} \int\limits_{-\infty}^{+\infty} F_u(k_y)\tilde{G}_{yx}^{HJ}(k_x=-\beta_f,k_y)F_p(k_y)\bullet\cos(k_y y_m)dk_y \qquad (4.16)$$

where β_f is the effective propagation constant of the line. An offset feed line may be modelled by replacing y_m with y_m-y_s as shown in Fig. 4.3a.

The effective propagation constant is computed by considering an infinte, x-directed microstrip line, of width W_f, supporting a travelling wave current of the form $exp(-j\beta_f x_0)$. Using the results listed in Appendix D, the expression for the x-component of the electric field is then evaluated as [37]

$$E_{xx} = -2\pi \int\limits_{-\infty}^{+\infty}\!\!\!\int \delta(k_x+\beta_f)F_y(k_y)\tilde{G}_{xx}^{EJ}(k_x,k_y)e^{jk_x x}e^{jk_y y}dk_x dk_y \qquad (4.17)$$

where F_y is the Fourier transform of the y-variation of the x- directed electric current distribution (assumed to uniform since the strip is very thin), and is given by $F_y(k_y)=2\sin(k_y W/2)/k_y$.

Enforcement of the electric field boundary condition at the surface of the conducting transmission line (after performing the k_x integration) yields the following characteristic equation for β_f, which can be solved quickly by using Muller's method.

$$\int_{-\infty}^{+\infty} \tilde{G}_{xx}^{EJ}(\beta_f, k_y) F_y^2(k_y) = 0 . \qquad (4.18)$$

The voltage reflection coefficient, R, may be computed from the magnetic current (voltage) and the voltage discontinuity vector as $R = 0.5 \, | M >^t \, | \Delta v >$ [36]. The slot impedance may be computed from the expression

$$Z_s = Z_c \frac{2R}{1-R}. \qquad (4.19)$$

where Z_c is the characteristic impedance of the transmission line. In many applications, the transmission line is open circuit terminated by a stub of length $\lambda_g/4$, where λ_g is the guide wavelength at the center frequency of operation. To compute the impedance of the slot under this condition, one simply adds to the input impedance, computed under the infinite line assumption, a series impedance, $Z_{st} = -jZ_c \tan(\beta_f L_t)$, where L_t is the open circuit stub length measured from the center of the slot, as shown in Fig. 4.3b.

4.4 Numerical Results

As discussed in Chapter 3, in order to verify a theoretical model experimentally, it is necessary to have a test device which represents the ideal situation as closely as possible. In the case of the coaxial probe fed DRA, it has been shown that the presence of thin air gaps between the dielectric resonator, and the conducting surfaces on which it resides, can have a significant effect upon the antenna resonant frequency and input impedance. It is believed that the presence of small air gaps between the dielectric resonator, and the conducting ground plane on which it resides, will have a similar effect upon the input impedance of the slot coupled DRA. Because

49

of this possibility, the slot-coupled transmission line model of [36] was incorporated in the computer code which implements the dyadic Green's function for a hemisphere [32]. This code was then used to verify the application of the theory presented in this chapter. It should be pointed out that the only difference between the transmission line model used with the present theory, and that incorporated in [32], are the basis functions. Piecewise linear basis functions are used in the former; whereas, piecewise sinusoidal basis functions are used in the latter.

The radius of the HDRA under study was chosen to be 3.09cm. With this radius, the HDRA under study would have the same volume as that of the CDRA whose input impedances are plotted in Fig. 3.3. Since the h/a ratio of the CDRA of Fig. 3.3 was approximately 1, the TE_{111} mode of this HDRA should be excited close to the resonant frequency of the HEM_{11} mode for the CDRA under coaxial probe excitation. Plotted in Fig. 4.4, are the computed input impedances, as a function of frequency, of a slot-coupled HDRA under delta source excitation. As can be seen in Fig. 4.4, the input impedances of both theories are in very good agreement. Five basis functions were used on slot in both cases. Fig. 4.5 plots the input impedance of the same HDRA as a function of frequency with the transmission line model. Five basis functions were used on the slot for the dyadic Green's function analysis. Nine basis functions were used on the slot for the present theory. This indicates that the piecewise linear basis functions do not yield a solution which converges as rapidly as the piecewise sinusoidal basis functions when the transmission line model is implemented. Fig. 4.6 illustrates the effect that a displacement of $x_{s0} = 1$cm has upon the antenna input impedance and resonant frequency. Seven basis functions were used on the slot for both techniques. The Fourier modes -3 to +3 were used in the BOR/slot analysis. The behavior is consistent with that of the CDRA analyzed in Chapter 3. Since the y magnetic field component of the dominant TE_{111} mode is strongest at $x = 0$, the slot should be positioned at $x_{s0} = 0.0$ for efficient mode coupling. Based upon the coaxial probe feed

studies of Chapter 3, a slot displacement away from $x_o = 0.0$, should raise the resonant frequency as well as couple to higher order modes. The effect of the higher order mode coupling upon the input impedance is that of increasing inductance. These effects can be seen in Fig. 4.3.

Since one of the objectives of this work is to build a computer code that can be used for design of DRAs, it is necessary to have a code which runs very fast. Therefore, it would be desirable to use a delta source model to simulate the effect of the slot-coupled transmission line. As can be seen from Fig. 4.7, using an average effective permittivity, $\epsilon_{eff} = (\epsilon_r + 1)/2$, together with a delta source, yields impedance levels and a resonant frequency close to that of the transmission line model. Fig. 4.8, which shows the effect an off center transmission line feed, also indicates that the delta source model, together with $\epsilon_{eff} = (\epsilon_r + 1)/2$, is a good first approximation for obtaining preliminary design data. Therefore, for initial design work, the delta source model should prove to be effective.

4.5 Experimental results

The input impedance of slot-fed dielectric radiators has been measured by two different feed arrangements: a microstrip-slot excitation and a coaxial-slot excitation. The two measurements are based on different data processing procedures, and they complement each other. Furthermore, the measurements were performed on radiators made of various relative dielectric constants (between $\epsilon_r = 12$ and $\epsilon_r = 80$), providing a consistency check over a wide range of input parameters.

The physical layout of the microstrip-slot measurement is shown in Fig. 4.9a. The microstrip conductor is located below the ground plane, and it is connected to coaxial connectors of type N

which are used for the attachment of the Hewlett Packard Model 8510B network analyzer. The ground plane of the microstrip line has a rectangular aperture which provides the excitation for the HEM_{11} mode in the dielectric radiator which is placed on top of the aperture.

The characteristic impedance of the microstrip is 50 Ω. The substrate is Rogers RT/duroid 5880, which has relative dielectric constant $\epsilon_r = 2.20$, loss tangent 0.0004, slab thickness 0.062", and copper thickness 1 oz/sq. ft. (corresponding to 35 μm). The ground plane was originally of the size 76 $\times$ 133 mm (3" $\times$ 5.25"); this was later increased to 229 $\times$ 203 (9" $\times$ 8"). Absorbing material was placed around the radiating structure to prevent multiple reflections from the surrounding objects in the laboratory.

The coaxial-slot measuring arrangement is shown in Fig. 4.9b. In this arrangement, the outer conductor of the semirigid coaxial line UT-85, of characteristic impedance 50 Ω, is soldered to one side of the slot. The center conductor of the coaxial line is soldered to the other side of the slot. The coaxial line is equipped with an SMA coaxial connector, which is used for the attachment to the network analyzer. The ground plane is of the size 1' $\times$ 1', and is made of the brass metal sheet of thickness 0.021". The dielectric radiator is made of the Emerson Cumming type Hi-K powdered dielectric material, with the dielectric constant $\varepsilon_r = 12$. The container for the powder is made of a vinyl tube of inner diameter 55 mm, with the wall thickness 3 mm, and of relative dielectric constant $\varepsilon_r = 1.8$. The absorbing material is placed around the entire structure.

4. 5. 1 Microstrip-slot measurements

When the scattering matrix is measured with the network analyzer, the measured object constitutes a two-port, delineated by the space between the two coaxial connectors shown in

52

Fig. 4. 9a. The antenna slot is placed symmetrically at the center of the structure. The slot impedance has to be de-embedded from the measured scattering parameters. A de-embedding procedure well suited for this situation is the so-called TRL (through-reflect-line) method [44]. This technique was originally introduced for six-port measurements, but it can be easily adapted to the conventional two-port measurements [45].

For this measurement, a narrow rectangular slot of the size 23 × 2 mm was used. The dielectric resonator used was Trans-Tech D86230905Z407A, of diameter 22.99 mm and height 10.34 mm, with the relative dielectric constant of 80.0. The de-embedded slot impedance is shown in Fig. 4.10a. One observes that the antenna behaves as a resonant circuit. The resonant frequency is 1.15 GHz, and the maximum of the impedance is about 600 Ω. The imaginary part of the impedance shows an odd symmetry about the resonant frequency, varying between +300 to about -300 Ω.

In the next experiment, the resonator was lifted from the ground plane by inserting a dielectric spacer of diameter 25.4 mm and height 0.79 mm (1/32"). The material of the spacer is Rexolite, with dielectric constant 2.5. The measured impedance is shown in Fig. 4.10b. It is observed that the resonant frequency has shifted toward a higher frequency, namely 1.75 GHz. The maximum resistance is now around 220 Ω, but the imaginary part of the impedance is no longer symmetric about the resonant frequency, varying between +135 Ω and -75 Ω.

The third measurement was made with twice as thick a spacer, namely 1.59 mm (1/16"), also made of Rexolite. The result is shown in Fig. 4.10c. It can be seen that the resonant frequency has moved even higher, to 1.93 GHz. The maximum resistive part of the impedance is now about 45 Ω, which is a convenient value for matching to a 50 Ω microstrip. However, the imaginary part of impedance is located between +70 and +28 Ω. Probably, a longer slot would cause the imaginary part of the impedance to behave symetrically.

53

The first conclusion that can be made from these experiments is, that the presence of the spacer between the dielectric resonator and the ground plane changes significantly the center frequency of the HEM_{11} mode. The second effect of the spacer is that the slot resistance can be lowered to a value close to 50 Ω. Unfortunately, these two effects could not be simulated numerically within the time allotted to the project.

4. 5. 2 Coaxial-slot measurements

The measurement circuit in Fig. 4. 9b is a one-port, in which the only de-embedding consists of transforming the impedance from the coaxial reference plane through the appropriate length of the UT-85 cable. Since a powdered dielectric material is used for this antenna, the slot aperture in the ground plane must be sealed in such a way that the measured terminal parameters are not influenced by the material used to close the aperture. First, the aperture was filled with GE Silicone Sealer and Adhesive which essentially formed a silicone (Si) window in the ground plane. The antenna's terminal impedance was measured as a function of frequency. Next, the terminal impedance was measured using two different samples of 0.002" thick transparent tape (Scotch tape) to cover the Si window from the top side of the ground plane (identified as TOT in Figs. 4.11 to 4.14). After removing the tape from the top of the aperture, the terminal impedance of this antenna was measured using a large sample of tape to cover the Si window from beneath the ground plane (identified as TOB in Figs. 4.11 and 4.14). As can be seen in Figs. 4.11 and 4.12, both resonant frequency and impedance levels are influenced by the presence of the tape between the bottom of the DR and the ground plane. Also obvious is that the presence of the tape on the bottom of the Si window has only a slight influence upon the antennas terminal parameters. From this experimental study, it was decided to measure the terminal

impedances without the Si window and with the tape on the bottom of the ground plane. The results of this measurement are presented in Figs. 4.13 and 4.14. All of the computed terminal impedances have been divided by two, so as not to dwarf the measured impedances.

Figures 4.13 and 4.14 show both computed and measured terminal impedances for the antennas under test. For these measurements, the Si window was not used. For the TOT measurements, the aperture was air filled, and for the TOB measurements, the aperture was filled with the powdered dielectric material. As can be seen from these figures, the small pieces of tape, which essentially just cover the antenna aperture, illustrate how sensitive the HEM_{11} mode could be to small air gaps between the ground plane and the bottom of the DR. It should be pointed out that the feed probe displaced from the center of the slot aperture by 1.64mm and that the numerical model takes this into consideration. Furthermore, since the terminal impedance was computed at the point where the center conductor of the feed line exited the coaxial line, and not in the plane of the aperture, Booker's extension to Babinet's principle [46] may not hold. Since the theory used in the numerical model does not account for the thickness of the ground plane, only modest agreement with measurements can be expected for antennas such as the one used in this experiment.
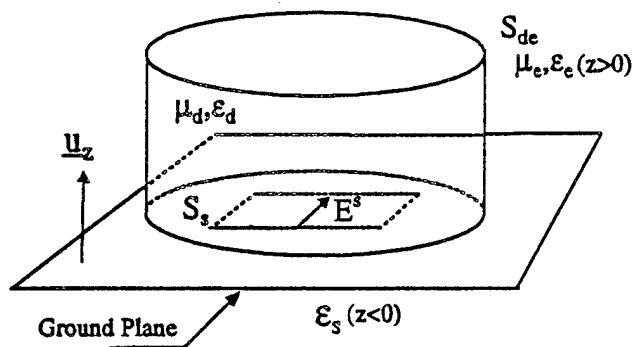
Fig. 4.1a. Geometry of the slot aperture coupled antenna.
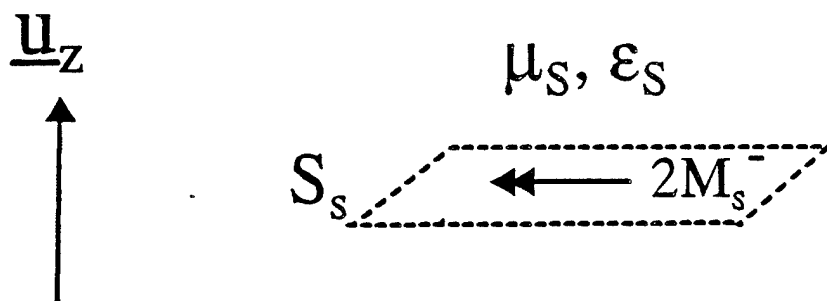
Fig. 4.1b. The imaged problem valid for $z < 0$.
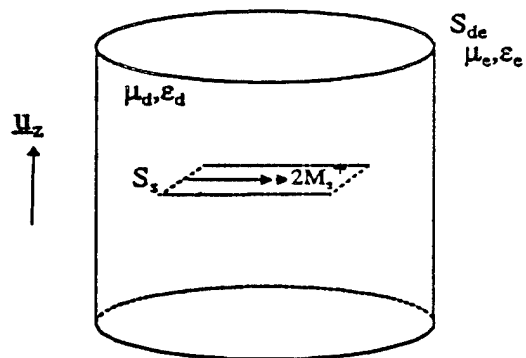
Fig. 4.1c. The imaged problem valid for $z > 0$.
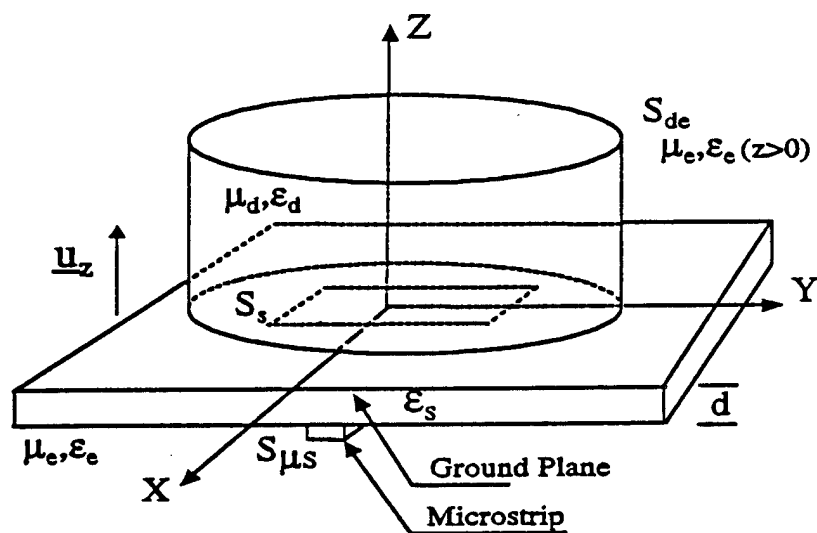
Fig. 4.2a. Geometry of the slot coupled microstrip DR antenna.
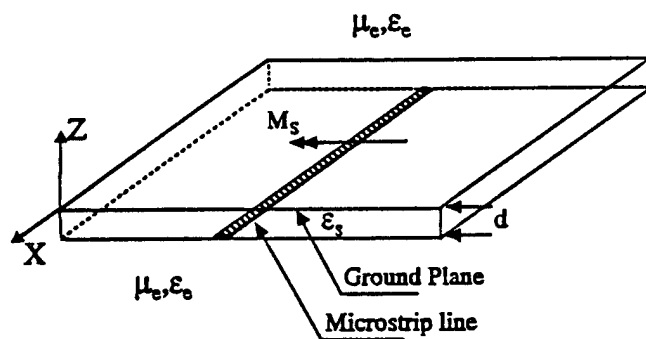
Fig. 4.2b. Problem valid for the half space $z < 0$.
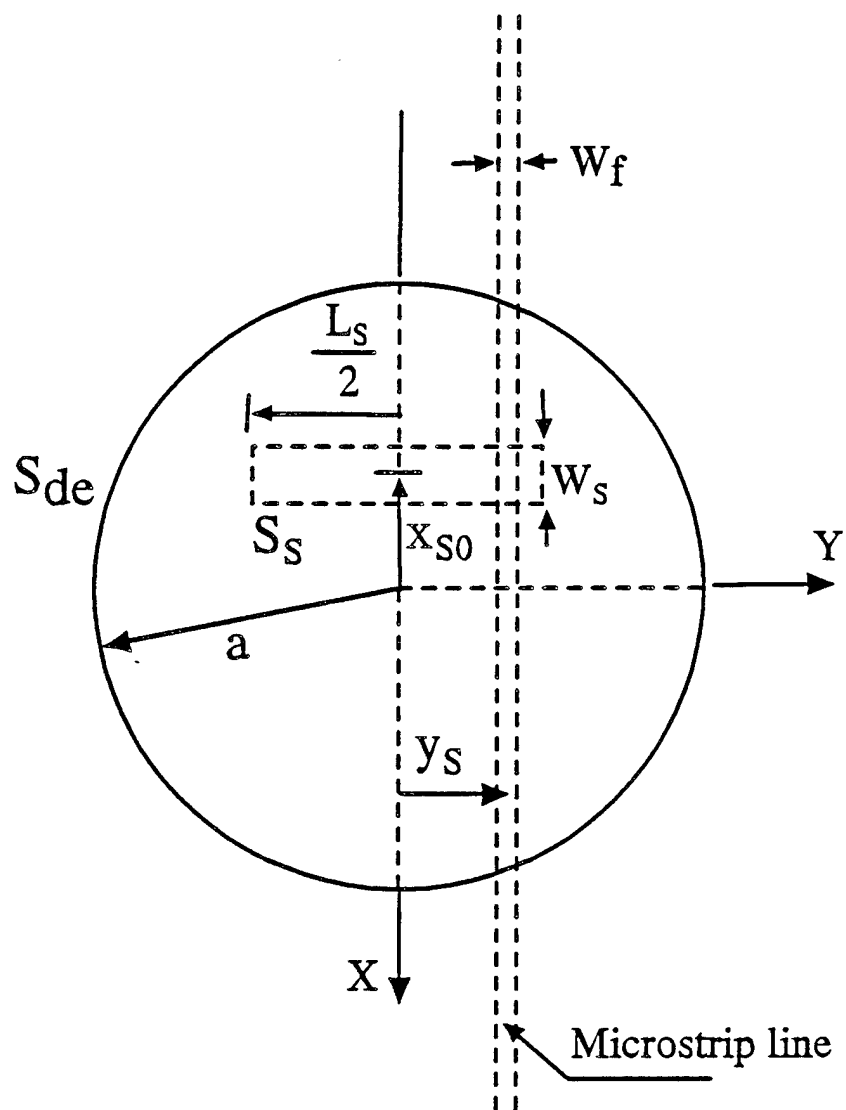
Fig. 4.3a. Coordinates for the slot-coupled transmission line.
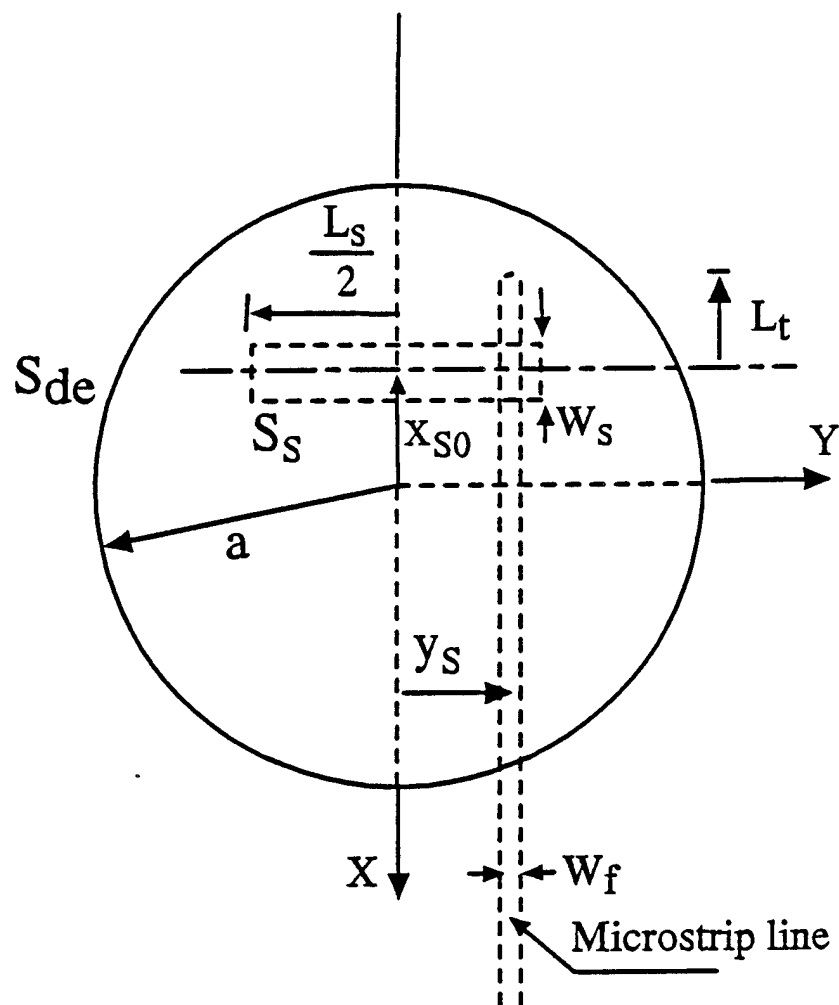
Fig. 4.3b. Coordinates for the slot-coupled transmission line with tuning stub of length L_t.
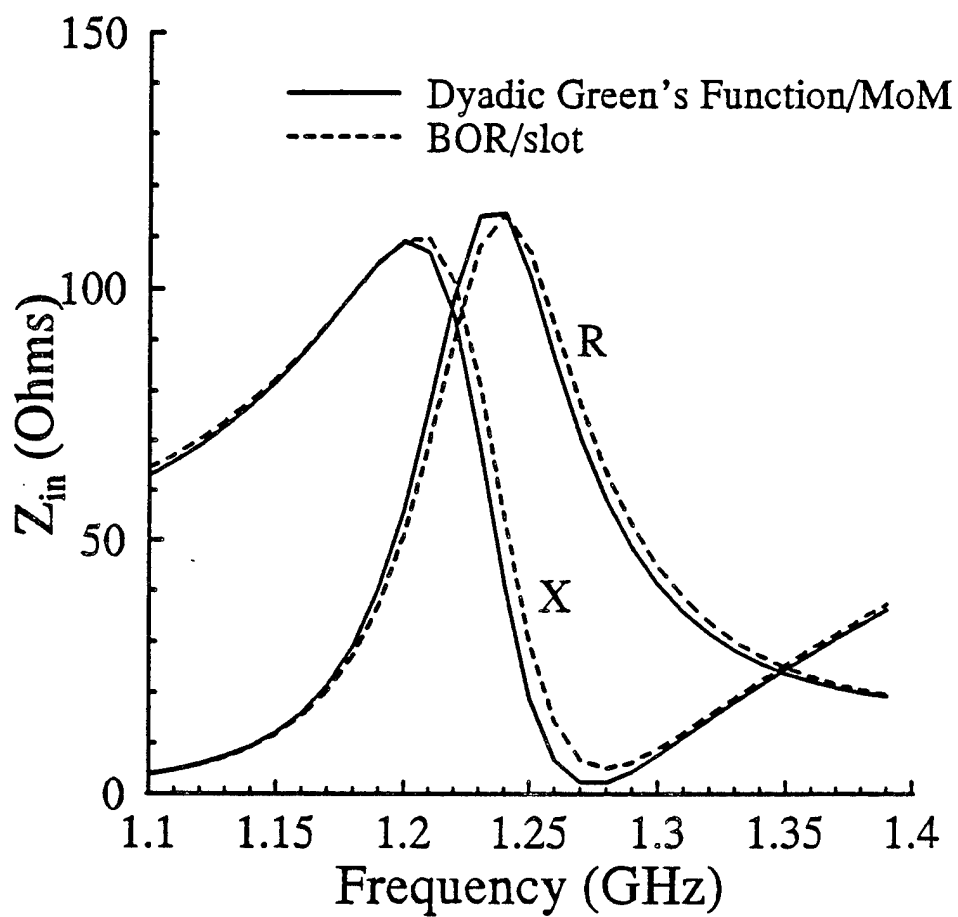
Fig. 4.4. Input impedance vs. frequency for a slot-coupled HDRA with delta-source model. $\epsilon_d = 12.0$, $\epsilon_s = 1.0$, $a = 3.09$cm, $y_s = x_{so} = 0.0$cm, $L_s = 3.5$cm, $W_s = 0.06$cm.

60
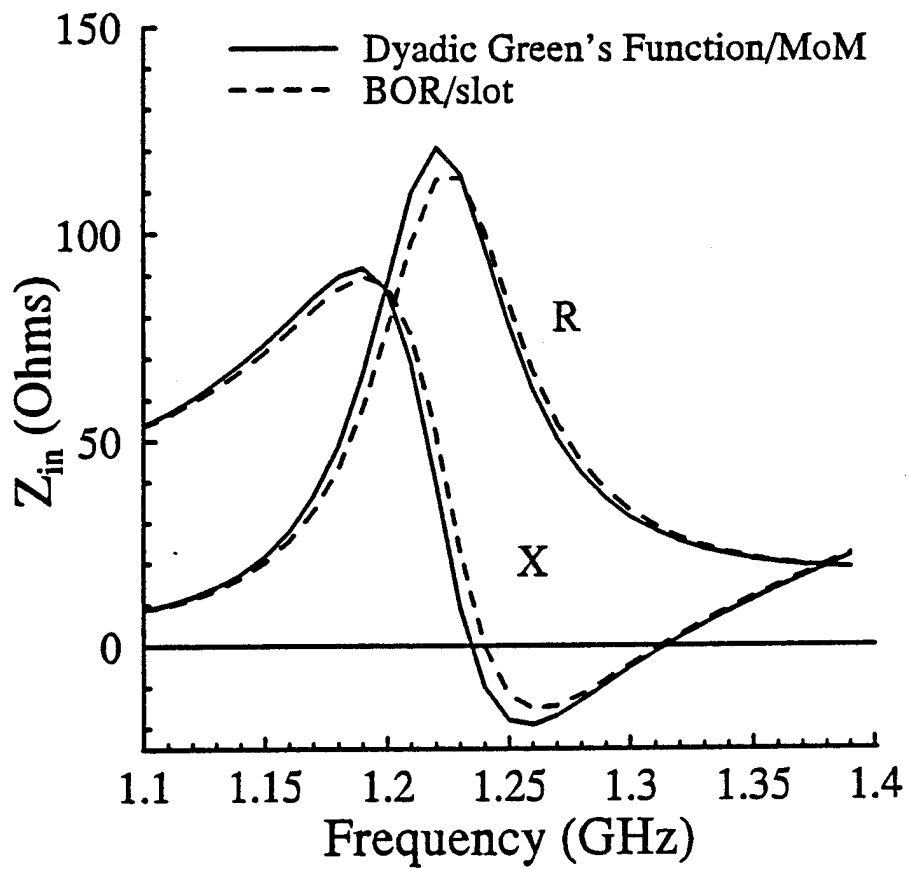
Fig. 4.5. Input impedance vs. frequency for a slot coupled\TL HDRA (no stub). $\epsilon_d = 12.0$, $\epsilon_s = 2.2$, $a = 3.09$cm, $y_s = x_{s0} = 0.0$cm, $L_s = 3.5$cm, $W_s = 0.06$cm, $W_f = .15$cm, $d = 0.16$cm.

61

Fig. 4.6. Input impedance vs. frequency for a slot-coupled/TL HDRA (no stub). $\epsilon_r = 12.0$, $\epsilon_s = 2.2$, a=3.09cm, $y_s = 0.0$cm, $x_{s0} = 1.0$cm, $L_s = 3.5$cm, $W_s = 0.06$cm, $W_f = .15$cm, d=.16cm.
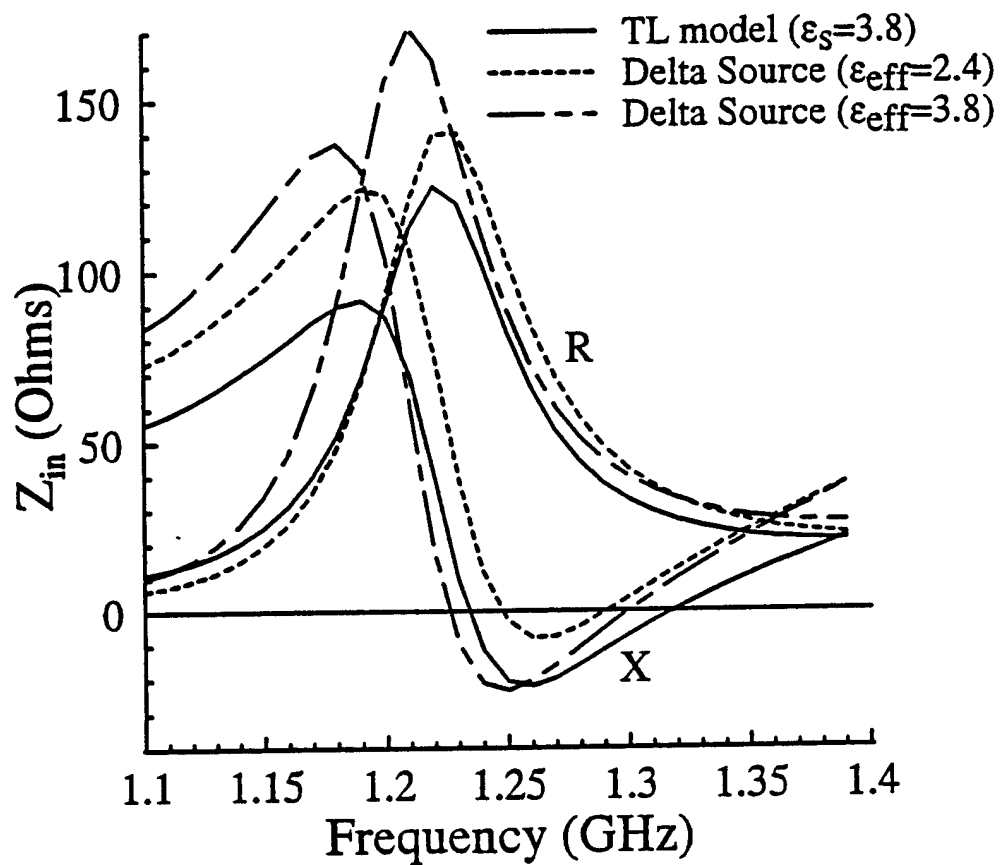
Fig. 4.7. Effect of ϵ_{eff} upon the input impedance when using delta source model. $\epsilon_d = 12.0$, a=3.09cm, $y_s = x_{s0} = 0.0$cm, $L_s = 3.5$cm, $W_s = .06$cm, $W_f = .15$cm, d=0.16cm.
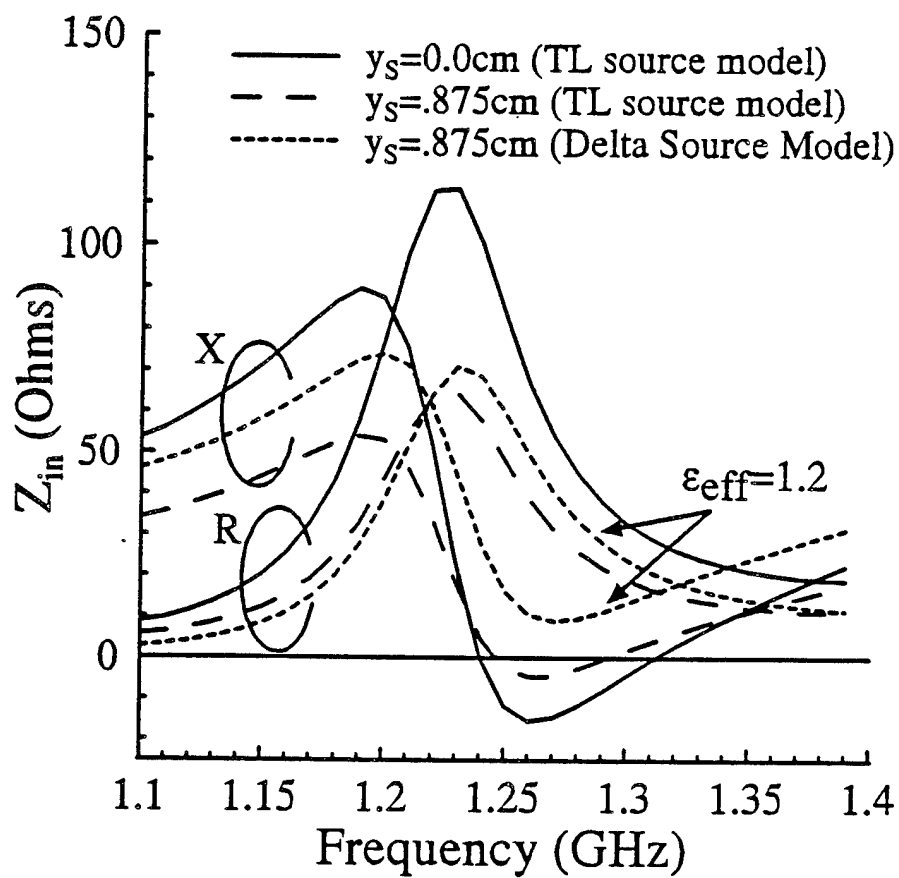
Fig. 4.8. Effect of source location upon the input impedance of HDRA. $\epsilon_r = 12.0$, $\epsilon_s = 2.2$, a=3.09cm, $x_{s0} = 0.0$cm, $L_s = 3.5$cm, $W_s = .06$cm, d=0.16cm.

64

Dielectric Resonator

An open slot
on the ground plane

Ground plane

Substrate
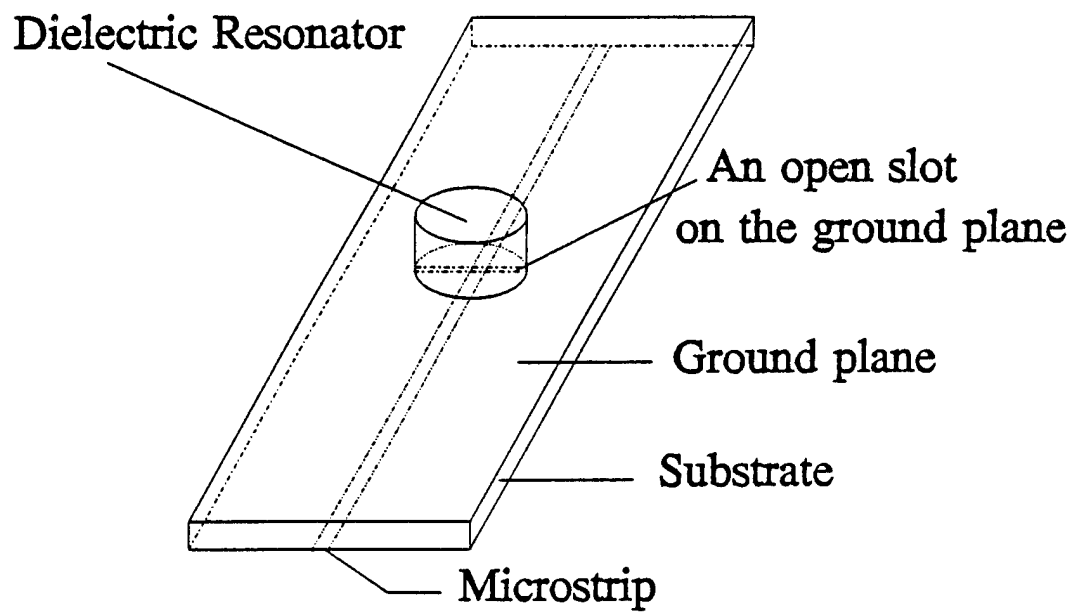
Microstrip

Fig. 4.9a Microstrip-slot measurement

65
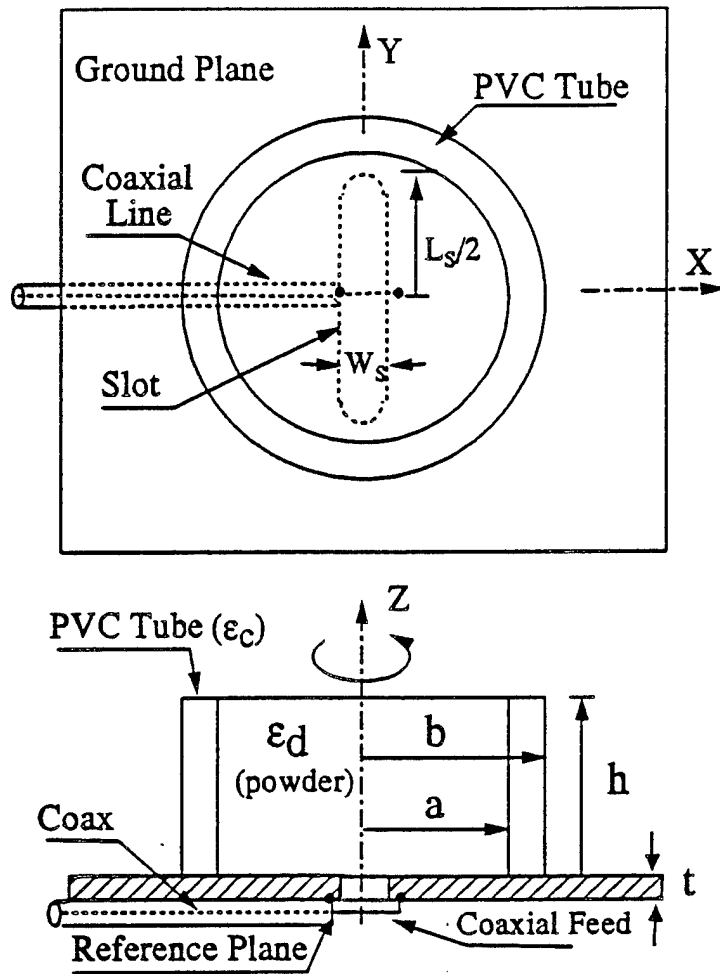
Fig. 4.9b Coaxial-slot measurement
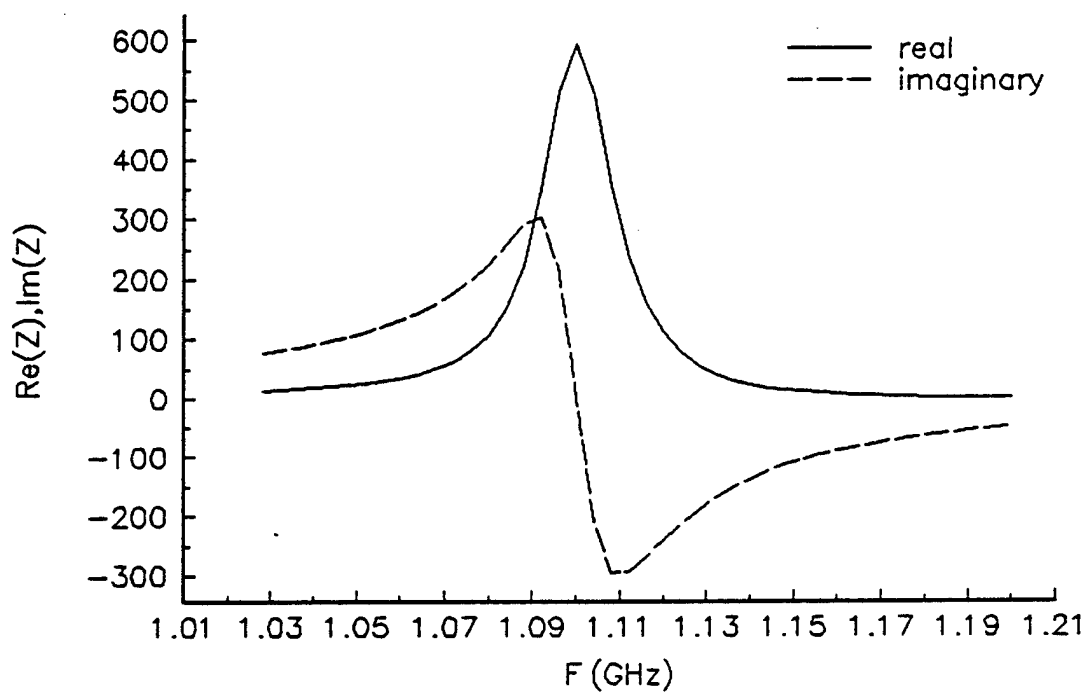
Fig. 4.10a Microstrip-slot impedance, without spacer

67
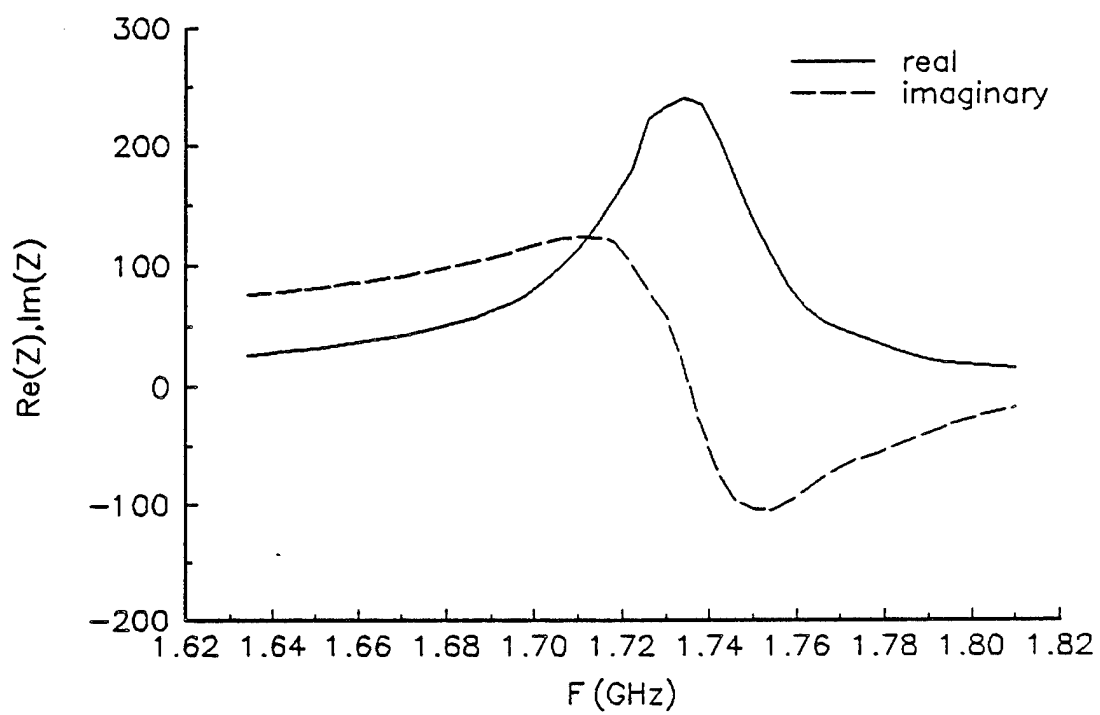
Fig. 4.10b Microstrip-slot impedance, spacer 0.79 mm

68
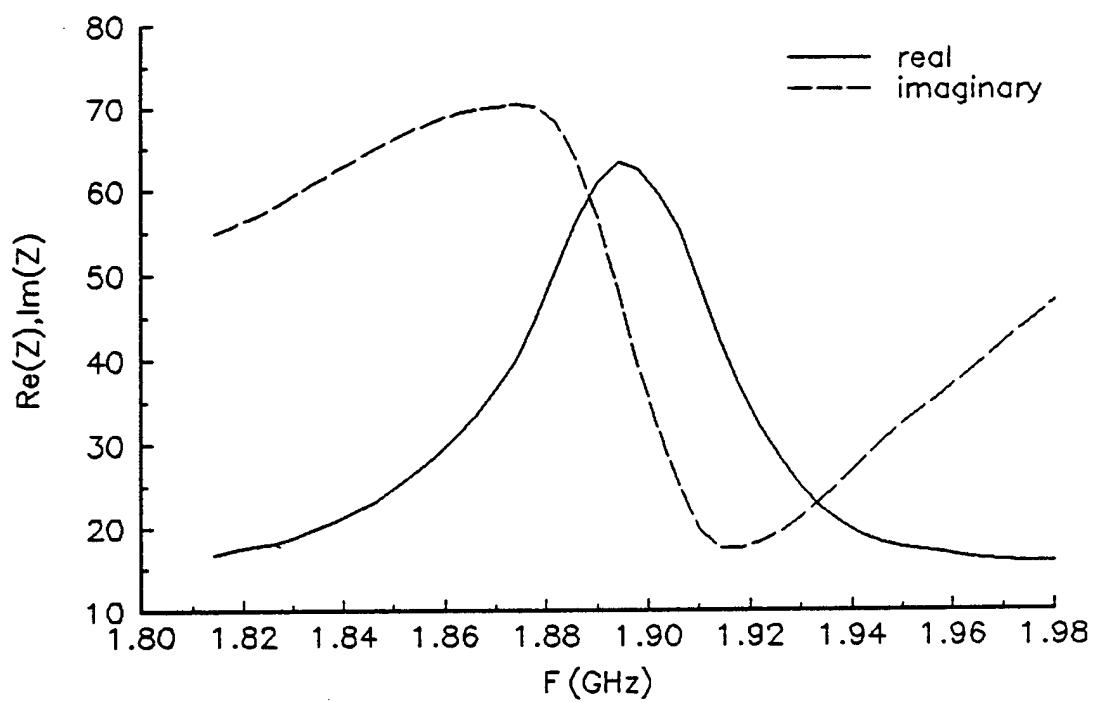
Fig. 4.10c Microstrip-slot impedance, spacer 1.59 mm

69
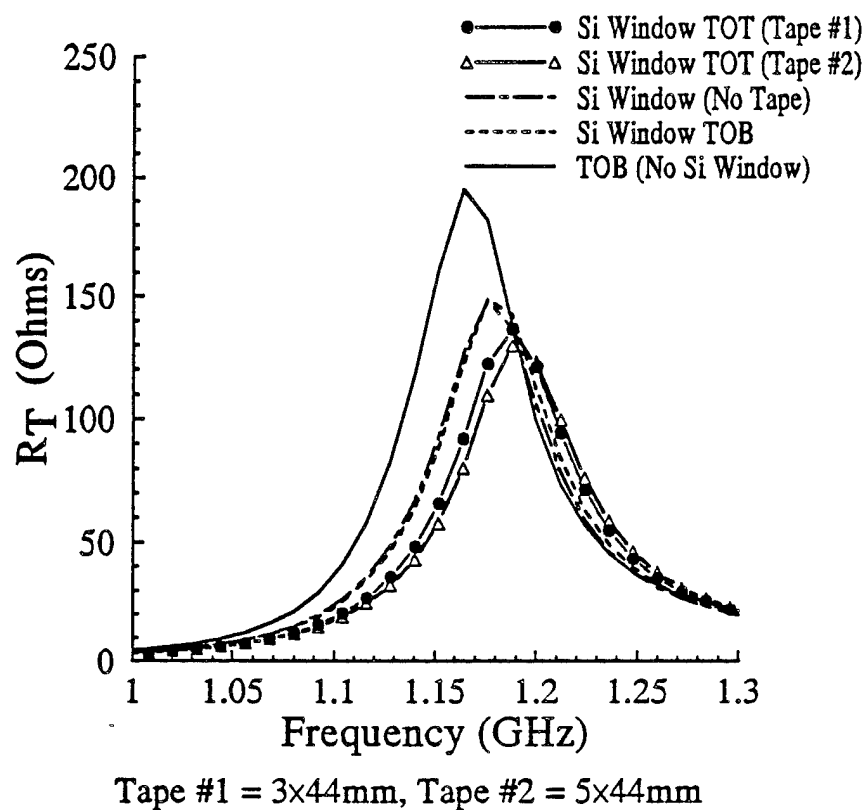
Fig. 4.11   Measured terminal resistances for the slot coupled antenna of
             Fig. 4.9b. a=27.5mm, b=30.3mm,
             h=26.0mm,t=0.031",L₂=42.0mm, W₄=1.588mm.

70
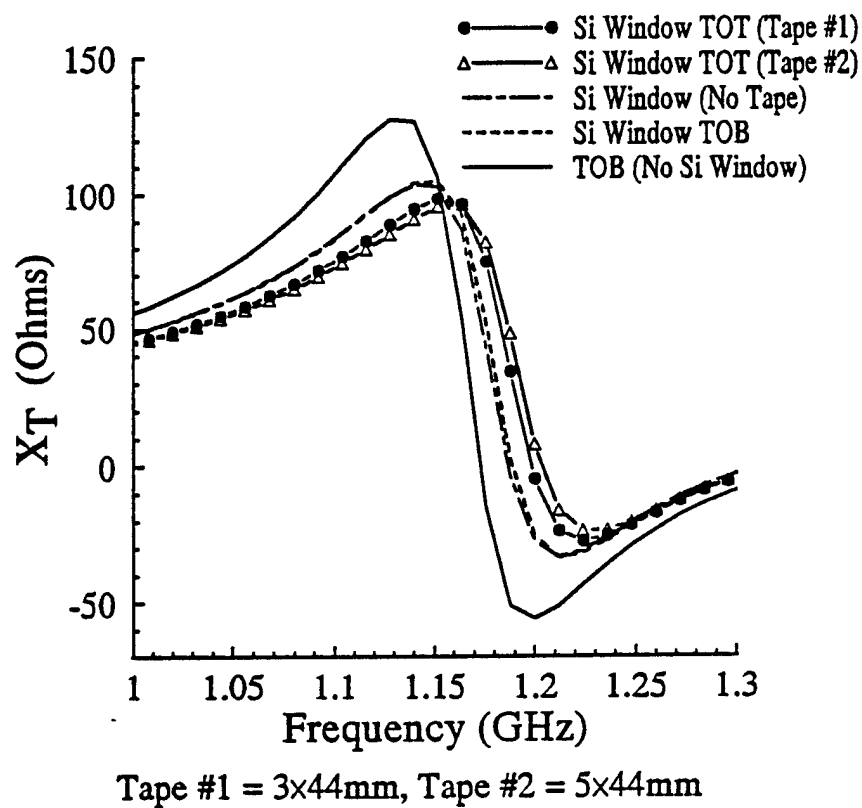
Fig. 4.12 Measured terminal reactances for the slot coupled antenna of Fig. 4.9b. a=27.5mm, b=30.3mm, h=26.0mm,t=0.031",L$_a$=42.0mm, W$_a$=1.588mm.
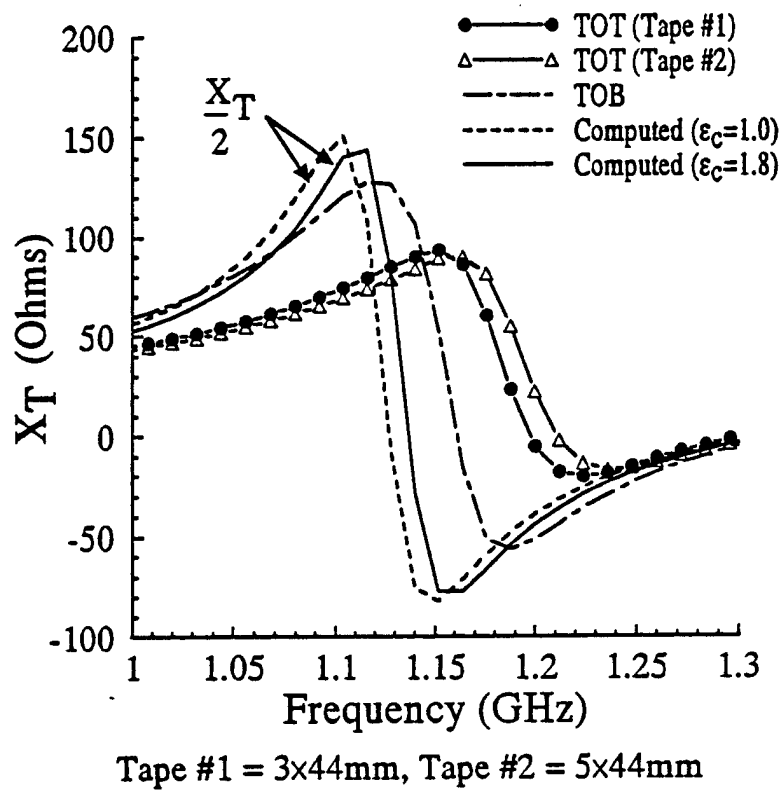
RT
2

Tape #1 = 3×44mm, Tape #2 = 5×44mm
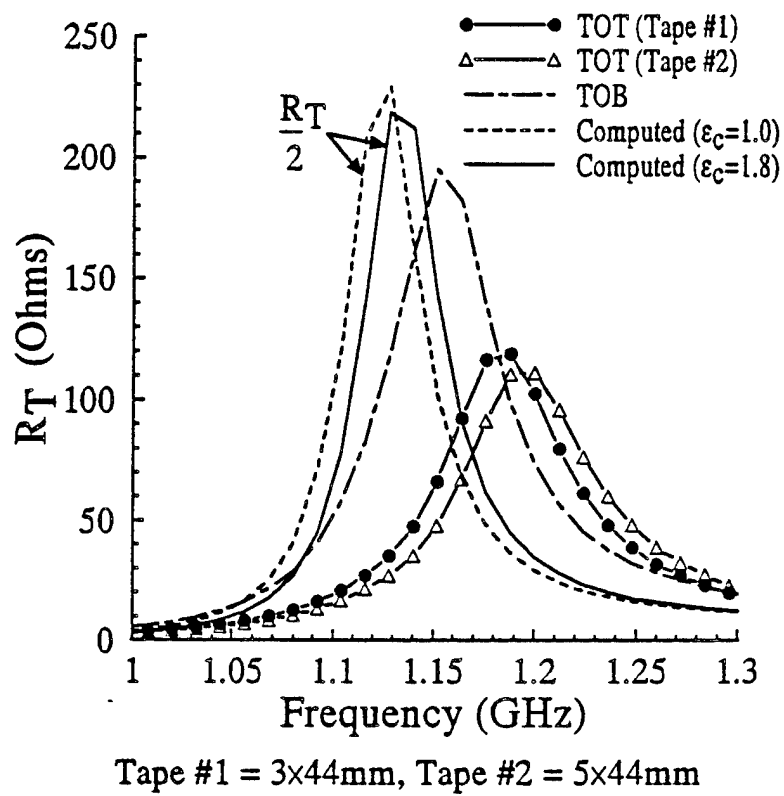
Fig. 4.13·   Measured and computed terminal resistances for the slot coupled antenna of Fig. 4.9b.
a=27.5mm, b=30.3mm, h=26.0mm,t=0.031",L_s=42.0mm, W_s=1.588mm.

Fig. 4.14   Measured and computed terminal reactances for the slot coupled antenna of Fig. 4.9b. a=27.5mm, b=30.3mm, h=26.0mm,t=0.031",L$_s$=42.0mm, W$_s$=1.588mm.

CHAPTER 5

Conclusions

In this work, a general formulation has been presented for the solution of the electromagnetic boundary value problem generated by a dielectric body of revolution in the presence of a thin wire antenna, or in the presence of a thin slot aperture in a conducting ground plane. Since an application of practical interest is the computation of the input impedance of a dielectric resonator antenna, the computer code written to implement this theory was optimized for this purpose. The integrity of this technique has been established both experimentally and numerically by modelling cylindrical dielectric resonator antennas excited by a coaxial feed probe. Under the present theory, the computed input impedances of a dielectric resonator antenna excited by a coaxial probe were verified numerically by comparing them to the input impedances computed by an independent numerical code which uses the exact Green's function for a dielectric sphere [23,32-33]. The present theory was also verified experimentally by fabricating a test antenna in such a way so as to insure that it would accurately represent the theoretical model. This test antenna consisted of a vertical PVC tube, fixed on a conducting ground plane, and filled with a powdered dielectric material. Not only did this test antenna serve the purpose of validating the present theory, it was also used to study the effect of a thin air gap between the dielectric material and the conducting surfaces on which it resides. Furthermore, the experimental and numerical air gap study revealed that it is possible to enhance the performance of a dielectric resonator antenna by separating it from the conducting surfaces on which it resides by a thin, low permittivity dielectric material. From an academic point of view, the results obtained from this experimental work are also of importance, because they provide data which may be used by future researchers as a reference source to aid in developing new theoretical models.

The validity of the present theory for the coupling of a thin slot aperture to a dielectric body

of revolution has also been established numerically. The numerical code used to analyze a hemispherical dielectric resonator antenna excited by a thin slot aperture [32] was modified to include a slot-coupled transmission line model. As shown in Chapter 4, the two theories yield results which are in very good agreement. However, the comparison of the computed and measured slot excited input impedances revealed significant discrepancies. The closer examination has demonstrated, that both the computed and the measured input impedances depend very critically on the thickness of intermediate dielectric layers in the vicinity of the slot. Such a layer can be formed by the air gap between the conductive plate and the solid dielectric resonator. To avoid the air gaps, a number of measurements were performed with the powdered dielectric. Nevertheless, even with the powdered dielectric, it was for instance observed that putting the adhesive tape below or on top of the slot made a considerable difference in the real part of the input impedance. At present, the agreement between the impedances obtained by the numerical model and by the measurement is not satisfactory for the slot excited antennas.

A variety of numerical and experimental checks have been performed in an effort to isolate the reason for the disagreement. Numerical results have been found to agree well with the results in the literature for a transmission-line-fed slot [36], a slot-fed hemispherical DRA [47], and an annular slot separating dissimilar half spaces [48]. On the other hand, our experimental data obtained for different structures, powdered and solid resonators, and for different de-embedding procedures all appear to be internally consistent, but disagree with numerical data. The data de-embedding procedure for microstrip-fed resonator has been checked by inserting a known lumped load at the aperture position, and the results were consistent. Thus, it is not clear at this time whether adding more details to the immediate vicinity of the slot model is required to improve the situation, or whether yet undetermined factors are distorting either the numerical or the experimental results.

75

APPENDIX A

A Novel Delta Gap Source Model For Cylindrical Dipoles

The delta gap source model, because of its simplicity and wide range of application, has been used extensively as a forcing function for the EFIE of thin wire antenna theory for many years. When used with the EFIE, the delta function is implicitly used to model an impressed electric field. Equivalently, the delta function can be thought of as driving the wire antenna with a 1V discontinuity in scalar potential or with an impressed unit voltage on the surface of the wire antenna. The discontinuity in scalar potential is a necessary boundary condition when obtaining Hallén's equation from Pocklington's EFIE [19]. The major drawback to the delta function is that is that is predicts infinite "gap" capacitance. Furthermore, since the delta function is not in the range of the Pocklington "operator," some questions arise concerning its use as a forcing function when the EFIE is solved via the method of moments (MoM) [38]. Despite this fact, it is well known that good results for the current distribution on thin wire antennas, with the possible exception of the current at the delta gap source location, can be obtained. Approximate current distributions are sufficient to compute the radiation patterns; however, to determine the input impedance of a wire antenna, the current at the source location must be accurately computed. Since the coaxial probe feeds for dielectric resonator antennas are modelled as cylindrical dipoles in this work, a delta source model which provides a stable, convergent solution for the current at the source location is needed.

Model Description: To analyze coaxial feed monopole antennas, image theory is invoked to remove the ground plane. The monopole is then modelled as a dipole in free space as shown in Fig. A1a. This same dipole model has been used to analyze the antenna of Fig A1b. In accordance with thin wire theory, the end caps of the wire are neglected and the wire in essence becomes a tube. In this work, the unknown current has been expanded in terms of a series of

subdomain basis functions, J_i, as

$$Ju_z = u_z \sum_1^N c_i J_i, \text{ where } J_i = \frac{T_i}{2\pi a_w}, \tag{A.1}$$

the c_i's are the unknown current coefficients, N is the total number of basis functions, T_i is the "triangle" function, and a_w is the dipole radius. Under a Galerkin MoM procedure, the testing function would be J_j, where $j = 1, 2, \ldots, N_g, \ldots, N\text{-}1, N$, as shown in Fig. A1a. Forming the inner product, $<J_j, \delta(z)>$, where $\delta(z)$ is the delta function, evaluates to a 1 in the generalized voltage matrix at the position corresponding to T_g [18]. The problem of poor convergence of the current at the delta gap source location can now be explained. Placing a 1 in the generalized voltage matrix satisfies the 1V discontinuity in scalar potential, but fails to satisfy the boundary condition on the impressed electric field, E^i. This failure stems from the fact that since E^i is linked to the width of the base of T_g, E^i changes for each N. In other words, a new boundary value problem is solved for each N. As a result of this, the solution for the coefficient c_g may not converge. To circumvent this problem, an extended delta gap source model is introduced. The extended delta gap source model, E_g, is a unit strength electric field of two variables that is impressed over an artificially constructed gap of length δ which may be written symbolically as

$$E_g^P = u_z \frac{1}{\rho} \delta(\rho - a_w)[u(z + \frac{\delta}{2}) - u(z - \frac{\delta}{2})]. \tag{A.2}$$

The superscript P is used to indicate that the z variation of this field is just a unit amplitude pulse which spans the δ gap. The gap length, δ, is treated as an unknown constant to be determined by requiring the tested gap field to be such that $\sum <J_j, E_g> = 1$. Formation of the inner product, results in the following equation.

77

$$\sum_{1}^{N} \int_{\phi=0}^{2\pi} \int_{\rho=0}^{\infty} \int_{z=-\delta/2}^{\delta/2} \frac{T_j}{2\pi a_w} \frac{1}{\rho} \delta(\rho - a_w)[u(z+\frac{\delta}{2}) - u(z-\frac{\delta}{2})]\rho dz d\rho d\phi = 1 \qquad (A.3)$$

Upon solution, we have that $\delta = a_w$. This result could also have been obtained by inspection, since in the limit $a_w \to 0$, the integrand of (A.3) also becomes a delta function in z due to the term $[u(z+\delta/2)-u(z-\delta/2)]/a_w$. The expanded delta source model is then implemented by replacing $\underline{E}_s^P/a_w$ of (A.2) with the Gaussian function

$$\underline{E}_s^G = \mathbf{u}_z \frac{1}{\sqrt{2\pi}\,\delta_0} e^{\frac{-z^2}{2\delta_0^2}} \qquad (A.4)$$

where δ_0 is now equal to $a_w/2$. The reason for this replacement is that the Gaussian function, $\underline{E}_s^G$, yields a solution which converges more rapidly, and may be numerically integrated with more ease than $\underline{E}_s^P/a_w$. Since δ_0 is a fixed length, and the Gaussian function is smooth, a stable solution can be achieved since the electric field boundary function will be theoretically satisfied for all N. This model is also appealing because this delta gap model will never have an infinite capacitance. This is obvious: since as $\delta \to 0$, $a_w \to 0$; thus, there is no dipole. For the results presented in the next section, when the MoM impedance matrix elements are computed, the exact kernel is used for the wire self terms [18], i.e., when the testing and basis functions overlap. For the non-self terms, the reduced kernel is used.

Numerical Results: Using measured data collected by R.W.P King [39] as a basis for comparison, computed current distributions for four ground plane backed monopole antennas are presented in Fig. A2 through Fig. A5. Both $\delta(z)$ and Gaussian forcing functions are used. As can be seen from these figures, the two numerical solutions agree quite well except for the current near the source location. The Gaussian forcing function gives much better agreement with King's measured current distributions. Fig. A6 and Fig. A7 are plots of computed and measured input

78

admittances as a function of h/a_w ("Slenderness Ratio") for a $\lambda_0/8$ and a $3\lambda_0/8$ monopole respectively. As can be seen, the computed admittances using the Gaussian delta source model are in excellent agreement with the measured admittances for a wide range of wire radii. However, the $\delta(z)$ source model performs poorly for the thicker monopoles. Note that the behavior of the computed admittances as a function of h/a_w are consistent for the monopoles under consideration. Since the convergence problem is associated with the dipole susceptance, Figs. A8 and A9 are convergence plots of the dipole susceptances as a function of N for the antennas whose current distributions are given in Figs. A2 through A5. These figures illustrate the stability of the Gaussian forcing function. Accurate values for input impedance can be obtained with as few as 20 basis functions per wavelength.

Using measured input impedances for the powdered CDRA described in Chapter 3 as a basis for comparison, the stability of the new delta source model was compared to two other delta source models. The geometry of the CDRA is shown in Fig. A1b with the labels used in this section. The delta sources models used in this study are the following:

a) The forcing function $\delta(z)$.

b) The Gaussian distribution given in equation (A.4).

c) The approximate delta function $[u(z+\delta/2)-u(z-\delta/2)]/a_w$ identified as $1/\delta$ in the figures.

Computed input impedances as a function of frequency for three different DR antennas are presented in Figs. A10 through A17. As can be seen from these figures, the Gaussian delta source model outperforms the competing delta source models in predicting the antenna resonant frequency and impedance levels. Fig. A18 through A20 are computed current distributions for the three delta source models. As can be seen from these figures, all show reasonable agreement except near the source location.

Conclusions: A novel delta source model, which is very simple to implement, has been

introduced and validated through numerical convergence tests and measurements. This new delta source provides a simple and accurate means of predicting antenna input impedance. As demonstrated in this work, loaded monopole antennas may also be successfully analyzed using this new delta source model.
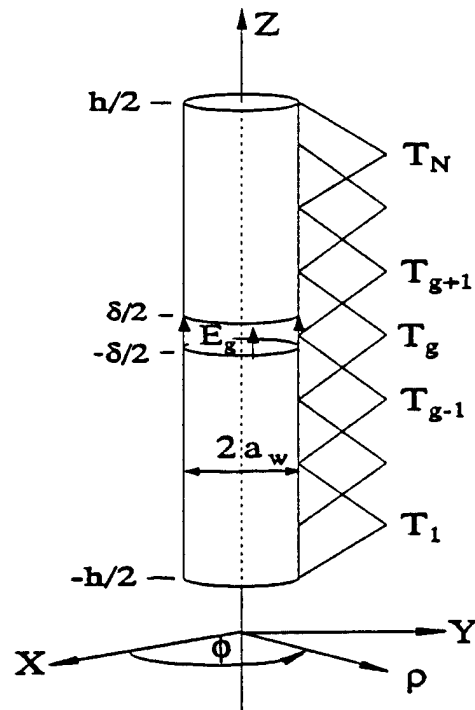
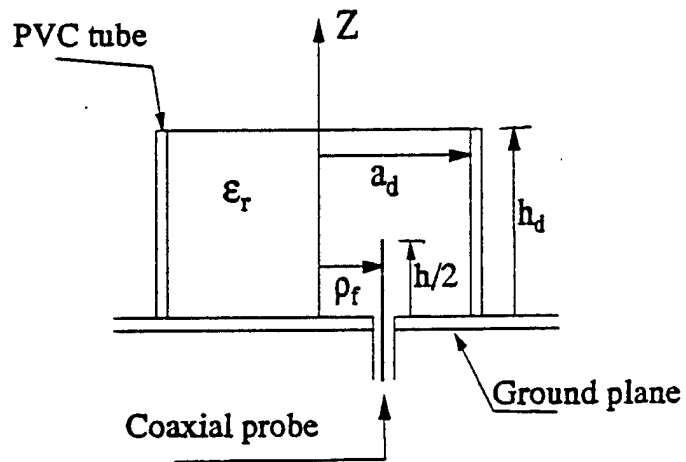Fig. A1a. Geometry of the cylindrical dipole.
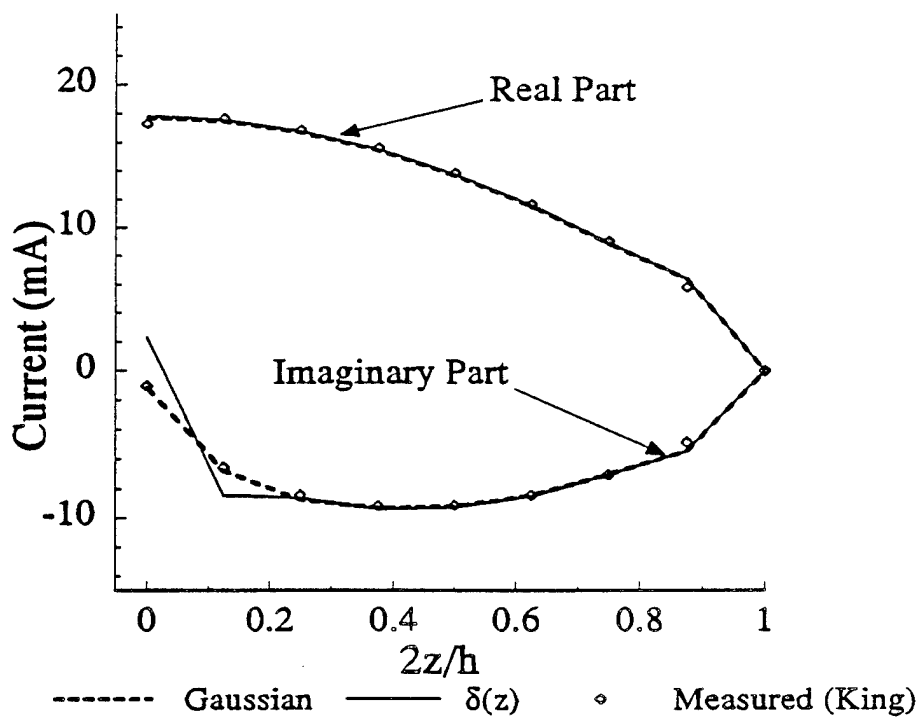

Fig. A1b. Geometry of the CDRA.

81

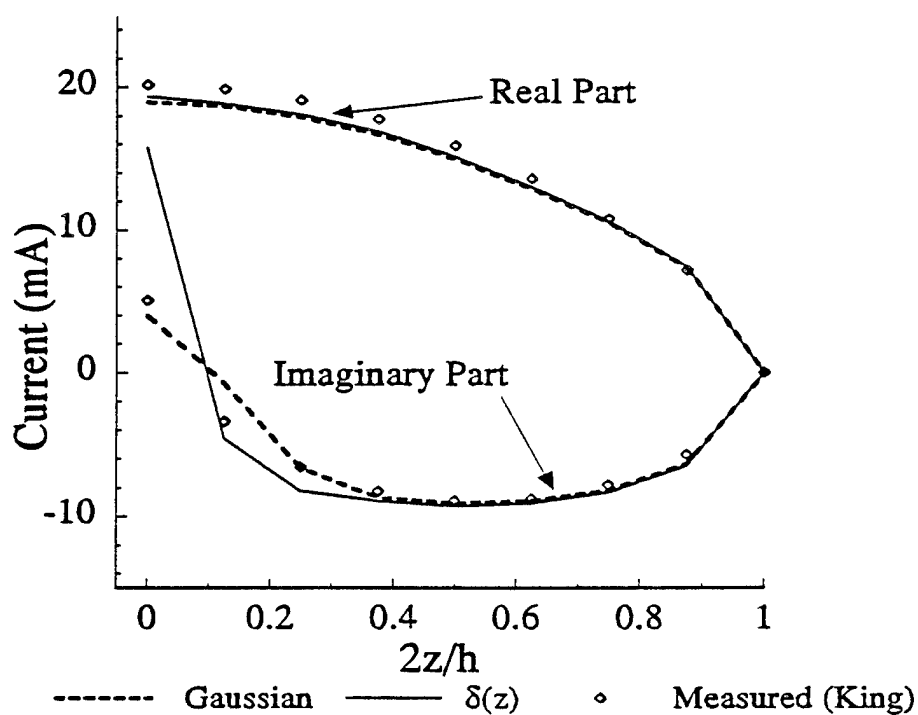Fig. A2. Current distribution for $\lambda_0/4$ monopole with $a_w=0.0254\lambda_0$ and $N=15$.

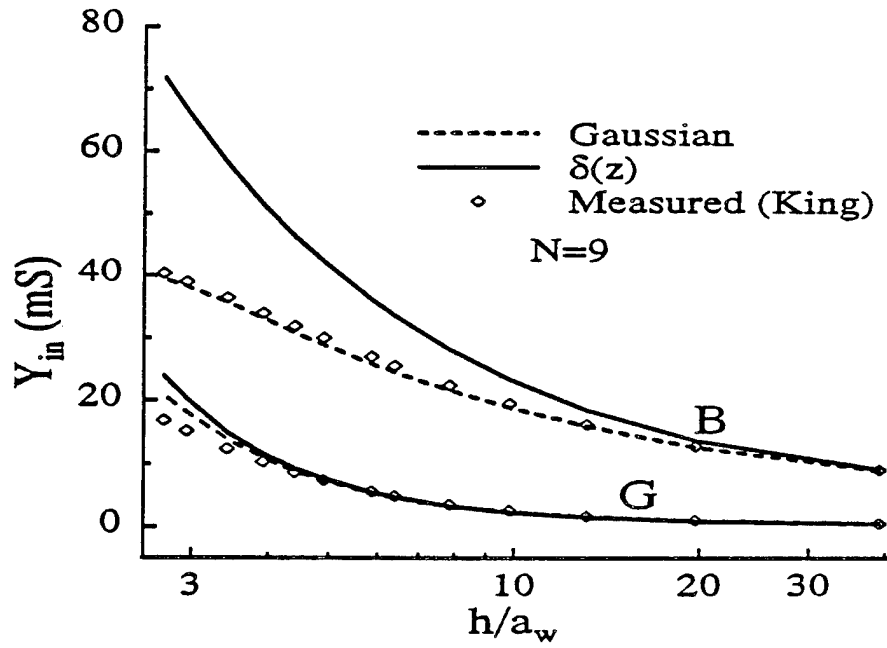Fig. A3. Current distribution for $\lambda_0/4$ monopole with $a_w=0.0509\lambda_0$ and $N=15$.
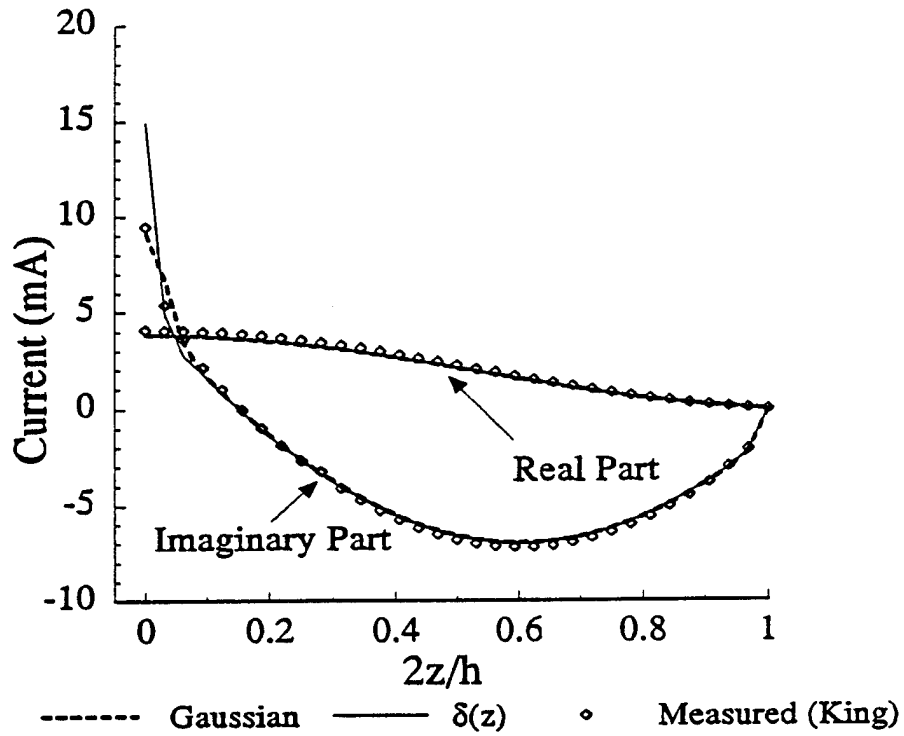
Fig. A4. Current distribution for $\lambda_0/2$ monopole with $a_w = 0.0254\lambda_0$ and N=63.
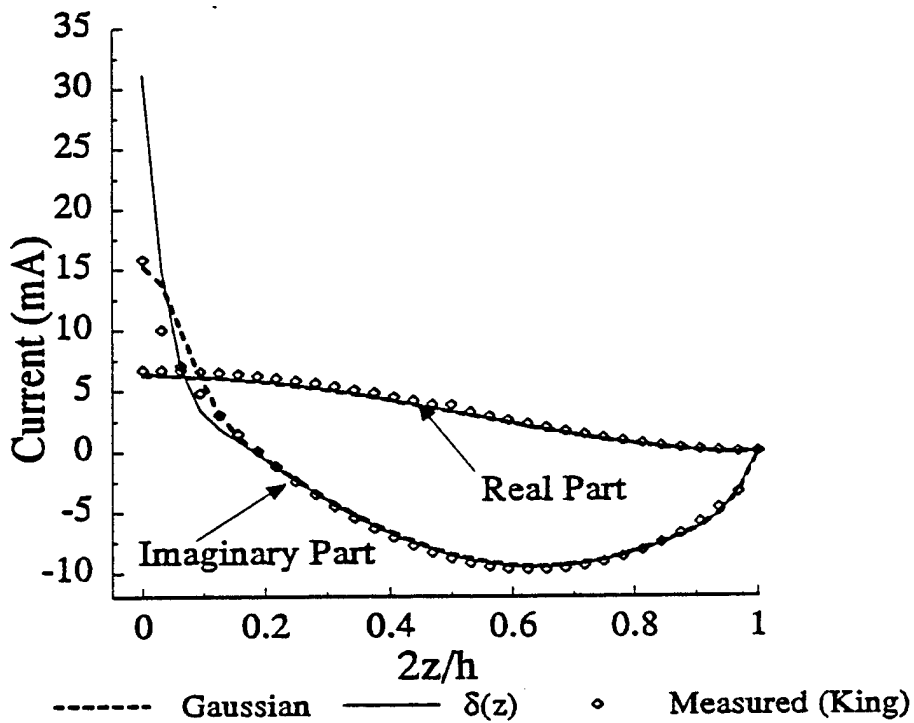
Fig. A5. Current distribution for $\lambda_0/2$ monopole with $a_w = 0.0509\lambda_0$ and N=63.

83

Fig. A6. Input admittance vs. h/a$_w$ for a λ_0/8 monopole.
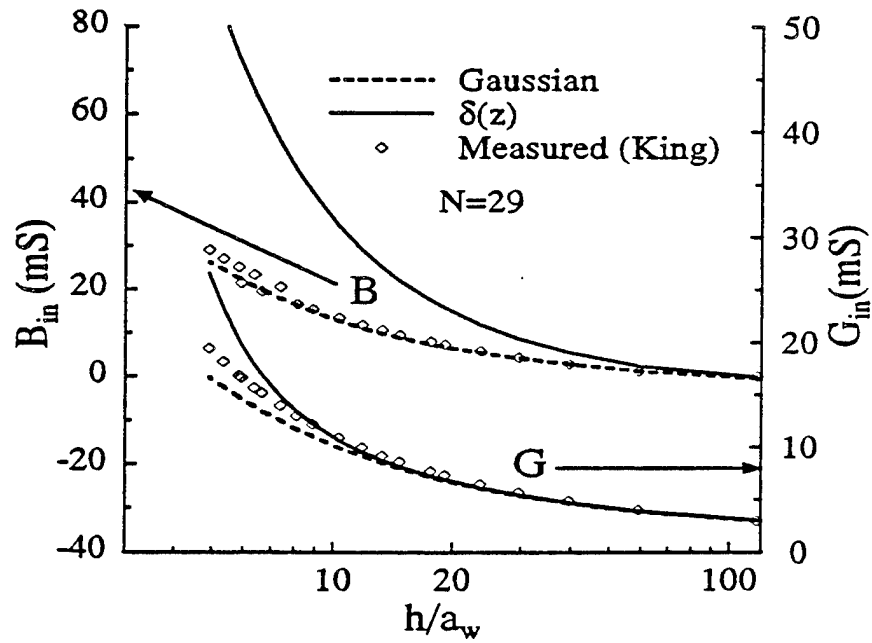
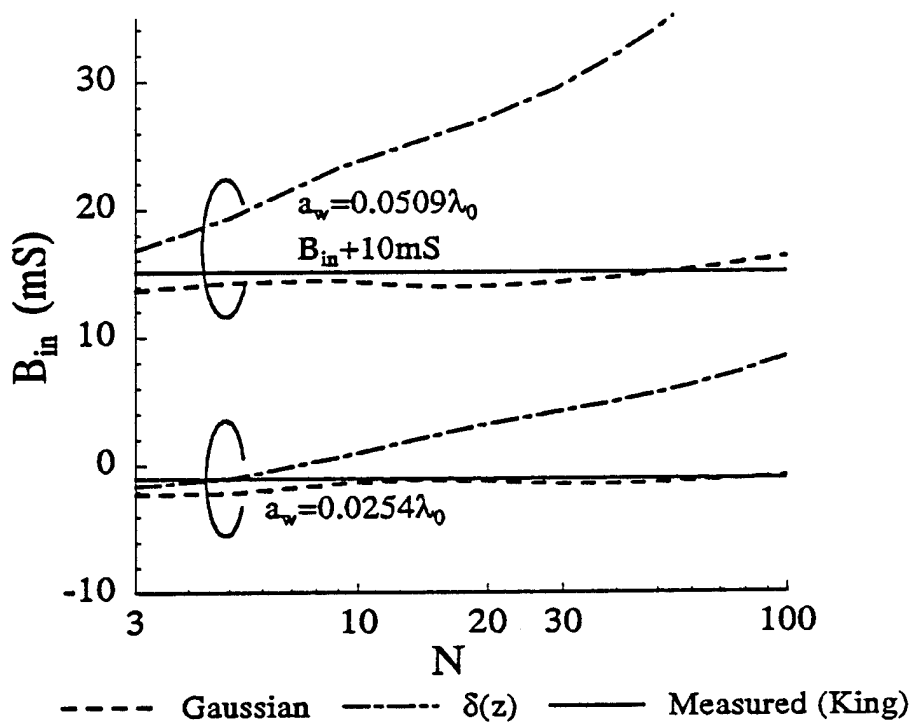Fig. A7. Input admittance vs. h/a$_w$ for a 3λ_0/8 monopole.

84

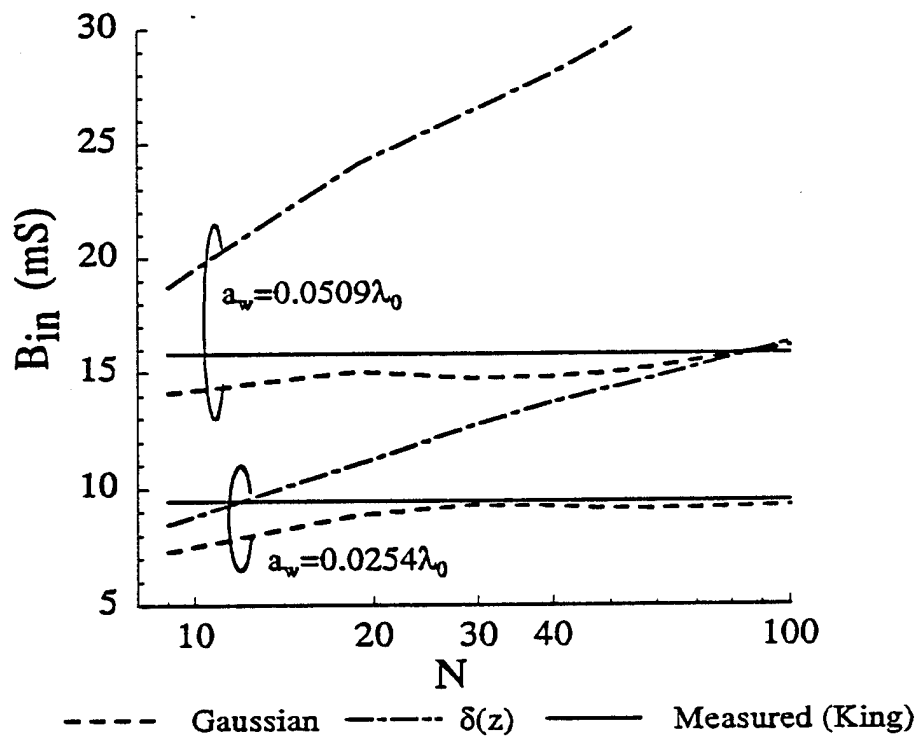Fig. A8. Input susceptance vs. N for $\lambda_0/4$ monopole.

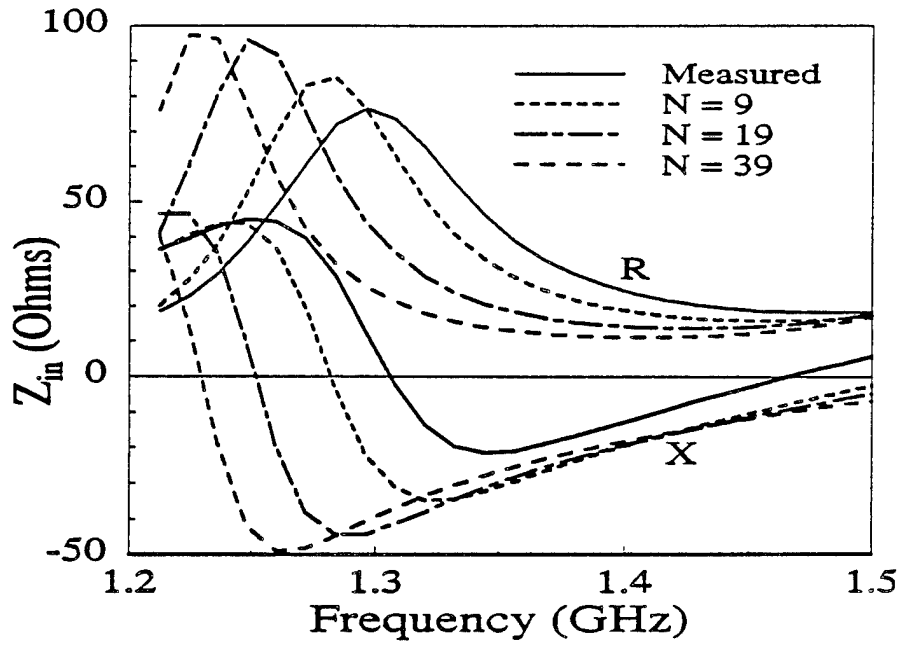Fig. A9. Input susceptance vs. N for $\lambda_0/2$ monopole.

85

Fig. A10. Input impedance vs. Frequency for different N using forcing function $\delta(z)$. CDRA parameters: $a_w=1.295$mm, $h/2=2.0$cm, $\rho_f=1.4$cm, $h_d=2.6$cm, $a_d=2.75$cm, and $\epsilon_r=12.0$.
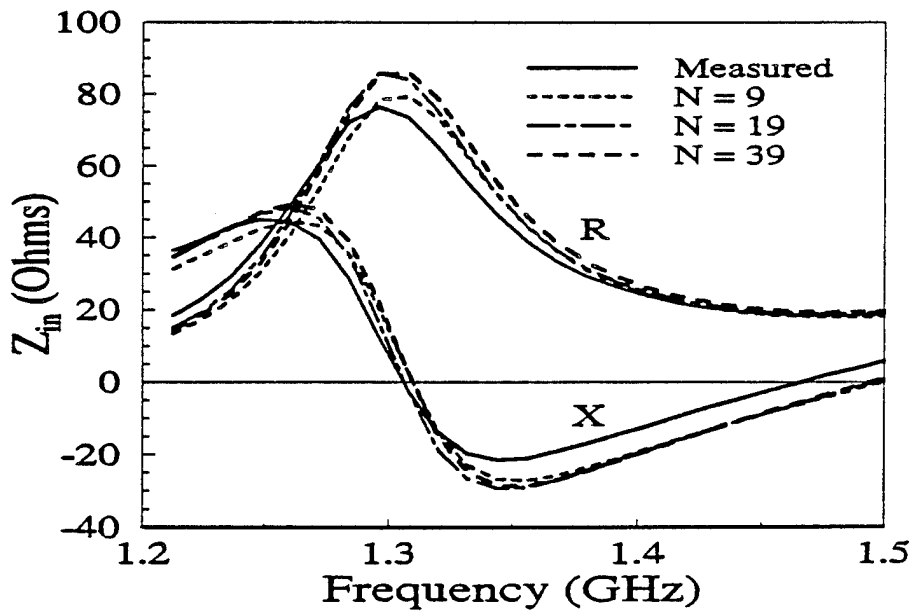

Fig. A11. Input impedance vs. Frequency for different N using Gaussian forcing function. CDRA parameters: $a_w=1.295$mm, $h/2=2.0$cm, $\rho_f=1.4$cm, $h_d=2.6$cm, $a_d=2.75$cm, and $\epsilon_r=12.0$.

Fig. A12. Input impedance vs. Frequency for different N using forcing function
$1/\delta$. CDRA parameters: a_w=1.295mm, h/2=2.0cm, ρ_f=1.4cm, h_d=2.6cm,
a_d=2.75cm, and ϵ_r=12.0.

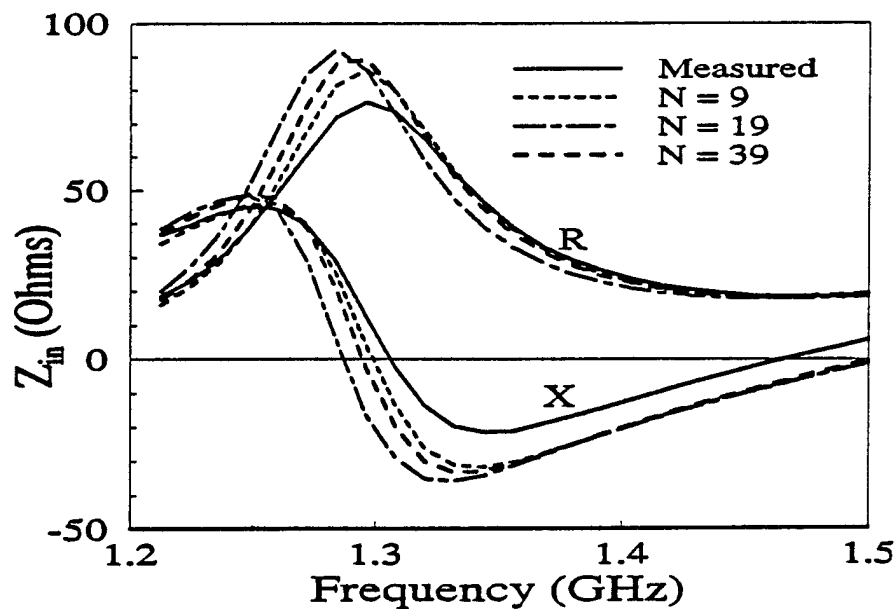

Fig. A13. Input impedance vs. Frequency for different N using forcing function
$\delta(z)$. CDRA parameters: a_w=0.381mm, h/2=2.0cm, ρ_f=1.4cm, h_d=2.6cm,
a_d=2.75cm, and ϵ_r=12.0.

87

Fig. A14. Input impedance vs. Frequency for different N using Gaussian forcing function. CDRA parameters: $a_w = 0.381$mm, $h/2 = 2.0$cm, $\rho_f = 1.4$cm, $h_d = 2.6$cm, $a_d = 2.75$cm, and $\epsilon_r = 12.0$.
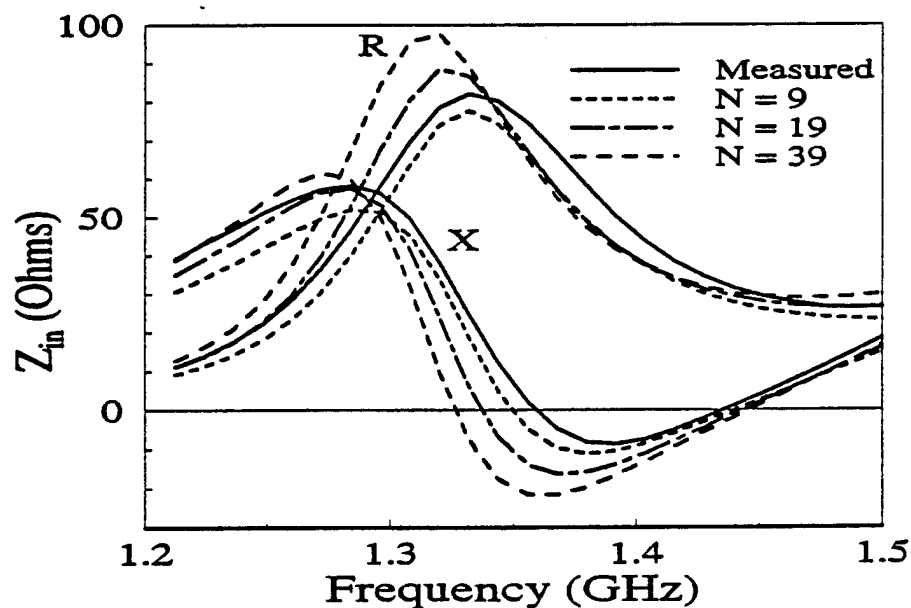

Fig. A15. Input impedance vs. Frequency for different N using forcing function $1/\delta$. CDRA parameters: $a_w = 0.381$mm, $h/2 = 2.0$cm, $\rho_f = 1.4$cm, $h_d = 2.6$cm, $a_d = 2.75$cm, and $\epsilon_r = 12.0$.

88

Fig. A16. Input impedance vs. Frequency for different N using forcing function $\delta(z)$. CDRA parameters: $a_w = 0.381$mm, $h/2 = 1.369$cm, $\rho_f = 0.0$cm, $h_d = 2.6$cm, $a_d = 2.75$cm, and $\epsilon_r = 12.0$.
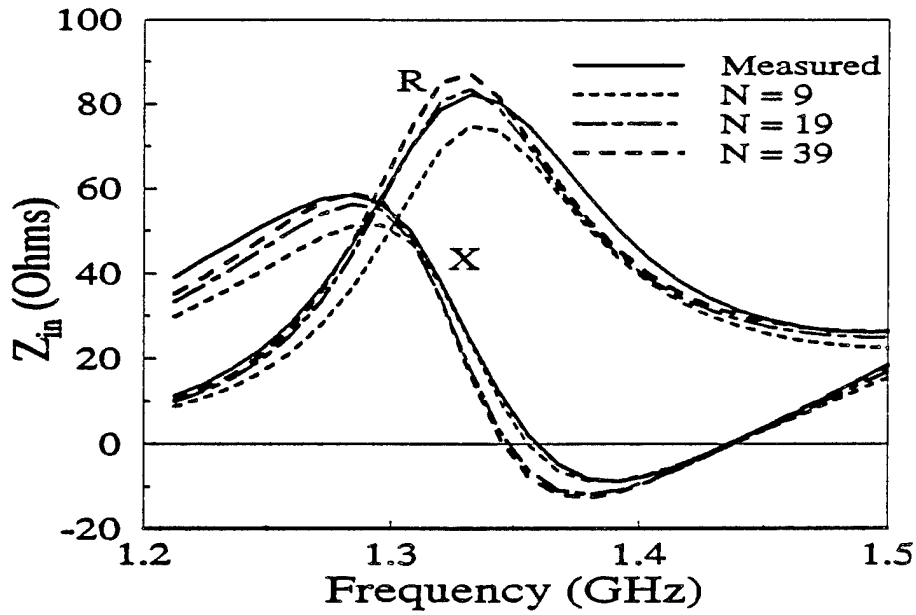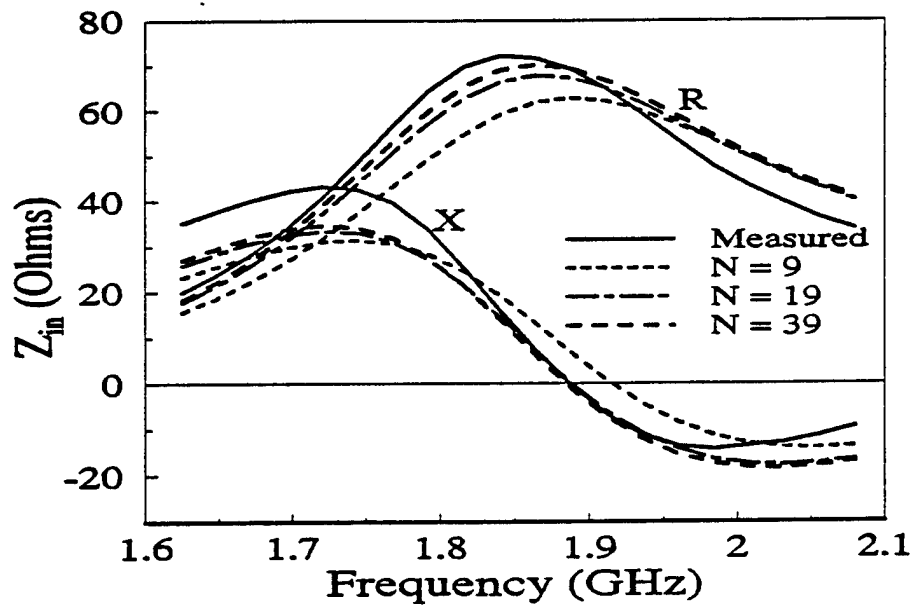

Fig. A17. Input impedance vs. Frequency for different N using Gaussian forcing function. CDRA parameters: $a_w = 0.381$mm, $h/2 = 1.369$cm, $\rho_f = 0.0$cm, $h_d = 2.6$cm, $a_d = 2.75$cm, and $\epsilon_r = 12.0$.

89
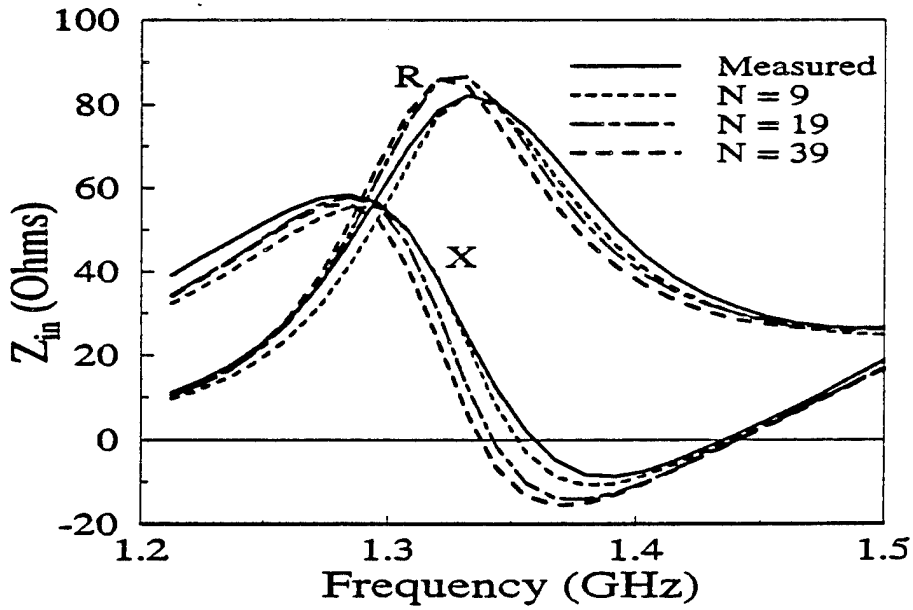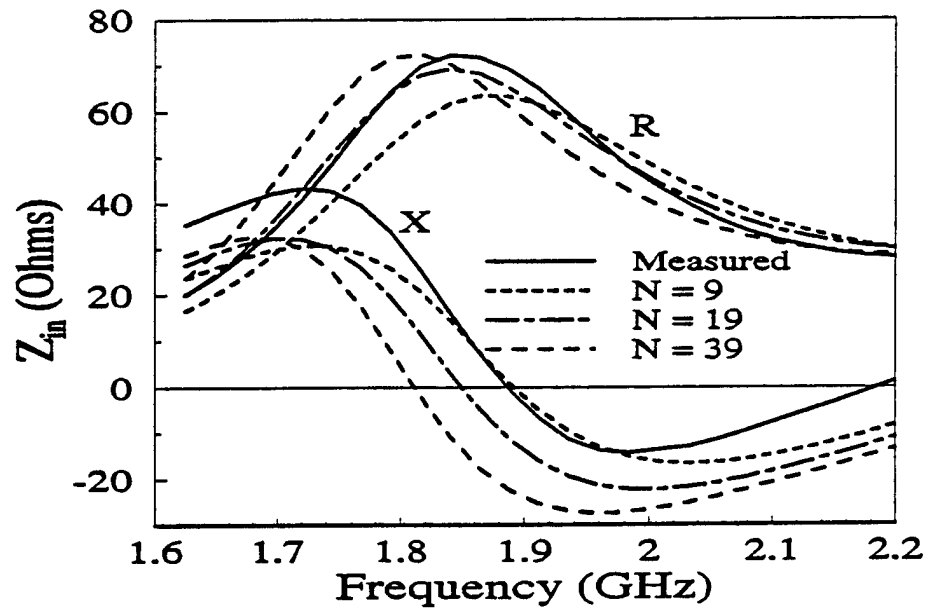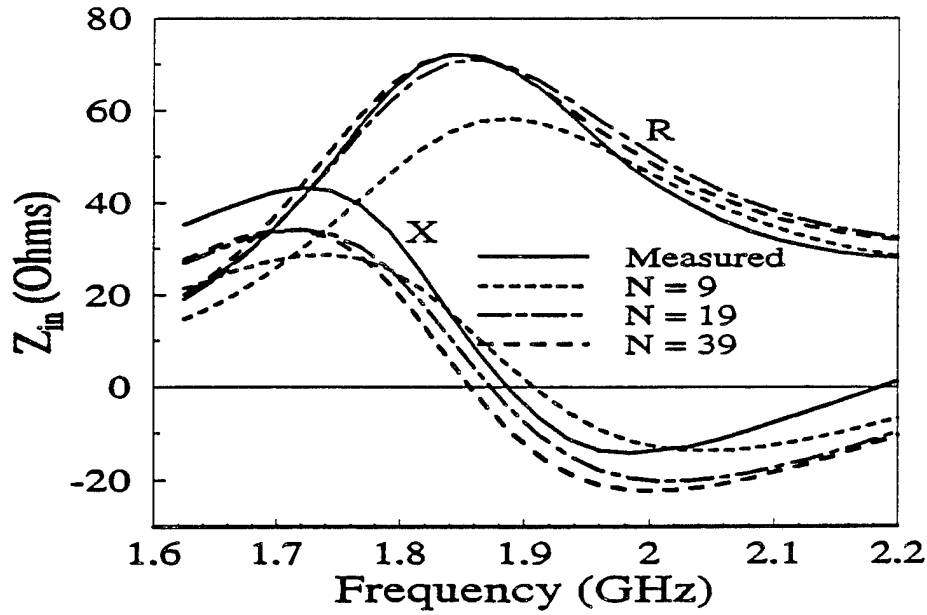
Fig. A18. Input impedance vs. Frequency for different N using forcing function
$1/\delta$. CDRA parameters: $a_w=0.381$mm, $h/2=1.369$cm, $\rho_f=0.0$cm, $h_d=2.6$cm,
$a_d=2.75$cm, and $\epsilon_r=12.0$.
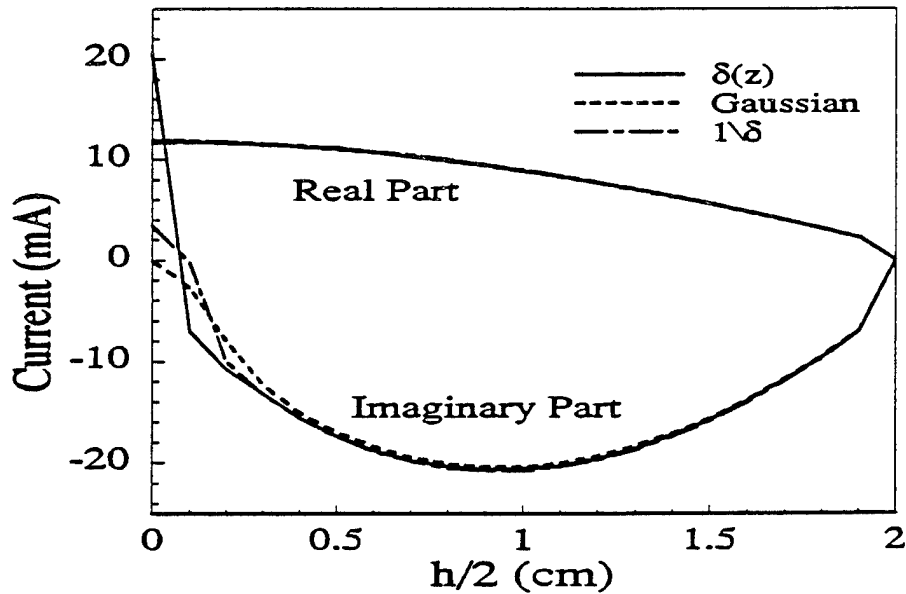
Fig. A19. Current distribution on coaxial probe for three delta source models
with $N=39$, $f=1.31$GHz, $a_w=1.295$mm, $h/2=2.0$cm, $\rho_f=1.4$cm, $h_d=2.6$cm,
$a_d=2.75$cm, and $\epsilon_r=12.0$.

Fig. A20. Current distribution on coaxial probe for three delta source models with N=39, f=1.35GHz, a_w=0.381mm, h/2=2.0cm, ρ_f=1.4cm, h_d=2.6cm, a_d=2.75cm, and ϵ_r=12.0.

Fig. A21. Current distribution on coaxial probe for three delta source models with N=39, f=1.89GHz, a_w=0.381mm, h/2=1.369cm, ρ_f=0.0cm, h_d=2.6cm, a_d=2.75cm, and ϵ_r=12.0.

Appendix B

BOR/wire coupling matrix elements

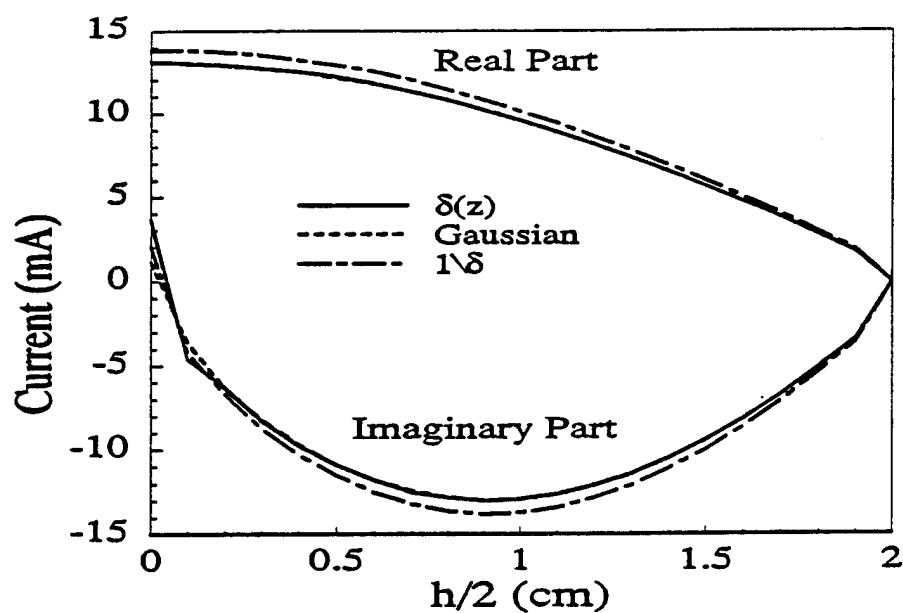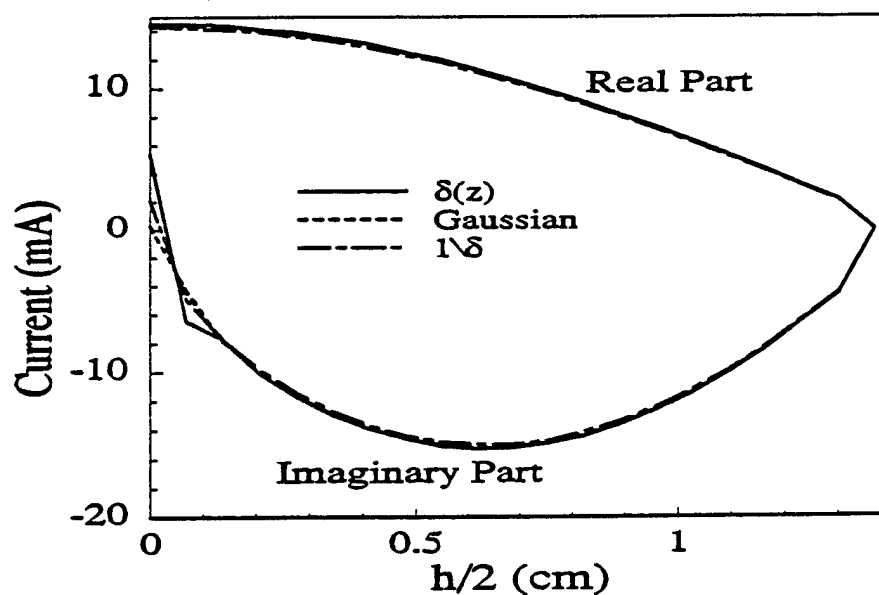Integral expressions for the matrix elements of the coupling block $[BW]_a$ are given by

$$Z_{t,w}{}^q = \frac{jk_q\eta_q}{4\pi}\int_{N_t} dt \int_0^{2\pi} d\phi \int_{P_w} d\dot{w}\{T(t)T(\dot{w})u_t \cdot u_w - \frac{1}{k_q{}^2}T'(t)T'(\dot{w})\} \cdot \{\frac{e^{-j(k_q R + n\phi)}}{R}\} \qquad (B1)$$

$$Z_{\phi,w}{}^q = \frac{jk_q\eta_q}{4\pi}\int_{N_t} dt \int_0^{2\pi} d\phi \int_{P_w} d\dot{w}\{T(t)T(\dot{w})u_\phi \cdot u_w + \frac{jn}{k_q{}^2\rho}T(t)T'(\dot{w})\} \cdot \{\frac{e^{-j(k_q R + n\phi)}}{R}\} \qquad (B2)$$

$$Y_{t,w}{}^q = \frac{1}{4\pi}\int_{N_t} dt \int_0^{2\pi} d\phi \int_{P_w} d\dot{w} T(t)T(\dot{w})u_t \cdot u_w \times \underline{R}\frac{(1+jk_q R)}{R^3}e^{-j(k_q R + n\phi)} \qquad (B3)$$

$$Y_{\phi,w}{}^q = \frac{1}{4\pi}\int_{N_t} dt \int_0^{2\pi} d\phi \int_{P_w} d\dot{w} T(t)T(\dot{w})u_\phi \cdot u_w \times \underline{R}\frac{(1+jk_q R)}{R^3}e^{-j(k_q R + n\phi)} \qquad (B4)$$

where N_t is the tth testing function on S_{de} and p_w is the pth basis function on S_{wq}. $\underline{R} = \underline{r} - \underline{f}$ and $R = |\underline{R}|$. The geometrical quantities are illustrated in Fig. B1.

As discussed in the body of this work, the triangle and rooftop basis functions are used on the wire and the slot, respectively. The elements for the BOR/slot may be obtained from the BOR/wire elements with a minor adjustment. The BOR and wire both use four weighted impulses as a representation for the triangle function. This weighted impulse representation is in essence a four point rectangular rule integration. For the BOR, the triangle function is given as

92

$$\rho f_i(t) = \sum_{p=1}^{4} T(t)_{p+4i-4} \delta(t-t_{p+2i-2}) \tag{B5}$$

where $\delta(t)$ is the unit impulse function and T is defined as shown in Fig. B2, for $i=1$ with

$$T_1 = \frac{d_1^2}{2(d_1+d_2)}$$

$$T_2 = \frac{(d_1+0.5d_2)d_2}{d_1+d_2}$$

$$T_3 = \frac{(d_4+0.5d_3)d_4}{d_3+d_4} \tag{B6}$$

$$T_4 = \frac{d_4^2}{2(d_3+d_4)}$$

and for its derivative,

$$\frac{d}{dt}(\rho f_i(t)) = \sum_{p=1}^{4} T'(t)_{p+4i-4} \delta(t-t_{p+2i-2}) \tag{B7}$$

as shown in Fig.B3 for $i=1$, T'_i is given by

$$T'_1 = \frac{d_1}{d_1+d_2}$$

$$T'_2 = \frac{d_2}{d_1+d_2}$$

$$T'_3 = \frac{-d_3}{d_3+d_4} \tag{B8}$$

$$T'_4 = \frac{-d_4}{d_3+d_4}$$

93

In Fig. B1, ρ, ϕ, and z are cylindrical coordinates, and t, ϕ form an orthogonal curvilinear coordinate system on the surface of the BOR where u_t and u_ϕ are orthogonal unit vectors in the t and ϕ directions, respectively. The outward normal to the surface is defined as $u_n = u_t \times u_\phi$. A unit vector on the wire (slot) is denoted as u_w (u_s). Source and field quantities are denoted as primed and unprimed, respectively. The angle between the Z-axis and $\pm u_t$ is denoted as $\pm v$.

Defining the triangle function for the wire and its derivative as

$$f_i(t) = \sum_{p=1}^{4} T(w)_{p+4i-4} \delta(w - w_{p+2i-2}) \tag{B9}$$

$$\frac{d}{dt} f_i(w) = \sum_{p=1}^{4} T'(w)_{p+4i-4} \delta(w - w_{p+2i-2}) \tag{B10}$$

the expressions for the coupling blocks (B1) to (B4) may be written as

$$Z_{t,w}^{q} = \frac{jk_q \eta_q}{4\pi} \sum_{p=1}^{4} \sum_{i=1}^{4} \{ T_{p'}(t) T_{i'}(w) \{ \sin v_{i'} [w_{x_{i'}} \cos\phi + w_{y_{i'}} \sin\phi] + w_{z_{i'}} \cos v_{i'} \}$$
$$- \frac{T'_{p'}(t) T'_{i'}(w)}{k_q^2} \} \int_{-\pi}^{\pi} \frac{e^{-j(k_q r + m\phi)}}{r} d\phi \tag{B11}$$

$$Z_{\phi,w}^{q} = \frac{jk_q \eta_q}{4\pi} \sum_{p=1}^{4} \sum_{i=1}^{4} \{ T_{p'}(t) T_{i'}(w) [-w_{x_{i'}} \sin\phi + w_{y_{i'}} \cos\phi]$$
$$+ \frac{T_{p'}(t) T'_{i'}(w)}{k_q^2 \rho_{i'}} \} \int_{-\pi}^{\pi} \frac{e^{-j(k_q r + m\phi)}}{r} d\phi \tag{B12}$$

94

$$Y_{t.w}^q = \frac{1}{4\pi} \sum_{p=1}^{4} \sum_{l=1}^{4} \{T_{p'}(t)T_{l'}(w)\{w_{x_{i'}}[\sin\nu_{i'}(z_{i'}-z_{j'})\sin\phi - \cos\nu_{i'}(\rho_{i'}\sin\phi - y_{j'})]$$
$$-w_{y_{i'}}[\sin\nu_{i'}(z_{i'}-z_{j'})\cos\phi - \cos\nu_{i'}(\rho_{i'}\cos\phi - x_{j'})]$$
$$+w_{z_{i'}}[\sin\nu_{i'}(\rho_{i'}\sin\phi - y_{j'})\cos\phi - \sin\nu_{i'}(\rho_{i'}\cos\phi - x_{j'})\sin\phi]\} \tag{B13}$$
$$(1+jk_q r)\int_{-\pi}^{\pi} \frac{e^{-j(k_q r + m\phi)}}{r^3} d\phi$$

$$Y_{\phi.w}^q = \frac{1}{4\pi} \sum_{p=1}^{4} \sum_{l=1}^{4} \{T_{p'}(t)T_{l'}(w)\{w_{x_{i'}}\cos\phi(z_{j'}-z_{i'})$$
$$-w_{y_{i'}}\sin\phi(z_{i'}-z_{j'})$$
$$+w_{z_{i'}}[(\rho_{i'}\sin\phi - y_{i'})\sin\phi + \cos\phi(\rho_{i'}\cos\phi - x_{j'})]\} \tag{B14}$$
$$(1+jk_q r)\int_{-\pi}^{\pi} \frac{e^{-j(k_q r + m\phi)}}{r^3} d\phi$$

where r is given by

$$r = \{(\rho_{i'}\cos\phi - x_{j'})^2 + (\rho_{i'}\sin\phi - y_{j'})^2 + (z_{i'} - z_{j'})^2\}^{1/2} \tag{B15}$$

and $\mathbf{u}_w = w_x\mathbf{u}_x + w_y\mathbf{u}_y + w_z\mathbf{u}_z.$

The summation indices are given by

$$p' = p + 4i - 4$$
$$l' = l + 4j - 4$$
$$i' = p + 2i - 2 \tag{B16}$$
$$j' = l + 2i - 2$$

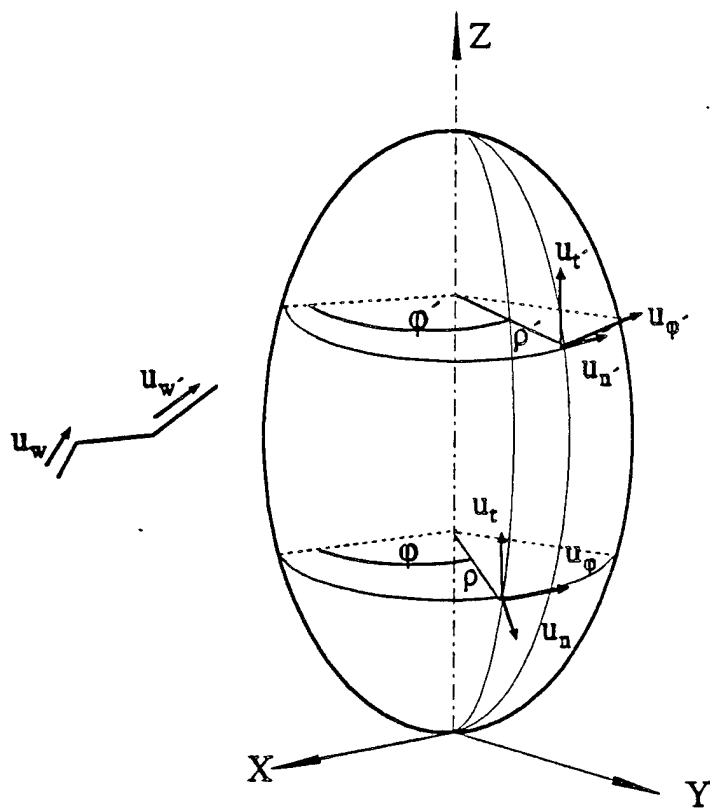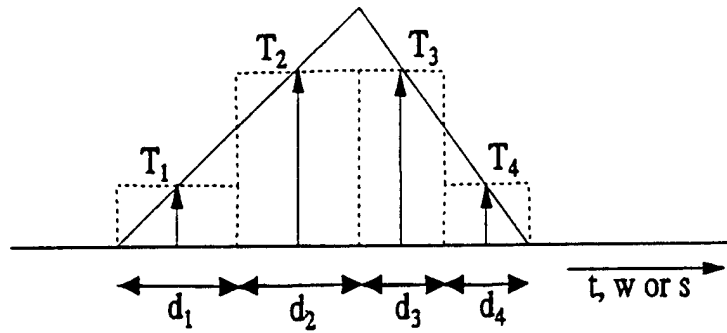Fig. B1. Geometry of the BOR/wire.

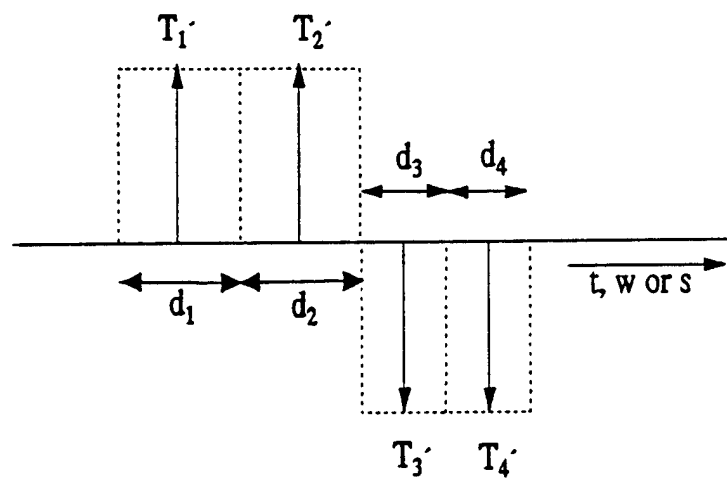Fig. B2.a. The triangle function approximation.

Fig. B2.b. The derivative of the triangle function
approximation.

97

APPENDIX C

BOR/slot Coupling Matrix Elements

The expressions for the BOR/slot interaction elements are obtained by substituting the appropriate dual parameters. Since the current on the thin slot is axially directed, it is not necessary to perform a numerical integration for these matrix elements along the coordinate which corresponds to the width of the slot. Instead, one simply multiplies the dual of (B1) to (B4) by the width of the slot to obtain the total magnetic current. The symbol Λ is used to represent the rooftop function even though it is identical to the triangle function.

After doing so, the integral expressions for the matrix elements of the coupling block $[BS_s]_a$ are given by

$$Z_{t,s}^d = \frac{jk_d}{4\pi\eta_d} \int_{N_1} dt \int_0^{2\pi} d\phi \int_{P_s} d\mathcal{S}\{T(t)\Lambda(\mathcal{S})u_t \cdot u_s -\frac{1}{k_d^2}T'(t)\Lambda'(\mathcal{S})\}\frac{e^{-j(k_d R + n\phi)}}{R} \tag{C1}$$

$$Z_{\phi,s}^d = \frac{jk_d}{4\pi\eta_d} \int_{N_1} dt \int_0^{2\pi} d\phi \int_{P_s} d\mathcal{S}\{T(t)\Lambda(\mathcal{S})u_\phi \cdot u_s +\frac{jn}{k_d^2\rho}T(t)\Lambda'(\mathcal{S})\}\frac{e^{-j(k_d R + n\phi)}}{R} \tag{C2}$$

$$Y_{t,s}^d = \frac{1}{4\pi} \int_{N_1} dt \int_0^{2\pi} d\phi \int_{P_s} d\mathcal{S}\, T(t)\Lambda(\mathcal{S})u_t \cdot u_s \times \underline{R}\frac{(1+jk_d R)}{R^3}e^{-j(k_d R + n\phi)} \tag{C3}$$

$$Y_{\phi,s}^d = \frac{1}{4\pi} \int_{N_1} dt \int_0^{2\pi} d\phi \int_{P_s} d\mathcal{S}\, T(t)\Lambda(\mathcal{S})u_\phi \cdot u_s \times \underline{R}\frac{(1+jk_d R)}{R^3}e^{-j(k_d R + n\phi)} \tag{C4}$$

where N_t is the tth testing function on S_{d_s} and p_s is the pth basis function on S_s. $\underline{R} = \underline{r} - \underline{f}$ and $R = |\underline{R}|$. Again, as in the case of the BOR/wire coupling matrix blocks, the 4 impulse representation for the rooftop (triangle) function and its derivative are used for the evaluation of the above integral expressions. By substituting the dual parameters into equations (B11-B14), explicit expressions for the BOR/slot coupling matrix blocks may be obtained.

Slot/microstrip Spectral Domain Green's Functions

The following are the required Green's function components from Ref. [36]:

$G_{xx}^{EJ} =$ E_x at (x,y,d) due to a unit x electric current element at (x_0,y_0,d)

$G_{yx}^{HJ} =$ H_y at $(x,y,0)$ due to a unit x electric current element at (x_0,y_0,d)

$G_{yy}^{HM} =$ H_y at $(x,y,0)$ due to a unit y magnetic current element at $(x_0,y_0,0)$

$G_{xy}^{EM} =$ E_x at (x,y,d) due to a unit y magnetic current element at $(x_0,y_0,0)$.

Given that the Fourier transform relation is defined as

$$G(x,y) = \frac{1}{4\pi^2} \int\limits_{-\infty}^{+\infty}\int \tilde{G}(k_x,k_y) e^{jk_x(x-x_0)} e^{jk_y(y-y_0)} dk_x dk_y. \tag{D1}$$

Then,

$$\tilde{G}_{xx}^{EJ} = j\frac{\eta_0}{k_0}\{(\epsilon_s k_0^2 - k_x^2)k_2\cos(k_1 d) + jk_1(k_0^2 - k_x^2)\sin(k_1 d)\}\ \frac{\sin(k_1 d)}{T_e T_m} \tag{D2}$$

$$\tilde{G}_{yx}^{HJ} = -\tilde{G}_{xy}^{EM} = \frac{-jk_x^2(\epsilon_s - 1)\sin(k_1 d)}{T_e T_m} + \frac{k_1}{T_e} \tag{D3}$$

$$\tilde{G}_{yy}^{HM} = -\frac{j}{k_0\eta_0}[\frac{j(k_1\cos(k_1 d) + jk_2\epsilon_s\sin(k_1 d))(\epsilon_s k_0^2 - k_y^2)}{k_1 T_m} - \frac{jk_y^2 k_1(\epsilon_s - 1)}{T_e T_m}] \tag{D4}$$

where,

$$T_e = k_1\cos(k_1 d) + jk_2\sin(k_1 d) \tag{D5}$$

$$T_m = \epsilon_s k_2\cos(k_1 d) + jk_1\sin(k_1 d) \tag{D6}$$

$$k_1^2 = \epsilon_s k_0^2 - \beta^2, \qquad \text{Im } k_1 < 0 \tag{D7}$$

$$k_2^2 = k_0^2 - \beta^2, \qquad \text{Im } k_2 < 0 \tag{D8}$$

$$\beta^2 = k_x^2 + k_y^2 \tag{D9}$$

$$k_0^2 = \omega^2 \mu_0 \epsilon_0 \tag{D10}$$

Given that the Fourier transform relation is defined as

$$F(k_x) = \int_{-\infty}^{+\infty} f(x) e^{jk_x x} dx, \tag{D11}$$

the following components of the basis/testing functions,

$$\text{pulse function: } f_u(y) = \begin{cases} 1/W, & \text{for } |y| < W/2 \\ 0, & \text{for } |y| > W/2 \end{cases} \tag{D12}$$

$$\text{triangle function: } f_p(y) = \begin{cases} 1 - \dfrac{2|y|}{h}, & \text{for } |y| < h/2 \\ 0, & \text{for } |y| > h/2 \end{cases} \tag{D13}$$

where W is the width of the basis/testing function, and h is the length of the base of the triangle function, have the following Fourier transforms, respectively:

$$F_u(k_y) = \text{sinc}(k_y W/2) \tag{D14}$$

$$F_p(k_y) = \frac{h}{2} \text{sinc}^2(k_y h/4) \tag{D15}$$

It should be noted that the expression (D4) differs from that provided in [36] in that the contribution to the Green's function from the upper half space has been removed.

REFERENCES

[1] S.A. Long, M.W. McAllister, and L.C. Shen, "The resonant dielectric cavity antenna," *IEEE. Trans. Antennas Propagat.*, vol. AP-31, No. 3, pp. 406-412, 1983.

[2] M.W. McAllister and S. A. Long, "Resonant hemispherical dielectric antenna," *Electronic Letters*, vol. 20, pp. 657-658, 1984.

[3] A.A. Kishk, H.A. Auda, and B.C. Ahn, "Accurate predictions of radiation patterns of dielectric -resonator antennas," *Electronic Letters*, vol. 23, No. 25, pp. 1374-1375, 1987.

[4] A.A. Kishk, H.A. Auda, and B.C. Ahn, "Radiation characteristics of cylindrical dielectric resonator antennas with new applications," *IEEE Antennas and Propagat. Society Newsletter*, vol. 31, pp. 7-16, Feb. 1989.

[5] W. Huang, A.A. Kishk, and A.W. Glisson, "Analysis of a thick monopole antenna loaded with dielectric material," *AEÜ*, April, 1994 (in press).

[6] D. Kajfez and P. Guillon, Editors, *Dielectric Resonators*, Norwood, MA., Artech House, Inc., 1986.

[7] A.W. Glisson and C.M. Butler, "Analysis of a wire antenna in the presence of a body of revolution," *IEEE Trans. Antennas Propagat.*, vol. AP-28, No. 5, pp. 604-609, 1980.

[8] J.F. Shaeffer and L.N. Medgyesi-Mitschang, "Radiation form wire antennas attached to bodies of revolution: the junction problem," *IEEE Trans. Antennas Propagat.*, vol. AP-29, No. 3, pp. 479-487, 1981.

[9] J.F. Shaeffer, "EM scattering from bodies of revolution with attached wires," *IEEE Trans. Antennas Propagat.*, vol. AP-30, No. 3, pp. 426-431, 1982.

[10] R. Pérez-Leal and M.F. Cátedra, "Input Impedance of wire antennas attached on-axis to conducting bodies of revolution," *IEEE Trans. Antennas Propagat.*, vol. AP-36, No. 9, pp. 1236-1243, 1988.

[11] D.C. Jenn, and W.V.T. Rusch, "An E-field integral equation solution for the radiation from reflector antennas with struts," *IEEE Trans. Antennas Propagat.*, vol. AP-37, No. 6, pp. 683-689, 1989.

[12] T.E. Durham and C.G. Christodoulou, "Electromagnetic radiation from structures consisting of combined body of revolution and arbitrary surfaces," *IEEE Trans Antennas Propagat.*, vol. AP-40, No. 9, pp. 1061-1067, 1992.

[13]   T.E. Durham and C.G. Christodoulou, "Integral equation analysis of dielectric bodies of revolution in the presence of arbitrary surfaces," *IEEE Antennas and Propagat. Society Internat. Symp. Digest*, vol. 1, pp. 44-47, June 1993.

[14]   T.E. Durham and C.G. Christodoulou, "A method for treating junctions between bodies of revolution and arbitrary surfaces," *IEEE Trans Antennas Propagat.*, vol. AP-42, No. 2, pp. 213-219, 1994.

[15]   G.P. Junker, A.A. Kishk, and A.W. Glisson, "Numerical analysis of dielectric resonator antennas excited in quasi-TE modes," *Electronics Letters*, Vol. 29, No. 21, pp. 1810-1811, 1993.

[16]   G.P. Junker, A.A. Kishk, and A.W. Glisson, "Input impedance of an aperture coupled dielectric resonator antenna," 1994 *IEEE Antennas and Propagat. Society Internat. Symp. Digest*, vol. 2, pp.748-751, Seattle, June, 1994.

[17]   G.P. Junker, A.A. Kishk, and A.W. Glisson, "Input impedance of dielectric resonator antennas excited by a coaxial probe," *IEEE Trans Antennas Propagat.*, vol. 42, pp. 960-966, July 1994

[18]   R.F. Harrington, *Field Computation by Moment Methods*, Malabar, Fla., Robert E. Kreiger Publishing, 1968.

[19]   R.S. Elliott, *Antenna Theory and Design*, Englewood Cliffs, NJ, Prentice-Hall, Inc., 1981.

[20]   R.F. Harrington, *Time Harmonic Electromagnetic Fields*, New York, McGraw Hill, 1961.

[21]   A.A. Kishk, and L. Shafai, "Different formulations for numerical solution of single and multibodies of revolution with mixed boundary conditions," *IEEE Trans. and Propagat.*, vol. AP-34, No. 5, pp.666-673, 1986.

[22]   A.A. Kishk, *Different Integral Equations for Numerical Solution of Problems Involving Conducting of Dielectric Objects and Their Combination*, PhD. Thesis. University of Manitoba, Manitoba, Canada, 1986.

[23]   G. Zhou, A.A. Kishk, A.W. Glisson, "Input impedance of hemispherical dielectric resonator antenna excited by a coaxial probe", *IEEE Antennas and Propagat. Society Internat. Symp. Digest*, vol. 2, pp. 1038-1041, June 1993.

[24]   W. Zheng and S. Ström, "The null-field approach to electromagnetic resonance of composite objects," *Computer Physics Communications*," Vol. 68, pp. 157-174, 1991,

[25]   G.P. Junker, A.A. Kishk, A.W., Glisson, and D. Kajfez, "Effect of an air gap on cylindrical dielectric-resonator antennas operating in the TM_{01} mode," *Electronics Letters*, vol. 30, No.2, pp. 40-43, 1994.

[26]   G.P. Junker, A.A. Kishk, A.W., Glisson, and D. Kajfez, "Effect of an air gap around the coaxial probe exciting a cylindrical dielectric resonator antenna," *Electronics Letters*, vol 30, No.3, pp. 177-178, 1994.

[27]   A.A. Kishk, M.R. Zunoubi, D. Kajfez, "A numerical study of a dielectric disk antenna above a grounded dielectric substrate," *IEEE Trans. Antennas Propagat.*, vol. AP-41, No. 6, pp. 813-821, June 1993.

[28]   A.A. Kishk, A.W. Glisson, and P.M. Goggans, "Scattering from conductors coated with materials of arbitrary thickness," *IEEE Trans. Antennas Propagat.*, vol. AP-40, No. 1, pp. 108-112, 1992.

[29]   J.T. St. Martin, Y.M.M. Antar, A.A. Kishk, A. Ittipiboon, and M. Cuhaci, "Dielectric-resonator antenna using aperture coupling," *Electronics Letters*, Vol. 26, No. 24, pp. 2015-2106, 1990.

[30]   A.A. Kishk, A. Ittipiboon, Y.M.M. Antar, and M. Cuhaci, "Dielectric-resonator antenna fed by a slot in the ground plane of a microstripline," *IEE Publication No. 370, Antennas and Propagation*, Part I, pp. 540-543, 1993.

[31]   K.W. Leung, K.Y.A. Lai, K.M. Luk, and D. Lin, " Input impedance of aperture coupled hemispherical dielectric resonator antenna," *Electronics Letters*, vol. 29, No. 13, pp. 1165-1167, 1993.

[32]   G. Zhou, "Analysis of a hemispherical dielectric resonator (DRA) excited by a coaxial probe or a narrow slot," master's thesis, Department of Electrical Engineering, University of Mississippi, Dec. 1993.

[33]   A.A. Kishk, G. Zhou, and A.W. Glisson, "Analysis of dielectric-resonator antennas with emphasis on hemisphericl structures," *IEEE Antennas and Propagat. Society Newsletter*, vol. 36, pp. 20-31, April, 1994.

[34]   C.M. Butler, Y. Rahmat-Samii, and R. Mittra, "Electromagnetic penetration through apertures in conducting surfaces," *IEEE Trans. Antennas and Propagat.*, vol. AP-34, No. 1, pp. 82-93, 1986.

[35]   A.W. Glisson and D.R. Wilton, "Simple and efficient numerical methods for problems of electromagnetic radiation and scattering from surfaces," *IEEE Trans. Antennas and Propagat.*, vol. AP-28, No. 5, pp. 593-603, 1980.

[36]   D.M. Pozar, "A reciprocity method of analysis for printed slot and slot-coupled microstrip antennas," *IEEE Trans. Antennas and Propagat.*, vol. AP-34, No. 12, pp. 1439-1446, 1986.

[37]   R.W. Jackson and D.M. Pozar, "Full-wave analysis of microstrip open-end and gap discontinuities," *IEEE Trans. Microwave Theory Tech.*, vol. MTT-33, No. 10, pp.1036-1042, 1985.

[38] T.K. Sarkar, "A study of the various methods for computing electromagnetic field utilizing thin wire integral equations," *Radio Sci.*, vol. 18, 1983, pp.29-38.

[39] R.W.P. King, *Tables of Antenna Characteristics*, New York, IFI/Plenum Data Corporation, 1971.

[40] D. Kajfez, A. W. Glisson, J. James, "Evaluation of modes in dielectric resonators using a surface integral equation formulation," *IEEE MTT-S International Microwave Symposium Digest*, Boston, pp. 409-411, June 1983.

[41] D. Kajfez, A. W. Glisson, J. James, "Computed modal field distributions of isolated dielectric resonators," *IEEE MTT-S International Microwave Symposium Digest*, pp. 193-195, San Francisco, June 1984.

[42] A. W. Glisson, D. Kajfez, J. James, "Evaluation of modes in dielectric resonators using a surface integral equation formulation," *IEEE Trans. Microwave Theory Techn.*, vol. MTT-31, pp. 1023-1029, December 1983.

[43] D. Kajfez, A. W. Glisson, J. James, "Computed modal field distributions for isolated dielectric resonators," *IEEE Trans. Microwave Theory Techn.*, vol. MTT-32, pp. 1609-1616, December 1984.

[44] G. F. Engen and C. A. Hoer, "Thru-reflect-line: an improved technique for calibrating the dual six-port automatic network analyzer," *IEEE Trans. Microwave Theory Tech.*, vol MTT-27, pp. 987-993, December 1979.

[45] J. Guo, "Impedance measurement of a slot-excited circular dielectric radiator," M. S. Thesis, *Dept. of Electr. Engr., U. of Mississippi*, December 1993.

[46] H. G. Booker, "Slot aerials and their relation to complementary wire aerials," *J.I.E.E.* (London), part IIIA, vol. 93, pp. 620-626, 1946.

[47] K. W. Leung and K. M. Luk, "Moment method solution of aperture-coupled hemispherical dielectric resonator antenna," *IEEE AP-S International Symposium Digest*, Seattle, WA pp. 752-755, June 1994.

[48] C. E. Tong and R. Blundell, "An annular slot antenna on a dielectric half-space," *IEEE Trans. Antennas Propagat.*, vol. 42, No. 7, 967-974, 1994.

Rome Laboratory

Customer Satisfaction Survey

RL-TR-_____   .

Please complete this survey, and mail to RL/IMPS,
26 Electronic Pky, Griffiss AFB NY 13441-4514. Your assessment and
feedback regarding this technical report will allow Rome Laboratory
to have a vehicle to continuously improve our methods of research,
publication, and customer satisfaction. Your assistance is greatly
appreciated.
Thank You

_____

_____

Organization Name:_____(Optional)

Organization POC: _____(Optional)

Address:_____

1.   On a scale of 1 to 5 how would you rate the technology
developed under this research?

     5-Extremely Useful   1-Not Useful/Wasteful

                    Rating_____

Please use the space below to comment on your rating. Please
suggest improvements. Use the back of this sheet if necessary.

2.   Do any specific areas of the report stand out as exceptional?

                 Yes____   No_____

     If yes, please identify the area(s), and comment on what
aspects make them "stand out."

3. Do any specific areas of the report stand out as inferior?

Yes___ No___

If yes, please identify the area(s), and comment on what aspects make them "stand out."

4. Please utilize the space below to comment on any other aspects of the report. Comments on both technical content and reporting format are desired.